NTNU
Norwegian University of
Science and Technology

Control System on a Wind Turbine

Evaluation of Control Strategies for a Wind Turbine with Hydraulic Drive Train by Means of Aeroelastic Analysis

Lars Frøyd

Master of Science in Energy and Environment
Submission date: June 2009
Supervisor: Morten Kjeldsen, EPT
Co-supervisor: Torbjørn Nilsen, EPT
Ole Gunnar Dahlhaug, EPT
Peter Chapple, ChapDrive AS

Norwegian University of Science and Technology
Department of Energy and Process Engineering

Problem Description

The objective of the thesis is to:

1. Develop a control system based on a variable speed on the wind turbine shaft, with or without pitch control.
2. Conduct control system analyses using aero-elastic software such as GH Bladed or FAST.
3. Conduct aero-elastic analysis using software such as GH Bladed or FAST.

If there is time, the student shall:
4. Implement the control system in Matlab and Simulink for further implementation in the controller at ChapDrive's turbine, which is located at Valsneset.
5. Conduct tests on ChapDrive's turbine, which is located at Valsneset
All points are carried out in close collaboration with personnel at ChapDrive.

Assignment given: 19. January 2009
Supervisor: Morten Kjeldsen, EPT

Norges teknisk-
naturvitenskapelige universitet
NTNU

Fakultet for ingeniørvitenskap og teknologi
Institutt for energi- og prosessteknikk

EPT-H-2009-Nr

MASTEROPPGAVE

for
Lars Frøyd
Våren 2009

Kontrollsystem for en vindturbin
Control system on a wind turbine

Bakgrunn
Utviklingen av vindturbiner har gått i fra enheter på 1 MW i 1999 til at man i dag har 5 MW. Dette har ført til at turtallet på turbinene har blitt drastisk redusert som igjen fører til at mekaniske girbokser blir uforholdsmessig store og tunge. Ved Vannkraftlaboratoriet er det utviklet en hydraulisk transmisjon som kan benyttes i vindturbiner som kan redusere vekten av girboksen og som gir mulighet for at generatoren kan flyttes ned på bakken. Det er startet et selskap som skal videreutvikle denne teknologien som heter ChapDrive AS. Det er i denne sammenheng testet en slikt hydraulisk transmisjon ved Vivas vindturbin på Valsneset. Studenten skal være med å utvikle kontrollsystemet og eventuelt gjennomføre funksjonstester på denne turbinen. Resultatet fra disse beregningene er konfidensielle.

Mål
Målet med dette prosjektet er å utvikle og teste et kontrollsystem for en vindturbin

Oppgaven bearbeides ut fra følgende punkter:

1. Utarbeide et kontrollsystem basert på variabelt turtall på turbinakslingen, med eller uten pitch control

2. Gjennomføre kontrollsystemanalyser vha software som for eks. GH Bladed

3. Gjennomføre aeroelastiske analyser vha software som for eks. GH Bladed

Dersom det er tid skal studenten:

4. Gjennomføre programmering med Matlab og SimuLink og implemtere hele eller deler av dette til kontrollsystemet til ChapDrive’s turbin som står på Valsnes

5. Gjennomføre tester på ChapDrive’s turbin som står på Valsnes

Alle punktene gjennomføres i nært samarbeid med personell ved ChapDrive.

Senest 14 dager etter utlevering av oppgaven skal kandidaten levere/sende instituttet en detaljert fremdrift- og evt. forsøksplan for oppgaven til evaluering og evt. diskusjon med faglig ansvarlig/ veiledere. Detaljer ved evt. utførelse av dataprogrammer skal avtales nærmere i samråd med faglig ansvarlig.

Besvarelsen redigeres mest mulig som en forskningsrapport med et sammendrag både på norsk og engelsk, konklusjon, litteraturliste, innholdsfortegnelse etc. Ved utarbeidelsen av teksten skal kandidaten legge vekt på å gjøre teksten oversiktlig og velskrevet. Med henblikk på lesning av besvarelsen er det viktig at de nødvendige henvisninger for korresponderende steder i tekst, tabeller og figurer anføres på begge steder. Ved bedømmelsen legges det stor vekt på at resultatene er grundig bearbeidet, at de oppstilles tabellarisk og/eller grafisk på en oversiktlig måte, og at de er diskutert utførlig.

Alle benyttede kilder, også muntlige opplysninger, skal oppgis på fullstendig måte. (For tidsskrifter og bøker oppgis forfatter, tittel, årgang, sidetall og evt. figurnummer.)

Det forutsettes at kandidaten tar initiativ til og holder nødvendig kontakt med faglærer og veileder(e). Kandidaten skal rette seg etter de reglementer og retningslinjer som gjelder ved alle fagmiljøer som kandidaten har kontakt med gjennom sin utførelse av oppgaven, samt etter eventuelle pålegg fra Institutt for energi- og prosessteknikk.

I henhold til "Utfyllende regler til studieforskriften for teknologistudiet/sivilingeniørstudiet" ved NTNU § 20, forbeholder instituttet seg retten til å benytte alle resultater i undervisnings- og forskningsformål, samt til publikasjoner.

Ett -1 komplett eksemplar av originalbesvarelsen av oppgaven skal innleveres til samme adressat som den ble utlevert fra. (Det skal medfølge et konsentrert sammendrag på maks. en maskinskrevet side med dobbel linjeavstand med forfatternavn og oppgavetittel for evt. referering i tidsskrifter).
Til Instituttet innleveres to - 2 komplette, kopier av besvarelsen. Ytterligere kopier til evt. medveiledere/oppgavegivere skal avtales med, og evt. leveres direkte til, de respektive.
Til instituttet innleveres også en komplett kopi (inkl. konsentrerte sammendrag) på CD-ROM i Word-format eller tilsvarende.

Institutt for energi og prosessteknikk, 12. januar 2009

Johan E. Hustad
Instituttleder

for Morten Kjeldsen
Faglærer/veileder

Medveiledere:	Torbjørn Nielsen	
	Ole G. Dahlhaug	
	Peter Chapple	ChapDrive AS
	Svein Kjetil Haugset	ChapDrive AS

Preface

This Master's thesis was prepared at the Hydro Power Laboratory at the Norwegian University of Science and Technology (NTNU). It is the result of six months of work, and it is the continuation of my project thesis.

I would like to express my gratitude to Associate Professor Morten Kjeldsen for his supervision, valuable discussions and support. I would also like to thank my co-supervisors at NTNU Professor Torbjørn Nielsen for giving me opportunity to do my thesis at the Hydro Power Laboratory and Professor Ole Gunnar Dahlhaug who first introduced me to the mysteries of wind turbines and who suggested the subject of the thesis. Thanks for all the conversations and discussion during the work with the thesis and during my 18 months here at the Laboratory.

Thanks also to the people at ChapDrive A/S for allowing me to work with such an interesting problem. I would like to thank all of them for sharing their valuable time with me and for the numerous pleasant Friday lunches at their office. A special thank goes to Svein Kjetil Haugset, Per Olav Haarberg and Peter Chapple for long and interesting technical discussions and invaluable input to my work. Without them, this thesis would never have been possible.

My greatest appreciation to my fellow students, my classmates and friends at *Energy and Environment* and my colleagues here at the Laboratory for all their feedback and support and interesting discussions. Not to mention the cheerful lunches and all the fun we have had together. You all have made the years in Trondheim a memorable experience.

Summary

The objective of this thesis is

1. To develop a combined hydraulic and aeroelastic model of variable speed, variable pitch wind turbine with a hydraulic drive train.
2. To investigate the dynamic properties in the system and use the knowledge to create a control strategy and implement a control system for the said wind turbine model.
3. To analyse and evaluate the control system in terms of stability, power production and fatigue life time damage.

The wind turbine is a 225 kW originally fixed speed, variable pitch turbine that has been modified by replacing the original drive train with a hydrostatic transmission. The hydraulic part is modelled in the Matlab simulation environment Simulink and the coupled structural and aerodynamic simulations are carried out in the aeroelastic simulation program FAST.

The aerodynamic properties are developed using XFOIL, and found to match the reported aerodynamic characteristics well. A quasi-dynamic model based on steady state aerodynamic properties is used for verification of the aeroelastic model.

The structural models are created partially based on information from the manufacturer of the turbine, and partially by analysis of and comparison with the structural properties of other wind turbines.

An analysis of the natural frequencies of the different components in the system is carried out and the result is presented in terms of a Campbell diagram. This exercise was necessary because the turbine was designed for fixed speed operation. Before running the turbine at variable speed one should be aware of any resonance frequencies. The natural frequencies were also found by spectral analysis of time-domain simulations.

A control strategy is developed based on maximum power point tracking by following the optimal tip speed ratio in the low wind speed regime. In the above rated wind speed regime, power is limited by blade feathering. The control strategy is developed using blade element momentum methods, based on the steady state aerodynamic characteristics.

Following the optimal tip speed ratio requires a method of estimating the wind speed. For that purpose, a wind speed estimator is developed based on look-up tables according to the torque and rotor speed characteristics at different wind speeds and pitch angles. The wind speed estimator is tested and found to produce excellent wind speed estimates for conventional wind turbines, but the slow dynamics and oscillations of the hydrostatic drive train causes problems, so that the wind speed estimate is lagging behind the actual wind speed.

A control system that uses both pitch control and speed control is developed. The pitch controller is developed based on information on the control system of the actual turbine. The information on the controller is limited, but a model of the turbine with the original drive train is created, and the pitch controller is developed and tested on that model until good conformity with the expected behaviour is observed. The speed controller is developed based on PID control. The wind speed estimate is used to determine the set speed.

Six different configurations of the wind turbine controller is developed and tested for stability. A comprehensive analysis is carried out and the wind turbine configurations are simulated for wind speeds ranging from cut-in to cut-out. Based on the simulations, the real power curves are found, and a fatigue analysis is carried out. The turbines with hydrostatic transmission is found to have generally lower fatigue damage than a comparable turbine with conventional drive train. The power production is considerably lower due to the extra losses in the hydraulic transmission.

Sammendrag

Målet med denne oppgaven er å

- Utvikle en kombinert hydraulisk og aeroelastisk modell av en vindturbin med hydraulisk gir som skal kunne kjøres på variabelt turtall og med variabel pitchvinkel.
- Undersøke de dynamiske egenskapene til systemet, og bruke denne kunnskapen til å utvikle et reguleringssystem for den nevnte vindturbinmodellen.
- Analysere og vurdere reguleringssystemet med hensyn på stabilitet, effektproduksjon og materialtretthet i ulike komponenter.

Det hydrauliske systemet er modellert i simuleringsverktøyet Simulink i Matlab, og den kombinerte konstruksjons- og aerodynamiske analysen er utført i det aeroelastiske simuleringsverktøyet FAST.

De aerodynamiske karakteristikkene er bestemt ved hjelp av XFOIL, og de viser seg å stemme godt med de oppgitte aerodynamiske egenskapene. De strukturelle modellene av bladene og tårnet er basert på informasjon fra turbinprodusenten, men informasjonen om bladene var mangelfull.

En egenfrekvensanalyse har blitt utført på de ulike komponentene i systemet, og resultatet er presentert i et Campbell-diagram. Begrunnelsen for en slik analyse er at turbinen opprinnelig er designet for konstant turtall. Før turbinen kan kjøres på variabelt turtall må man bestemme turtallsområdene der interferens kan inntreffe.

En reguleringsstrategi for vindturbinen har blitt utviklet basert på variabelt turtall, slik at turbinen kan følge det optimale driftspunktet for vindhastigheter under merkehastigheten. For høye vindhastigheter blir effekten begrenset ved å pitche bladene ut av rotorplanet.

For å kunne følge det optimale driftspunktet behøves et estimat på den virkelige vindhastigheten. Det har derfor blitt utviklet en vindhastighetsestimator som baser seg på måling av akselmomentet og rotorturtallet. Testing av estimatoren viser at den beregner den virkelige vindhastigheten meget godt for vindturbiner med konvensjonelt gir, men tregheten i den hydrauliske overføringen skaper problemer og fører til at den estimerte vindhastigheten henger etter den virkelige.

Et reguleringssystem basert på den nevnte reguleringsstrategien har blitt utviklet. Pitchreguleringssystemet har blitt utviklet basert på informasjon om det tilsvarende systemet i den virkelige vindturbinen, men informasjonen var mangelfull. Det har ført til at en modell av den opprinnelige turbinen har blitt laget slik at pitchsystemet har kunnet bli testet og forbedret inntil god overensstemmelse med den forventede oppførselen er funnet. Turtallsregulatoren er basert på PID regulering, der referansehastigheten er beregnet av vindhastighetseregulatoren.

I alt seks varianter av reguleringssystemet har blitt utviklet og testet for stabilitetsproblemer. Deretter har en omfattende analyse av vindturbinmodellene blitt utført, med simuleringer for alle vindhastigheter mellom innkoplings- og utkoplingshastigheten. Basert på resultatene har de virkelige effektkurvene blitt funnet. I tillegg har det blitt utført en utmatningsanalyse på tårnet, bladene og akslingene. Turbinene med hydraulisk gir viste seg å ha generelt mindre utmatningsødeleggelser enn en tilsvarende turbin med konvensjonelt gir.

Contents

1 Introduction 1

2 Background 3
- 2.1 Previous work . . . 3
- 2.2 Ongoing work . . . 3
- 2.3 Available literature . . . 4

3 Wind turbine aeroelastics 6
- 3.1 Aeroelastic codes . . . 6
- 3.2 Coordinate system definitions . . . 6
- 3.3 Aerodynamics . . . 7
  - 3.3.1 Unsteady aerodynamics . . . 8
- 3.4 Structural elements . . . 9
  - 3.4.1 Modal approach . . . 9
  - 3.4.2 Finite element methods . . . 9
- 3.5 Wind description . . . 10

4 Dynamic loading and fatigue 12
- 4.1 Gravity load . . . 13
  - 4.1.1 Wind shear . . . 13
- 4.2 Tower shadow . . . 13
- 4.3 Yaw error . . . 15
- 4.4 Wind inclination angle and shaft tilt . . . 15
- 4.5 Fatigue damage . . . 16
  - 4.5.1 SN-curves . . . 16
  - 4.5.2 Palmgren-Miner rule . . . 16
  - 4.5.3 Rain-flow cycle counting . . . 17

5 Vestas V27 properties 19
- 5.1 Generator . . . 19
- 5.2 Pitch system . . . 20
- 5.3 Aerodynamics . . . 21
- 5.4 Structural Dynamics . . . 26
  - 5.4.1 Blades . . . 26
  - 5.4.2 Tower . . . 29

6 Hydraulic transmission 31
6.1 Pump and motor characteristics 33
6.2 Pipe flow and pressure 34
6.3 Simulink model 36

7 Aeroelastic and quasi-steady aerodynamic model comparison 37
7.1 Aeroelastic model 37
7.2 Quasi-steady model 37
7.3 Comparison 38

8 System frequencies and frequency response simulation 41
8.1 Drive train natural frequency 41
8.1.1 Linear approximation 41
8.1.2 Non-linear approach 43
8.2 Campbell diagram 44
8.3 Frequency responses in the non-linear system 46
8.3.1 Speed control frequency response 47
8.3.2 Pitch control frequency response 48

9 Control objectives and definitions 50
9.1 Energy capture 50
9.1.1 Maximum power point tracking 51
9.1.2 Wind speed estimation 52

10 Control strategies 54
10.1 Base case: Original Vestas V27 54
10.1.1 Simulation results 57
10.2 MPPT constant PID control 58
10.2.1 Linear analysis 59
10.2.2 Controller implementation 61
10.3 Gear box substitute 63
10.3.1 Improved gearbox substitute 64
10.4 MPPT Gain scheduling PID control 66
10.4.1 First attempt 66
10.4.2 Second attempt 68
10.5 Reduced power point tracking (RPPT) 70
10.6 Self governed turbine 71

11 Evaluation and comparison 73
11.1 Results 76
11.1.1 Performance 76
11.1.2 Fatigue life time damage 77
11.2 Comments on the results in appendix B and C. 80

12 Discussion and conclusion 82

13 Proposal for further work 86

A Linear analysis I

B Power curves VII

C Pitch and rotor speed curves IX

D Vestas blade data XI

E Xfoil input paramters XIII

F Simulink block diagram XV

G Quasi-steady model block diagram XVII

List of Figures

3.1 Blade coordinate system . . . 7
3.2 Tower and rotor coordinate systems . . . 7
3.3 Airfoil transistion and separation . . . 8
3.4 Comparison of static stall and Beddoes-Leishman dynamic stall . . . 8
3.5 3D wind history input . . . 10
3.6 IEC turbulence standard deviation . . . 11
3.7 IEC turbulence intensity classes . . . 11

4.1 FFT: Blade motion with wind shear . . . 12
4.2 FFT: Tower and blade motion . . . 12
4.3 Gravity load on one blade . . . 13
4.4 Gravity load on three blades . . . 13
4.5 Wind shear . . . 14
4.6 Wind shear loading . . . 14
4.7 Tower shadow velocity profile . . . 14
4.8 Downwind tower shadow loading . . . 14
4.9 Change of relative velocity and angle of attack due to yaw error as a function of ψ 15
4.10 5°yaw error . . . 15
4.11 20°yaw error . . . 15
4.12 Example of experimental and linear approximated SN-curves . . . 17
4.13 Pagoda-roof rain-flow counting analogy . . . 17

5.1 Generator torque curve . . . 20
5.2 Linear generator area . . . 20
5.3 Typical pitch system . . . 21
5.4 Simplified Simulink model . . . 21
5.5 Approaches for determining C_L and C_D curves . . . 21
5.6 α_{opt} and transition point . . . 23
5.7 Change of α by -4°pitch . . . 23
5.8 Transition lines at cut-in . . . 24
5.9 Transition lines at cut-out . . . 24
5.10 Extrapolated C_L, C_D and C_M . . . 25
5.11 Optimal pitch angle β . . . 25
5.12 Blade station locations . . . 25
5.13 Measured and simulated power curves . . . 26
5.14 $C_{L\max}$ curves . . . 27
5.15 Start-up torque curve. . . . 27
5.16 Flapwise stiffness distribution . . . 27
5.17 Blade interior geometry . . . 28

5.18 Flapwise stiffness 29
5.19 Mass distribution along blade 29
5.20 Edgewise stiffness distribution 29
5.21 Blade modal shapes 29
5.22 Tower modal shapes 30

6.1 Principle of the ChapDrive hydraulic transmission 31
6.2 Hydraulic transmission circuit diagram 32
6.3 Pump total efficiency diagram 33
6.4 Pump pressure loss diagram 33
6.5 Motor efficiency at 1200 *rpm* 34
6.6 Swash-efficiency diagram 34
6.7 Hydraulic transmission flow paths 35

7.1 $C_P(\lambda, \beta)$ at 17 *rpm* 38
7.2 $C_P(\lambda, \beta)$ at 43 *rpm* 38
7.3 Model comparison at 12 m/s mean wind speed with detailed view. 39

8.1 Hydraulic mass-spring damper analogy 42
8.2 Normal high and low pressure levels 43
8.3 Irregular pressure oscillations due to boost and relief valve 44
8.4 Campbell diagram 45
8.5 Campbell diagram detail 45
8.6 PSD plots showing the dominant system frequencies 46
8.7 Turbine speed frequency response block diagram 47
8.8 Rotor speed frequency response 48
8.9 Turbine power frequency response block diagram 49
8.10 Response of the pitch controller 49

9.1 Ideal power curve 50
9.2 Turbine control target curves 51
9.3 Principle of WSE 52
9.4 WSE performance 52
9.5 WSE interaction with FAST and the control system 52
9.6 Challenges in wind speed estimator performance 53

10.1 Pitch control layout 55
10.2 Pitch/power sensitivity to wind 56
10.3 Servo valve characteristic 56
10.4 Servo controller 56
10.5 Step response of original V27 power and pitch 57
10.6 V27 turbulent wind 58
10.7 V27 turbulent pitch response 58
10.8 V27 turbulent rotor power 58
10.9 Speed control system outline 59
10.10 Step response of ChapDrive I model 59
10.11 APF: No pitch control 60
10.12 APF: Ideal pitch control 60
10.13 Pressure feedback, constant gain 60
10.14 Scheduled gain 60

10.15 Speed control feedback loop block with damping injection 62
10.16 Step response of ChapDrive I model 63
10.17 Gearbox substitute performance - low wind speed 64
10.18 Step response of ChapDrive I improved gearbox substitute model 65
10.19 Speed control feedback loop gain scheduling 66
10.20 Ω_T frequency response 66
10.21 Non-linear analysis gain scheduling scheme 67
10.22 Step response of ChapDrive I gain scheduling. Approach 1 67
10.23 Visual analysis gain scheduling scheme 68
10.24 Step response of ChapDrive I gain scheduling. Approach 2 69
10.25 Reduced C_P target curves 70
10.26 Power and torque coefficients 70
10.27 RPPT turbine speed 71
10.28 RPPT hydraulic pressure 71
10.29 RPPT generator power comparison 71
10.30 Self governed hydraulic pitch system 72
10.31 Step response of the self governed turbine 72

11.1 Valsneset wind distribution 74
11.2 Relative average rotor power 76
11.3 Relative average deviation from λ_{opt} 77
11.4 Relative average generator power 77
11.5 Relative in-plane blade root moment damage 78
11.6 Relative out-of-plane blade root moment damage 78
11.7 Relative side-to-side tower root moment damage 79
11.8 Relative fore-aft tower root moment damage 79
11.9 Relative torsional tower root moment damage 80
11.10 Relative low speed shaft damage 80
11.11 Relative high speed shaft damage 81

A.1 Basic TSC feedback loop block diagram II
A.2 Change in C_t along Ω_T locus. Non-pitched blade III
A.3 Aerodynamic damping coefficient of the ideally pitched turbine III
A.4 TSC feedback loop block with damping injection IV
A.5 Bode diagram definitions VI

List of Tables

5.1 Vestas V27 specifications . . . 19
5.2 Generator specifications . . . 20

6.1 Hydraulic transmission specifications . . . 32
6.2 Equations governing hydraulic power units . . . 33
6.3 Viscous friction model . . . 35

8.1 Drive train natural frequency . . . 43

10.1 Vestas V27 prototype control parameters . . . 54
10.2 Vestas V27 model pitch control parameters . . . 57
10.3 ChapDrive 1 modelled control parameters . . . 62
10.4 ChapDrive 1 gearbox substitute model pitch control parameters . . . 63
10.5 ChapDrive 1 modelled control parameters . . . 68

Notation

List of symbols

α	Motor displacement opening-degree
β	Fluid bulk modulus
λ	Tip-speed-ratio
Ω, ω	Rotational speed (steady-state, deviation)
μ	Fluid dynamic viscosity
ρ	Fluid density
σ	Strain
$\sigma_{\mathcal{V}}$	Wind turbulence standard deviation
θ	Operational point
θ	Pitch angle
ζ	Damping coefficient, linear system
A	Swept rotor area
C_L	Lift coefficient
C_D	Drag coefficient
C_M	Pitching moment coefficient
C_P	Power coefficient
C_Q	Torque coefficient
C_T	Thrust coefficient
C_t	Torque gradient
d	Pipe diameter
D	Displacement volume
$H(s)$	Transfer function
$\mathcal{P}$	Power
P, p	Pressure
m	Mass
ℓ	Length
T	Torque
$\mathcal{T}$	Time constant
$\mathcal{U}$	Wind speed
V	Fluid volume
v	Linear speed
$\check{x}$	Estimated value of x
$\bar{x}$	Steady-state or average value of x
$\tilde{x}$	Measured value of x
$\dot{x}$	Time derivative of x

List of subscripts

T	Wind turbine
P	Hydraulic pump
M	Hydraulic motor
G	Generator
0	Synchronous speed
n	Rated operation point
$mech$	Mechanical
vol	Volumetric
tot	Total
$leak$	Internal leakage
$drain$	External leakage (to drain)
hp	High pressure line
lp	Low pressure line
ref	Reference value
res	Resultant
gov	Governor

Acronyms

PID	Proportional/integral/derivative (controller)
WSE	Wind speed estimator
TSC	Turbine speed controller
GFRP	Glass-fibre reinforced plastics
CFRP	Carbon-fibre reinforced plastics
MPPT	Maximum power point tracking
PSD	Power spectral Density
FFT	Fast Fourier transform
BEM	Blade element momentum method
DoF	Degree of freedom
APF	Amplitude-phase-frequency (diagram)

Chapter 1

Introduction

The Trondheim based company ChapDrive is developing hydraulic transmission systems to replace the traditional mechanical drive train of horizontal axis wind turbines. The purpose of this is the ability to move the generator from the nacelle to ground level, to save weight. Reducing the weight in the nacelle to improve stability and to reduce the construction costs may be a key requirement for success in development of future floating offshore wind turbines.

The hydraulic drive train makes the traditional gearbox redundant because the hydraulic transmission is able to function as a stepless reduction ratio gearbox. This means that the turbine can be operated with variable rotor speed, which can follow the optimal tip speed ratio over a wide range of wind speeds, while the generator can be operated at constant speed. This allows for high overall efficiencies in the low to mid range wind speed regimes, without extensive use of power electronic converters and rectifiers. Removing the gearbox saves weight in the nacelle, and it also means the removal of one of the most maintenance demanding units in a wind turbine. The hydraulic transmission will have lower efficiency than a standard gearbox, but the proven reliability of hydrostatic transmissions in tough conditions will hopefully compensate for the extra losses introduced, by reducing maintenance costs in offshore installations.

The introduction of a hydraulic transmission poses new challenges, especially with regards to control and stability issues. The reason for this is the relatively low stiffness of the hydraulic transmission compared to the original drive train. This introduces the risk of low frequency oscillations in the transmission, which may excite some of the numerous low frequency oscillations that are known to occur in wind turbines. It is important to investigate the possibilities of interaction between the frequencies of the transmission and the tower, blades or rotor speed, as this may cause excessive vibrations in the blades or the tower, leading to fatigue damage and reduced system life. Also the overall efficiency of the transmission is highly dependent on the strategy of operation, as both hydraulic pumps and motors have very poor characteristics outside the intended area of operation. It is therefore a necessity to develop a controller that maximizes the total efficiency, i.e. of both the turbine rotor and the transmission, over a wide range of wind speeds while staying in control of turbine oscillations.

ChapDrive now have had their transmission installed in two wind turbines at Valsneset, near Trondheim. The first one, a 225 kW Vestas V27 turbine, was installed early 2008 and is currently operable under supervision. The second one is a 900 kW NEG Micon NM52 which was erected September 2008 and is to be commissioned medio 2009. The aim of this masters thesis is to develop and test a set of controllers for the Vestas V27 turbine and to discuss means of evaluating the performance of these controllers in terms of fatigue damage and net power production. As maximum power production in general means pushing the turbine to its limits, the optimal control strategy means compromising between the aim of minimizing fatigue damage and the goal of improving the annual power production.

To be able to evaluate the controller performance, a coupled aeroelastic and hydraulic model will be developed. The open-source aeroelastic solver FAST[1] will do the aerodynamic calculations, while the hydraulic- and control systems will be modelled in the Matlab multipurpose simulation environment Simulink. In addition, a quasi-steady model will be developed for verification of the aeroelastic model and to aid the development of turbine governors. The quasi-steady model will not include structural dynamics, and it will be based on steady-state characteristics of the turbine rotor. The result is a model with fewer degrees of freedom (DoF) for reduced simulation times.

---

[1] Fatigue, Aerodynamics, Structures and Turbulence code. Developed by NREL

Chapter 2

Background

2.1 Previous work

This master's thesis is the continuation of a series of industrial and academic papers produced at ChapDrive and by master students at NTNU during the previous years. In 2005 two master's theses were written on the Hydro Power Laboratory at NTNU on the subject of evaluating hydraulic transmissions in wind turbines [8] and tidal turbines [20] respectively. Their work showed promising results, and based on this the company ChapDrive was formed.

For the first prototype, a Vestas V27 known as ChapDrive I, one master's thesis was completed in 2007 by Ove Jørås Pettersen, concerning modelling and simulations of wind turbines [36]. This thesis focused mainly on aeroelastics in general and the yawing and pitching mechanisms in wind turbines, but it also included a little on hydraulics. A control strategy and a basic hydraulic model was proposed by Steffen Andreas Varpe in 2008, in the master's thesis *Control system on a wind turbine* [45] based on field measurements of the system [44] and steady-state characteristics of the rotor, which were developed by master student Svein Kjetil Haugset [25]. A more complex model of the hydraulic system was developed by Prof. Peter Chapple from NTNU/ChapDrive and adapted to Simulink by Sintef Energy Research.

My project thesis [16] treated the second prototype, a NEG Micon NM52, known as ChapDrive II. The thesis was completed in December 2008. In that thesis a more detailed model of the hydraulic system was presented. The dynamic model of the wind turbine was built up according to the specifications from the turbine manufacturer and the aerodynamics were based on steady-state characteristics for the rotor. The thesis focused mainly on control issues, and a control strategy was developed based on a gain scheduling PID governor and wind speed estimation. It was shown that the hydraulic drive train was prone to oscillations because of negative aerodynamic damping associated with the stall-controlled rotor at high wind speeds.

2.2 Ongoing work

Parallel with the work on this thesis, similar work is carried out by two different groups related to the work of ChapDrive. Firstly a group consisting of Svin Kjetil Haugset from ChapDrive and PhD candidate Marit Reiso at NTNU is working on aeroelastic simulations on the ChapDrive II model [26]. The aim of this work is to examine the dynamic properties of the turbine before it is commissioned. The turbine model will include a simplified open-loop hydraulic transmission modelled by Garrad Hassan. A more comprehensive hydraulic transmission is also under development, but will not be finished before the deadline of this thesis.

The second group consists of Per Olav Haarberg from ChapDrive. He is working on aeroelastic modelling of the ChapDrive I model in GH Bladed in order to carry out a similar analysis as the first group at a later stage. His model does not include a hydraulic transmission, but rather the drive train of the original V27 turbine. His will use the blade structural and aerodynamic data that is developed in chapter 5 herein. This means that the the two aeroelastic models in Bladed and FAST can be verified against each other.

The two groups are writing their theses for the PhD-level course BA8607 Wind turbine design given at NTNU by prof. Geir Moe.

2.3 Available literature

The present thesis will consider the Vestas V27 turbine with the ChapDrive hydraulic transmission. In this context there are a number of important subjects including aerodynamic- and structural properties, fatigue, hydrostatic transmission modelling, and control system issues.

The aeroelastic model will be based on the aerodynamics of the rotor and the structural properties of the rotor blades and the tower. The steady-state aerodynamic properties of the turbine blades were thoroughly investigated by Svein Kjetil Haugset. A similar, simplified approach based on his findings will be used for the quasi-steady model. The aeroelastic model, however, needs a more detailed description of the unsteady aerodynamics. This means that effects like dynamic stall, and rotational stall delay must be considered. The attention to such effects is increasing and a number of recent publications deals with the subject, although most of the well-known and reputable wind turbine literature only mention these effects briefly.

The advantage of using aeroelastic models compared to quasi-steady models lies in the ability to include the motions of the elastic parts of the turbine; the tower and the blades. Therefore it is important to obtain correct values for the structural properties of these elements. The turbine documentation provided by Vestas includes a detailed description of both the tower and the blades. Although the blades and tower are complex geometrical structures, it is common to treat them as beam elements. Because of this simplification these structures can be treated according to standard theories considering mechanics of materials, which are readily available in mechanics literature.

The inclusion of structural dynamics allows for analyses of vibration induced fatigue. Fatigue is an important part of wind turbine design, and theory is treated thoroughly in *Guidelines for Design of Wind Turbines* by DNV/Risø [14]. A lot of additional literature is also available, as fatigue issues must be dealt with on all kinds of structures.

Except from the work done at the Hydro Power Laboratory and ChapDrive, there is little academic interest in the subject of wind turbines with hydraulic drive train. No external publications have been found dealing with the subject. However, control of hydraulic circuits and control of wind turbines are both subject to academic and industrial interest, and of lot of publications dealing with these subjects are available.

Publications regarding hydraulic control systems focus mainly on valve controlled systems and hydrostatic transmission for automotive applications. However, the control issues in the present problem relates more to control of wind turbines, even though the control action will be applied to the hydraulic motor. The issues regarding the hydraulic circuit will relate more to modelling of the system, a subject which was covered in detail in my project thesis. Therefore the hydraulic model will be based on the model from the project thesis, with only minor changes reflecting the the small differences between the two hydraulic circuits.

In the area of wind turbine control, two subjects were found to be of special importance in the project thesis, namely adaptive control techniques and wind speed estimation. The most commonly used adaptive control technique, gain scheduling, was implemented because of highly non-linear rotor characteristics of the stall-controlled NEG Micon turbine. The Vestas turbine has pitch control, and it is therefore not certain that gain scheduling is necessary. However, scheduled gains has been shown to improve the performance of variable speed wind turbines with pitch control as well [7]. A lot of literature on both constant gain and scheduled gain PID control is available, as this type of controllers have been the industry standard for decades.

A knowledge of the wind speed was found to be important in variable speed turbines for two reasons: Firstly the reference turbine speed is set according to the optimal tip speed ratio, which depends on the wind speed. Secondly the gain scheduling controller was scheduled according to the wind speed. Wind speed estimation is necessary because the wind turbine anemometer is placed behind the turbine rotor, which means that the readings will be disturbed by the passing blades. Literature dealing with wind speed estimation is quite limited but a few publications have been found dealing with the subject. The wind speed estimator will be based on the work done during the writing of the project thesis.

Chapter 3

Wind turbine aeroelastics

In the early days of the modern wind energy era, wind turbine dimensioning were based on steady-state load calculations. For small and stiff turbines this may give fairly good indications of the required strength, but in order to reduce the overall cost of the turbines, the current trend is to develop larger turbines with lighter and more flexible parts. This development increases the wind induced vibrations and oscillations in the structure, and thus also the necessity to include these motions in the calculations. Aeroelastic simulation codes combine aerodynamic calculations and elastic deformation with time-varying wind loads to better predict the dynamic loading that wind turbines are exposed to.

3.1 Aeroelastic codes

A large number of different aeroelastic codes exist at the present. A summary of the origins and capabilities of thirteen of the best known aeroelastic codes is found in [2], which gives a very good overview of the available tools. Such an exercise is of little interest for this thesis, and in the following only three of these codes will be taken into consideration. These are the *GH Bladed* by Garrad Hassan (United Kingdom), *HAWC II* by Risø National Laboratories (Denmark) and *FAST* by National Renewable Energy Laboratory (USA). These three codes are chosen because they are in frequent use at the Norwegian University of Science and Technology (NTNU) and in the Norwegian wind power industry in general.

3.2 Coordinate system definitions

The terms and coordinates used for denoting the geometry, displacements and loads on the turbine blades, rotor and tower is summarised in figures 3.1 and 3.2. The blade coordinate system is twisted along the blade span according to the structural twisting of the blade cord. The twist is zero at the blade tip and increasing towards the hub to improve the blade aerodynamics. The flapwise and edgewise directions denote the directions normal to and parallel to the blade cord at the tip. If the blade pitch is zero, the flapwise direction corresponds the out-of-plane rotor direction while the edgewise blade direction is equal to the in-plane rotor direction. For a pitched blade, a purely flapwise deflection will yield both in-plane and out-of-plane deflection of the rotor.

The tower motions are defined relative to the main shaft axis. Fore-aft deflections are parallel to the main shaft and side-to-side deflections are normal to the main shaft. Yaw error is the misalignment angle of the turbine shaft relative to the wind speed.

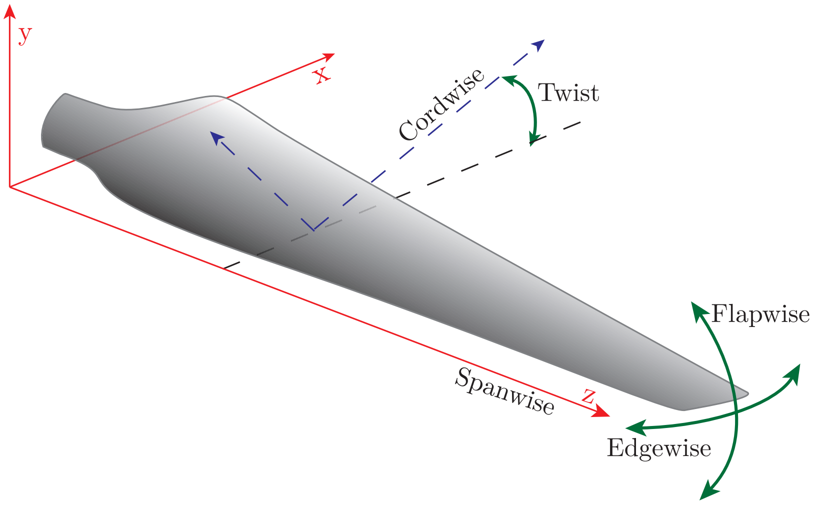

Figure 3.1: Blade coordinate system

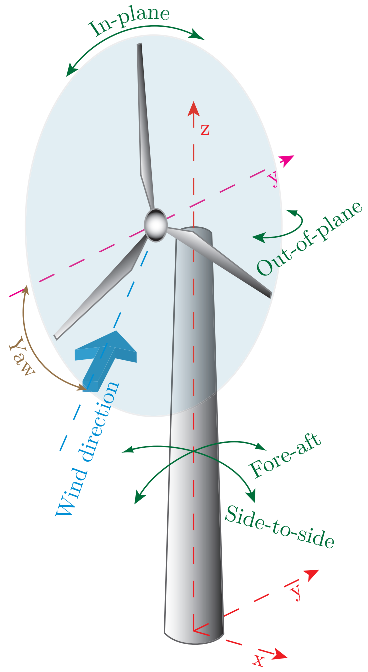

Figure 3.2: Tower and rotor coordinate systems

Both the blades and the tower may have torsional deflections around the z-axis, although not all aeroelastic codes are capable of calculating these components.

3.3 Aerodynamics

The core functionality of an aeroelastic code lies in the ability to handle aerodynamics. Today's most advanced aerodynamic solvers use computational fluid dynamics (CFD) to solve the flow field around a wing profile, but this is a very time consuming task due to the size of the rotor. An alternative, and far less expensive, method of calculating the aerodynamic forces is the blade element momentum (BEM) method. This method is based on an assumption of uniform and steady airflow, but BEM theory can also be extended to include dynamic effects as explained in section 3.3.1. The theory of BEM methods is readily available in general purpose wind energy literature like [34] and will therefore not be explained here.

The BEM method looks up the lift and drag coefficients from predefined tables. For this reason, the BEM aerodynamic calculations cannot be more accurate than the lift and drag curves available. These curves can be produced by scale model testing, CFD or panel methods, but all these methods have problems with prediction of transition and separation points. The transition point is the point where the flow changes from laminar to turbulent, due to roughness of the airfoil surface. The separation point is the point where the air flow over the airfoil starts to detach. These notions are explained in figure 3.3. The issue with the transition point is discussed further in section 5.3, and the behaviour of separation vortexes is discussed in section 3.3.1.

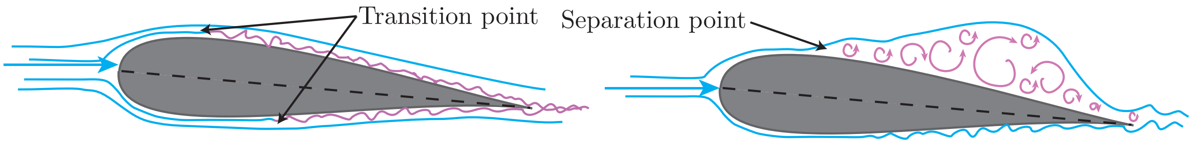

Figure 3.3: Airfoil transistion and separation

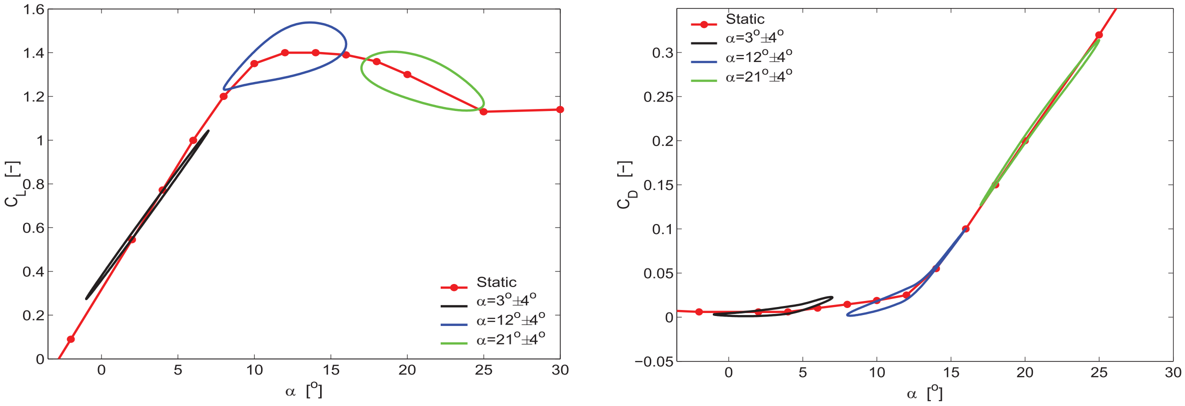

Figure 3.4: Comparison of static stall and Beddoes-Leishman dynamic stall
Adapted from [24]

3.3.1 Unsteady aerodynamics

Because the BEM method uses look-up tables of steady-state lift and drag coefficients, it is not natively able to handle unsteady flows, especially the stall phenomenon. Stalling occurs when the angle of attack becomes too large, so that the adverse pressure gradient at the suction surface of the airfoil becomes too large. When this happens, the flow can no longer maintain attached to the airfoil and it separates and forms a bubble of highly turbulent boundary layer, which may reattach at some point further down the cord for partially detached flow, or continue into the wake for fully detached flow. The look-up method implies that the airfoil can switch between stalled condition to attached flow from one time step to the next. In practise, the separation bubble will have to shed into the wake, and the flow will use some time to reattach and stabilise. To compensate for this, the aerodynamic solver uses a *dynamic stall model* that imitates the lift ans drag transients that follow the shedding of the separation vortex.

The dynamic stall model used in FAST is the Beddoes-Leishman model[1]. This model was originally developed for calculating lift in a helicopter rotor, but it has later been adapted for use in wind turbine calculations. An example of how the dynamic stall influence the lift and drag is illustrated in figure 3.4

A different effect that occurs in rotating airfoils is an effect known as *stall delay*. The characteristics of the stall delay phenomenon is that stalling of the turbine blades is shifted to higher angles of attack for rotating blades compared to non-rotating wings. The shift is due to three dimensional effects, but the physical explanation for this shift is not fully understood: Different studies suggest it is related to the twist- and chord to radius distribution [12] or Reynolds number effects in addition to centrifugal- and Coriolis forces [10,28]. The result is that the lift and drag forces at high angles of attack will be larger for a real turbine than what will be found through 2D calculations. A number of different stall delay models exist, and five of these models were compared in a recent study by Simon-Philippe Breton on NREL's 10 m diameter wind tunnel test turbine [10]. Among these five models it was found large discrepancies in predictions of the phenomenon, and none of the models were found to reproduce the test result well. Stall delay is believed to have larger influence on the behaviour of stall controlled turbines as they operate more in the deep stall area than pitch controlled ones. Thus compensating for the stall delay phenomenon in pitchable turbines is not of great importance [42]. None of the three aeroelastic codes discussed incorporate a stall delay model. It is however possible to include one by applying any of the models to the lift and drag curves directly [9].

---

[1] A through explanation and experimental testing of the model is given in [37]

3.4 Structural elements

In a real wind turbine all components will be somewhat flexible, but the effect of most of these on the overall dynamics is negligible. Three of the main components will, however, have a great influence on the turbine response. These are the tower, the blades and the drive train. The blades and tower are long and relatively slender objects that will flex under loading and possibly have oscillations and deflections of large amplitude, due to resonant loading. The drive train of most turbines is quite stiff, a massive steel shaft and possibly a gearbox. Still the drive train dynamics are important because coupling of the rotor and drive train is prone to oscillations that can excite the side-to-side vibration modes of the tower [9]. Excessive oscillations in the in-plane direction will cause wear and fatigue loading on the gearbox and generator [2]. In the special turbine configuration considered herein, a hydraulic drive train will be utilized, which further increase the importance of the drive train dynamics.

There are two fundamentally different methods of treating the structural dynamics in aeroelastic simulation codes; finite element analysis and modal analysis. HAWC II uses finite element methods, while GH Bladed and FAST uses the modal approach.

3.4.1 Modal approach

The modal representation is a simplified way to determine the deflection of the flexible parts of a structure with relatively few degrees of freedom (DoF). This is possible by determining the body's different natural frequencies and the accompanying deflection shapes known as the mode shapes. The idea of the modal representation is that the deflection of an element at any instant must be a linear combination of the element's modal shapes. The accuracy of the structural dynamics thus depends on the number of mode shapes one chooses to include. The number of mode shapes in FAST is limited to two flapwise modes and one edgewise mode for the blades. For the tower the number is limited to two fore-aft modes and two side-to-side modes. GH Bladed has the possibility to include up to nine modes for each blade direction and up to three tower modes for each direction. Including a large number of modes will only improve the calculated deflections somewhat, because the higher modes have far smaller amplitude than the first ones. The calculation time may increase noticeably by including more mode shapes because the higher modes have higher frequencies, which means that shorter time steps are necessary [9].

3.4.2 Finite element methods

The final element method is based on direct numerical calculation of the deflection of each structural element in each time step according to the stiffness and mass distribution and the damping properties. This method is held to be more accurate than the modal approach, but gives more degrees of freedom and is more computationally intensive. HAWC II uses

Timoshenko beams as the building blocks for all structural elements. This beam theory takes into account rotational inertia, and is therefore suitable for representing the torsional degree of freedom in blades and tower.

3.5 Wind description

The representation of the wind loading is different in aeroelastic simulations codes than in steady-state or quasi-dynamic counterparts. For quasi-dynamic calculations it is often sufficient to represent the wind as time varying, but spatially constant over the swept rotor area for a given time instant. Some techniques exists that can mimic the periodic loading due to wind shear and tower shade by use of so called *rotational sampling filters* [13].

FAST, GH Bladed and HAWC II all have the ability to represent the wind as a three dimensional time varying input. This is done by creating a discretized wind history in two spatial dimensions X and Y and time, as shown in figure 3.5. This resembles a wind history box that will move through the wind turbine at a pace determined by the time-resolution (frequency) of the wind data points. The spatial resolution can be quite coarse as the solver will interpolate the wind field in between each point, but a high frequency is necessary to catch the turbulent fluctuations in the wind. At each discrete data point the wind is defined with velocity components in the three spatial coordinates.

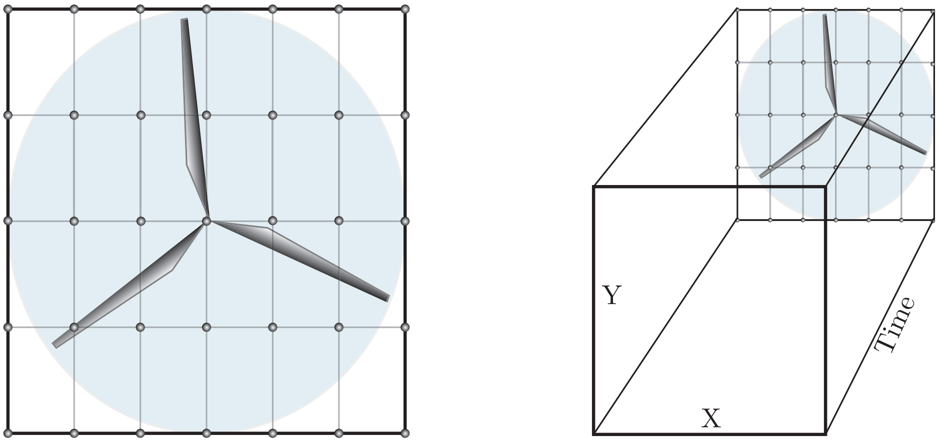

Figure 3.5: 3D wind history input

The wind history can be generated according to any turbulence model and with a given mean wind speed and standard deviation of the turbulence intensity. The IEC 61400-1 (3^{rd} edition) standard requires the use of either the *Mann model* or the *Kaimal model* [29].

The turbulence intensity is specified according the average turbulence intensity of the location of the turbine. IEC operates with turbulence classes A, B and C, which characteristics are shown in figures 3.6 and 3.7.

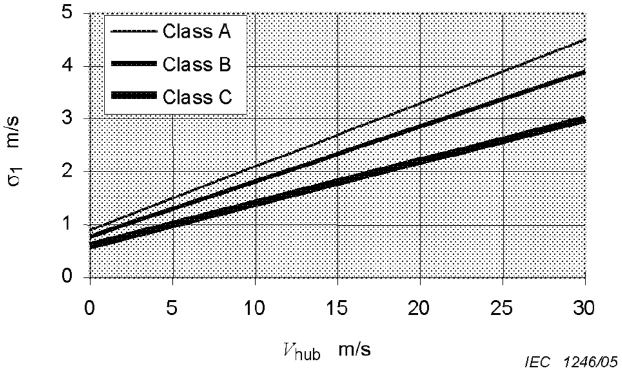

Figure 3.6: IEC turbulence standard deviation
Reproduced from [29]

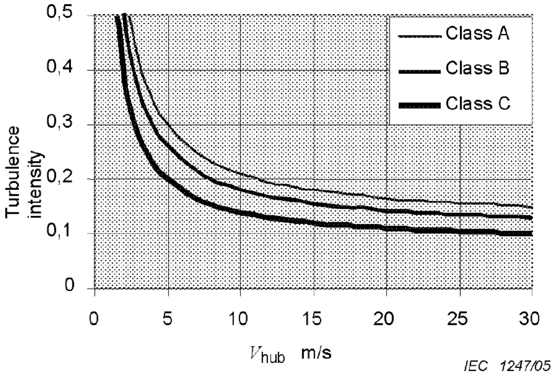

Figure 3.7: IEC turbulence intensity classes
Reproduced from [29]

Chapter 4

Dynamic loading and fatigue

In a vibrating and oscillating system, like a wind turbine, the dynamic loading play an important role. Often the fatigue damage due to dynamic loading will be the dimensioning criterion. For this reason it is important to know the characteristics of the various types of dynamic loading and how they affect the turbine. In the following, the dynamic loadings will be divided into periodic loads, which are due to the rotation of the turbine rotor, and transient loads, which are other dynamic loads such as wind gusts.

The periodic loadings contribute to oscillations that are a multiple of the rotor speed. The rotor speed frequency is commonly denoted 1P. This means that a 1P periodic loading will cause a 1P periodic excitations of a turbine blade as it passes through the swept rotor area, while the tower will be excited with a period of NP for a turbine with N blades. In this case the turbine has three blades so that the 1P blade loading will cause a 3P tower loading. This is illustrated by displaying the fast Fourier-transform (FFT) of the blade out-of-plane and the tower fore-aft motions in figure 4.2. The NP frequencies appear as peaks in the power spectrum.

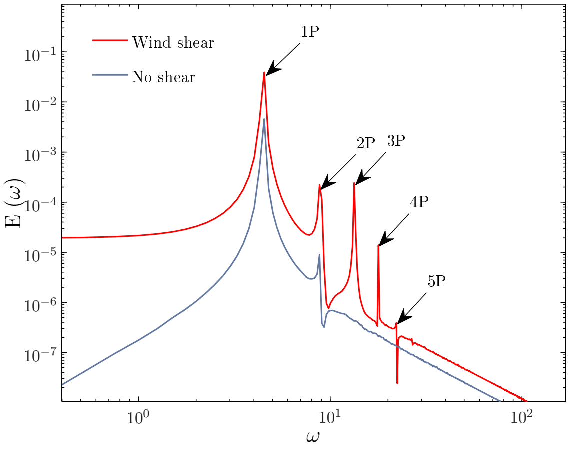

Figure 4.1: FFT: Blade motion with wind shear

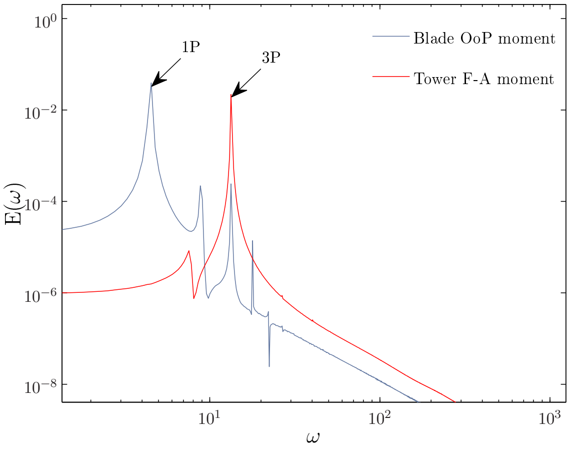

Figure 4.2: FFT: Tower and blade motion

Figure 4.1 shows the power spectrum of the out-of-plane loads on one blade with and without a wind shear. Including the wind shear, the cyclic loads are no longer purely sinusoidal and power spectrum peaks are found also at the higher harmonics. This is explained further in section 4.1.1 below.

4.1 Gravity load

The gravity load is an example of a perfectly sinusoidal load of frequency 1P. The gravity load is due to the weight of the turbine blade and causes a bending moment at the blade root which is a function of the azimuth angle ψ of the blade. The root edgewise moment will be zero when the blade is pointing directly up ($\psi = 0°$) or down ($\psi = 180°$) and have a maximum in absolute value when $\psi = \pm 90°$. A three-bladed wind turbine that is perfectly balanced will in theory not produce any gravity induced loads. To illustrate this, the gravity loads on the V27 rotor has been simulated with the aeroelastic model for a steady wind load and a constant rotor speed of 43 rpm. The result is shown in figures 4.3 and 4.4.

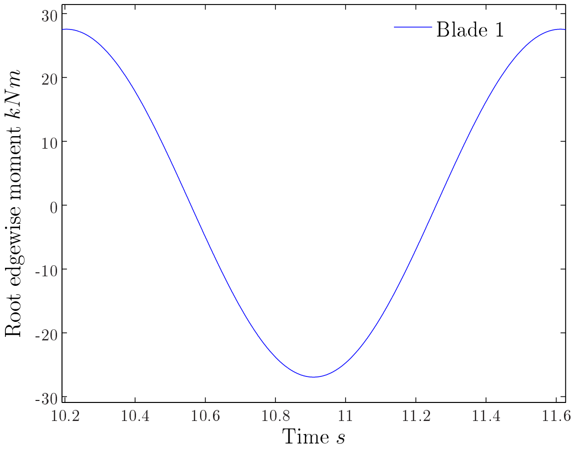

Figure 4.3: Gravity load on one blade

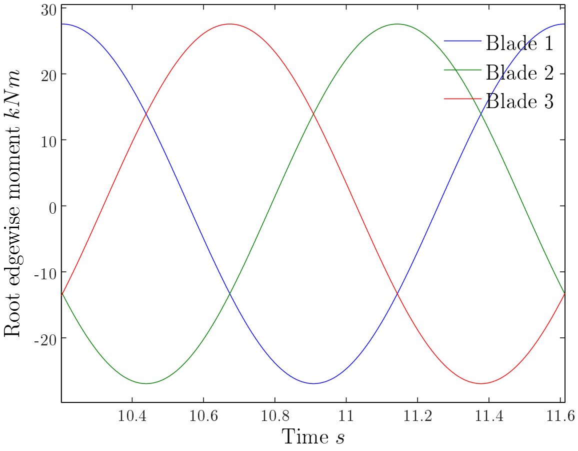

Figure 4.4: Gravity load on three blades

4.1.1 Wind shear

The wind shear effect, which is characterised by an increase of wind speed with altitude, is due to the boundary layer above the ground surface. The IEC 61400-1 standard requires the use of a wind profile as described by the power law in equation 4.1 with $\alpha = 0.2$.

$$V(z) = V_{\text{hub}}\left(\frac{z}{z_{\text{hub}}}\right)^{\alpha} \tag{4.1}$$

The wind shear will give an increased local wind speed when blades are pointing upwards compared to when they are pointing downwards as illustrated in figure 4.5. This will result in a 1P cyclic loading of the individual blade and a 3P loading of the tower. Because of the non-linear shape of the velocity profile, the loading cycles will not be completely sinusoidal. The small, but noticeable, deviation can be seen by inspection of the curves in figure 4.6. The influence of the wind shear on the power spectrum was shown in figure 8.2.

4.2 Tower shadow

The tower shadow effect is due to the interference of the tower on the flow through the rotor disk area. This effect is noticeable both in front of the tower for upwind rotors and behind the

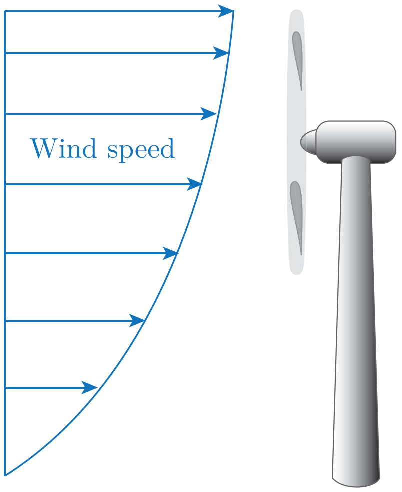

Figure 4.5: Wind shear

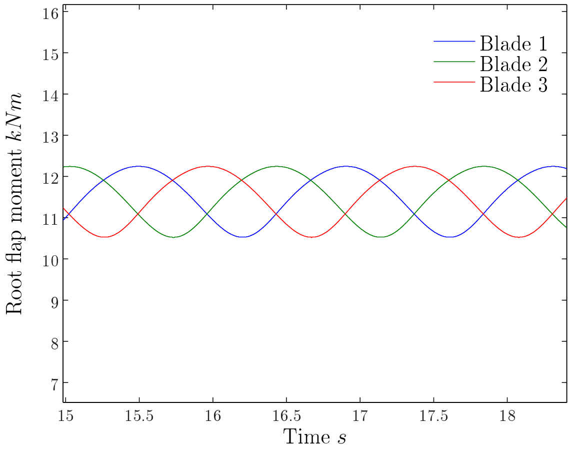

Figure 4.6: Wind shear loading

tower for downwind rotors. It is, however, a much larger tower shadow behind the tower than in front. The impact of the tower shadow on the airflow could be modelled by a potential flow solution (for upwind rotors) combined with an additional wake model (for downwind rotors). This is done in GH Bladed and HAWC II, but the FAST aerodynamic solver, AeroDyn, does unfortunately not have a potential solution at the moment, only a downwind wake model. Therefore it can only simulate the tower shade effect for downwind turbines. The Vestas V27 turbine is an upwind turbine, and the lack of a potential flow model in FAST calculations means that the tower shade effect will have to be ignored in all the aeroelastic simulations. Figure 4.7 shows an illustration of the effect of the tower shadow on the wind velocity profile in the area around the tower for an upwind turbine with a potential flow solution. Figure 4.8 shows the dynamics associated with the tower shade effect calculated in FAST for the V27 turbine, as it would appear if it had a downwind rotor.

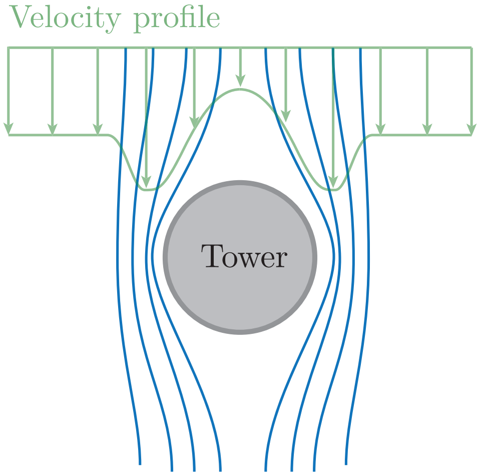

Figure 4.7: Tower shadow velocity profile

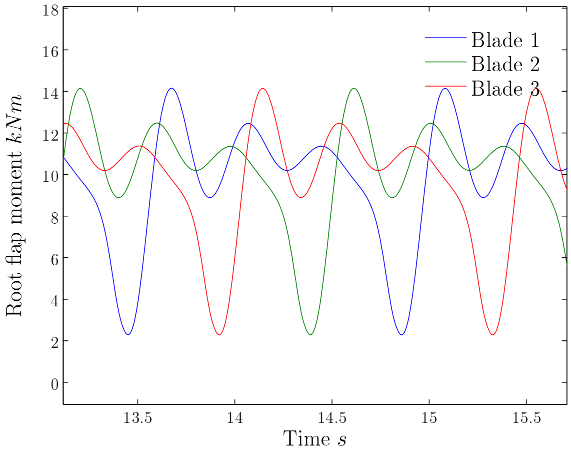

Figure 4.8: Downwind tower shadow loading

4.3 Yaw error

The yaw mechanism in wind turbines aligns the wind turbine rotor towards the wind direction to improve the efficiency and to avoid skewed inflow which will cause torsional loading on the tower. The wind direction can change fast, but the yaw inertia of the nacelle and the rotor is very large, which means that the yaw motion must be limited to avoid excessive gyroscopic loadings to the tower. Because of this, yaw errors commonly occur in wind turbines and contributes to dynamic loading.

A yaw angle misalignment causes a changing flow field around the airfoils as the blade moves through the swept area. As is seen in figure 4.9 both the relative wind speed V and the angle of attack changes for different azimuth angles ψ. Larger yaw errors will give larger variations in these parameters. For small yaw error angles the dynamic loading caused by this will behave relatively linear and produce a near-sinusoidal load variation cycle. The reason for this is the close to linear shape of the C_L-curve for small angles of attack that is common in many airfoil characteristics (See e.g figure 5.6). But when the yaw misalignment increases, the lift coefficient will start to move into and out of a partly stalled state and non-linear effects like dynamic stall will start to become visible. This is visualised in figures 4.10 and 4.11 for yaw angles of 5°and 20°respectively.

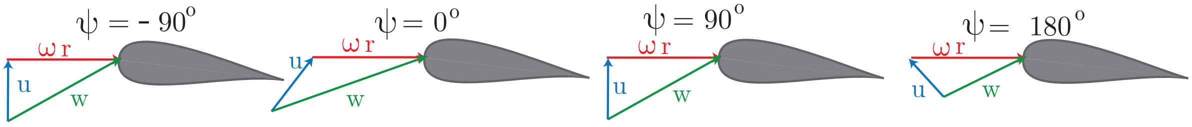

Figure 4.9: Change of relative velocity and angle of attack due to yaw error as a function of ψ

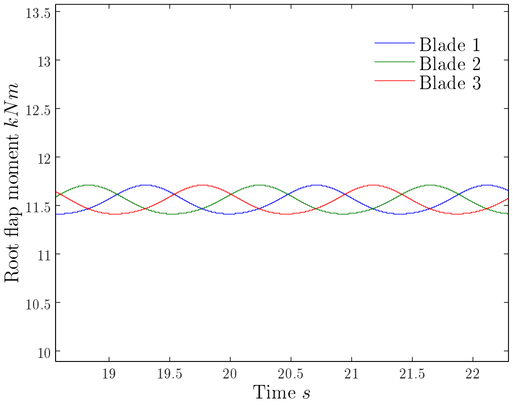

Figure 4.10: 5°yaw error

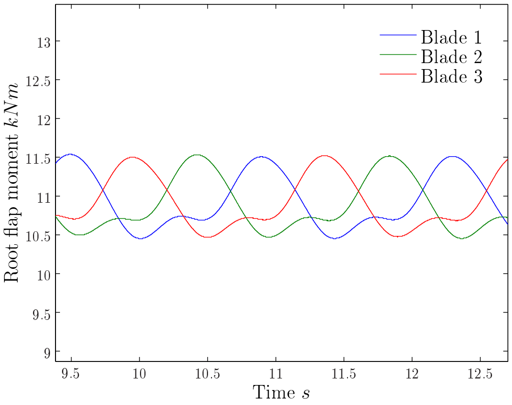

Figure 4.11: 20°yaw error

4.4 Wind inclination angle and shaft tilt

The effect of up-flow and shaft tilt is similar to the effect of yaw misalignment, as it is due to a misalignment of the wind speed angle and the rotor disk. The resulting dynamics are also similar, only shifted 90 °in azimuth angle relative to the yaw error loading. The difference is that while the yaw error is constantly changing and being actively compensated for, the shaft tilt introduces is a constant misalignment. The wind inclination angle is only somewhat dynamic as it is generally determined by the topology around the wind turbine. The Vestas V27 has 4 degrees of shaft tilt, and the location at Valsneset has approximately 0°flow inclination, as the area around the turbine is flat.

4.5 Fatigue damage

Wind turbines are often designed to have a life time of at least 20 years [14]. During that period they are constantly subject to fluctuating loads and structural vibrations. The deterioration and eventual failure of a material due to to such long time vibrations and cyclic loads is called fatigue damage. The stress amplitudes that causes fatigue damage are often much smaller than the stresses that causes static failure, and the damage is accumulated over a large number of cycles.

The damage originates at imperfections in the object material shape or structure, which causes stress concentrations, like a welded point or a bolt hole. The stress concentration initiates the development of a microscopic crack, and when subject to cyclic loading, the crack will slowly develop until a point where it eventually becomes unstable and cause the object to break.

4.5.1 SN-curves

A material's ability to withstand cyclic loading is often described using an SN-curve. The curve relates the stress-amplitude S of a load cycle with the number of cycles to failure N for a specific material. SN-curves for specific materials are found through laboratory testing, and SN-curves for commonly used materials such as structural steel are available in literature.

If the material properties are not known or the structure consists of several different materials it is common to use a model of the SN curve on the form:

$$N = KS^{-k} \tag{4.2}$$

Where K and k are material-specific materials. When expressed in logarithmic form, it becomes the linear relation:

$$\log N = \log K - k \log S \tag{4.3}$$

Thus it is common to approximate the SN curves as linear or partly linear slopes in a log-log reference system. A typical example is shown in figure 4.12, which shows a linear approximation of a real curve by two different slopes. By comparing equation 4.3 and the linear curve of figure 4.12 it can be seen that k, known as the Wöhler constant, is the slope of the SN-curve and that K is a material constant, setting the level of the SN-curve. In the linear approximation the subscript U denotes ultimate load, L denotes the end of the linear part of the curve, and ∞ denotes the endurance limit. The material can not withstand any load cycles above ultimate stress, but it can withstand an infinite number of load cycles below the endurance limit.

4.5.2 Palmgren-Miner rule

By assuming a linear relation between the stress cycles according to the SN-curve and the cumulative damage, the fatigue life can be predicted by the Palmgren-Miner rule.

$$D = \sum_{i=1}^{m} \frac{n(S_i)}{N(S_i)} \tag{4.4}$$

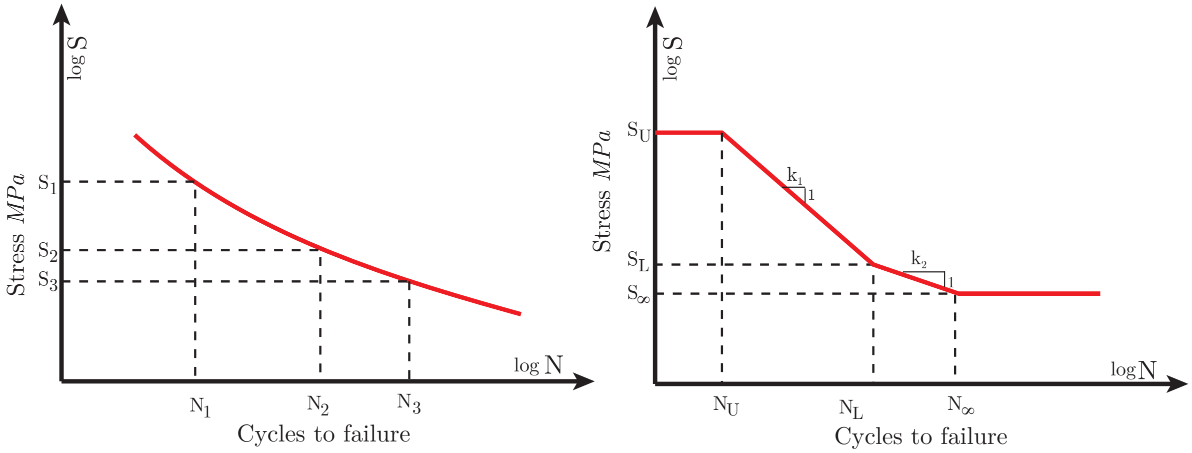

Figure 4.12: Example of experimental and linear approximated SN-curves

Here it is assumed that the stress history is counted and divided in m bins according to the cycle stress level S_i. n is the number of cycles of stress level S_i and N is the total cycles to failure of stress level S_i according to the SN-curve. The criterion for failure is $D \geq 1$.

4.5.3 Rain-flow cycle counting

The counting and binning of the stress-cycle history is done by rain-flow counting methods. The name refers to an analogy of raindrops falling on a pagoda-roof created by the stress-time history rotated vertically as illustrated in figure 4.13.

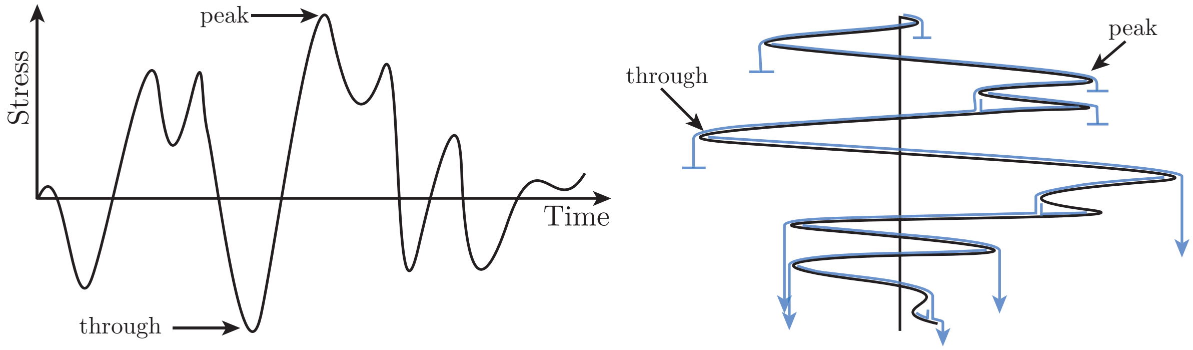

Figure 4.13: Pagoda-roof rain-flow counting analogy

The number of and amplitude of the stress cycles are counted according to the following rules [14].

1. A rain-flow starts from each through and peak.
2. A rain-flow continues until it intercepts a rain-flow started earlier.
3. A rain-flow started at a through stops when it meets a rain-flow started from a through larger than that of the current rain-flow.
4. A rain-flow started at a peak stops when it meets a rain-flow started from a peak larger than that of the current rain-flow.

The rain-flows ending in a bar in figure 4.13 has been counted according to the above rules, while the rain-paths ending in an arrow is continuing to run down the time series because none of the above rules have applied yet.

When a rain-flow is stopped, its travelled amplitude is found and categorized in one of the m bins according to its amplitude. The total number of cycles n within each bin i is then used to calculate the cumulative damages according to the Palmgren-Miner rule.

Chapter 5

Vestas V27 properties

The Vestas V27 is a 225 kW wind turbine with upwind rotor and pitchable blades. It is originally a fixed speed wind turbine, which can run at two different speeds due to a pole-shifting generator. The main specifications are listed in table 5.1.

Table 5.1: Vestas V27 specifications

Nominal power	225	kW
Number of blades	3	–
Rotor diameter	27	m
Hub height	31.5	m
Rotor moment of inertia	68760	kgm^2
Cut-in speed	3	m/s
Cut-out speed	25	m/s
Rotational speed	32.0/43.1	rpm
Power regulation	Pitch	–
Gearbox ratio	1 : 23.3	–
Aerofoil family	NACA 63-2XX	–

From references [45–47]

5.1 Generator

The generator in the Vestas V27 is a two-speed (pole shifting) squirrel cage induction generator. The generator specifications are provided in table 5.2.

The pole-shifting generator feature is possible due to a double set of stator windings which induces two different number of poles in the rotor. This configuration is common in fixed-speed wind turbines as it allows the turbine to rotate at two different speeds at low- and high wind speeds for increased power output: At low wind speeds the turbine rotates at 32 rpm, and when the wind increases and the generator power reaches a certain level, the generator is decoupled from the grid and the aerodynamic torque is used to accelerate the rotor to the next fixed rotation speed. When the rotor reaches 43.1 rpm and generator is rotating at 1000 rpm, which is its second synchronous speed, the generator is phased back on the grid, now using the second pair of stator windings.

The common way of implementing a generator in an aeroelastic simulation is to use one of the built-in generator models. FAST has the ability to model a generator as either a first

Table 5.2: Generator specifications

	6 pole winding		8 pole winding	
Nominal power	225	kW	50	kW
Synchronous speed	1000	rpm	750	rpm
Rated power speed	1009	rpm	756	rpm
Slip	0.9	%	0.8	%
Frequency	50	Hz	50	Hz
Voltage	3×690	V	3×690	V
Moment of inertia	7.4	kgm^2	7.4	kgm^2

From the Vestas V27 electrical manual [47]

order approximation or a Thevenin equivalent model. In addition, special generator configurations are available through a user-programmable subroutine. But because of the hydraulic transmission, the generator will have to be modelled in Simulink.

A typical torque-speed curve for an induction generator is provided in figures 5.1 and 5.2. The generator will be modelled by a first order approximation by equations 5.1 and 5.2.

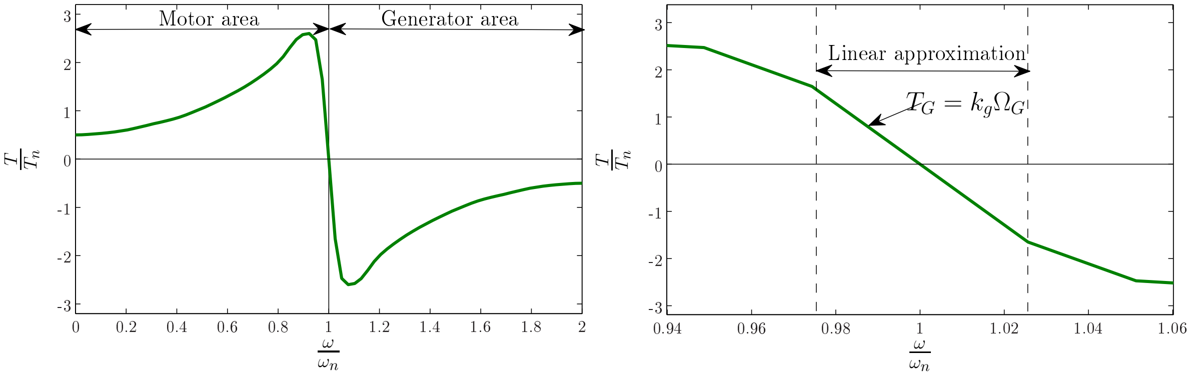

Figure 5.1: Generator torque curve

Figure 5.2: Linear generator area

$$T_G = k_g\Omega_G \tag{5.1}$$

$$\frac{\mathrm{d}\Omega_G}{\mathrm{d}t} = \frac{T_{\text{motor}} - T_G}{J_G} \tag{5.2}$$

This approach can only model the approximately linear part of the generator torque-speed characteristics around synchronous speed as explained in figure 5.2. This is a common approximation in dynamic wind turbine simulations, but it will not capture all the generator dynamics. If the generator performance is of special interest, a more detailed model should be used, but capturing the generator dynamics correctly would require very short time steps and consequently more time consuming simulations.

5.2 Pitch system

An example of a typical pitching system for a wind turbine is presented in figure 5.3.

The pitching motion is carried out by an hydraulic actuator at the root of each blade. The pitch actuator is in turn controlled by an hydraulic servo valve which is governed by the pitch

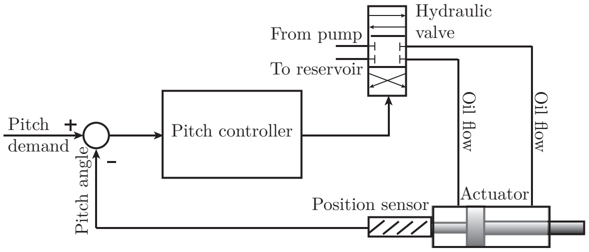
Hydraulic valve
From pump
To reservoir
Pitch demand
+
-
Pitch angle
Pitch controller
Oil flow
Oil flow
Position sensor
Actuator

Figure 5.3: Typical pitch system

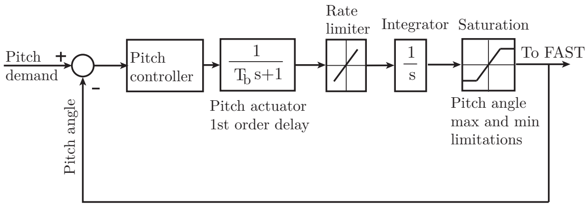
Pitch demand
+
-
Pitch controller
$\frac{1}{T_b s+1}$
Rate limiter
Integrator
$\frac{1}{s}$
Saturation
To FAST
Pitch actuator 1st order delay
Pitch angle max and min limitations
Pitch angle

Figure 5.4: Simplified Simulink model

controller. The pitch controller acts on the pitch error, which is the deviation of the actual pitch angle from the demand pitch angle. The actual pitch is measured by the position sensor on the hydraulic actuator, and the demanded pitch angle which is set according to the control scheme based on the wind speed and the generator power production.

The pitch system modelled in Simulink is simplified, as it does not model the hydraulics directly, but rather use a first order transfer function to include the dynamics associated with it. The most important features of the pitch system is, however, ensured by setting maximum pitch speed of $12°/s$ in the rate limiter box. The existence of pitch angle limitations due to the finite pitch actuator length is taken care of by the saturation block.

5.3 Aerodynamics

The geometry and structural characteristics of the turbine blades have been provided by Vestas (See appendix D). However, the lift- and drag characteristics of the aerofoils have not been provided. These characteristics are essential for simulation of the turbine, and they will therefore have to be found. The most reliable way of determining the aerofoil characteristics is by doing wind tunnel tests of each aerofoil section, but good estimates can be found by 2D calculations for small angle of attacks. Figure 5.5 illustrates common ways of determining the C_L and C_D curves.

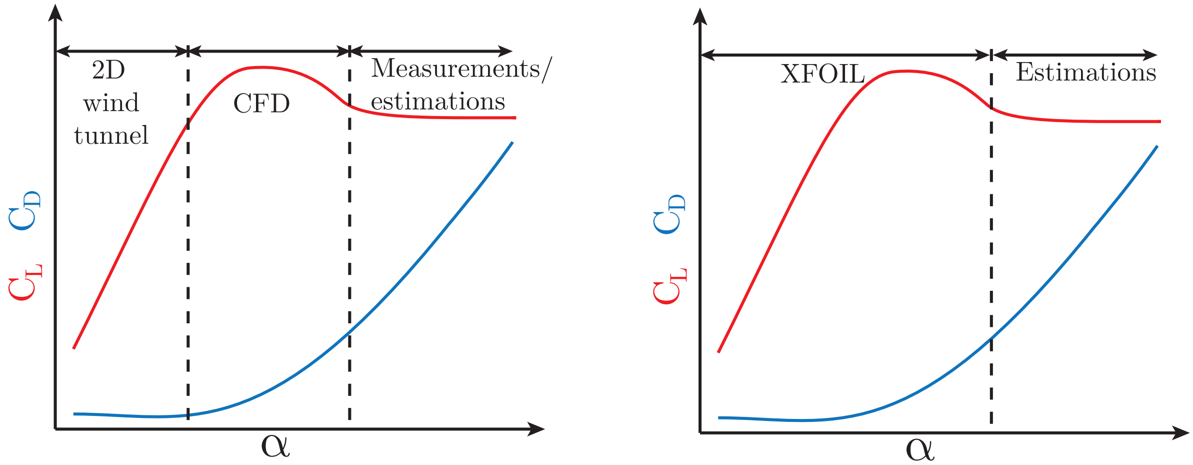

Figure 5.5: Approaches for determining C_L and C_D curves
Left: Approach suggested by [5]. Rigth: Approach used herein.

A number of codes exist that can calculate 2D aerofoil characteristics, most of them uses so called panel methods with viscous/inviscid interaction while others solve the full Reynolds-averaged Navier-Stokes (NS) equations. Panel methods have shown satisfactory results with low computational cost, while the NS approach is far more expensive, but also produces more accurate results in stall and post-stall areas [33]. A summary of commonly used panel codes is found in [33]. In this thesis, the XFOIL-code developed by Mark Drela [15] will be utilized.

XFOIL has a number of user-adjustable parameters which means that quite different aerofoil characteristics can be found for one aerofoil geometry. Consequently, the power curve of the Vestas V27 will be used for comparison with a power curve for the aeroelastic model turbine for verification of the aerofoil characteristics.

One of the user-adjustable settings is the transition criterion. The lift- and drag coefficients of an aerofoil are greatly influenced by the point of transition from laminar to turbulent flow. Laminar flow yields smaller drag and higher lift than turbulent flow. The accuracy of the lift- and drag curves are therefore highly dependent on accurate prediction of the point of transition. The point of transition depends in turn on the turbulence intensity in the wind and on the skin roughness of the aerofoil. The point of transition of a new turbine blade is located well away from the leading edge, but accumulation of bugs and dust on the leading edge during operation increases skin friction and causes earlier trigging of transition. To compensate for this effect, and because the free transition predictions of XFOIL are not always considered trustworthy [17], it is common to use forced transition in XFOIL. The location of this transition point varies slightly in literature, but reported values range between 2 and 12 % of the cord on the suction side and between 5 and 30 % on the pressure side [35, 39]. A numerical study of the transition point on a Nordtank 500 kW turbine has been carried out by Risøe National Laboratory in Denmark [40]. The transition point was found to vary between 2 and 30 % of the cord on the suction side and between 46 and 100 % of the cord on the pressure side of the blade for different spanwise positions. The transition point was found to be heavily dependent on the angle of attack, which means that a fixed transiton point may give incorrect results for large positive or negative angle of attack, i.e near and inside the stalled area. The Nordtank turbine is comparable to the Vestas V27 in that they are both pitch controlled and have quite similar aerofoil families (NACA 63-4XX for the Nordtank [38]).

The steady-state aerodynamic coefficients of the Vestas V27 rotor have been developed previously by master student Svein Kjetil Haugset at NTNU [25] along with the shape of the aerofoils. The characteristics were found by using a forced transition location of 10 % of the cord length on both sides of the aerofoil for all spanwise stations of the blade. The results, however, did not match the specifications from Vestas perfectly: The optimum pitch angle was found to be -4°, whereas the actual optimal angle was reported by Vestas to be between 0°and -1°. This discrepancy suggests that a too conservative transition criterion has been used. The explanation is found in figure 5.6 and 5.7: The local optimal angle of attack for an aerofoil is the point where the ratio C_L/C_D is maximum. Using a transition point further away from the leading edge (here shown with free transition), the slope of C_L/C_D in the linear area will be steeper, which results in a smaller optimal angle of attack. A transition point further away from the leading edge will therefore have the effect that the blade will have to be pitched less in negative direction, and thus correcting the optimal pitch setting towards the one reported by Vestas.

In Xfoil there are two different ways of influencing the location of the transition point. One is to set a forced transition point as explained above and the other is to change the transition criterion N_{crit}. The first is equivalent to having a physical turbulence trigger mounted at some fixed point of an aerofoil and the second is equivalent to changing the apparent turbulence level of the incoming airflow. The first method is the most commonly used but it may not

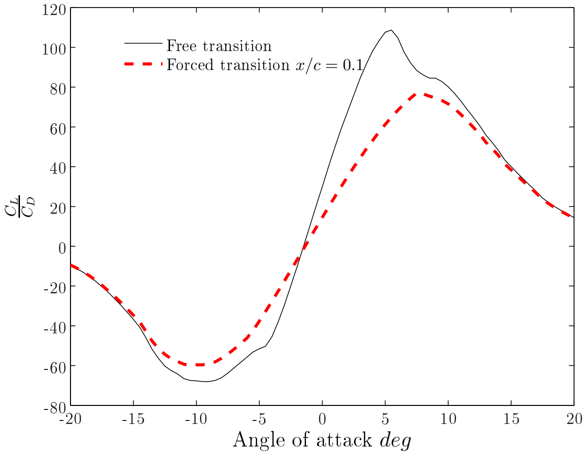

Figure 5.6: α_{opt} and transition point

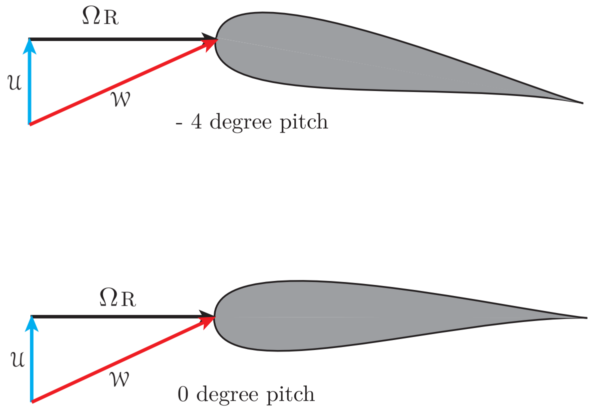

Figure 5.7: Change of α by -4°pitch

give satisfactory results for large positive or negative angles of attack. Such inflow situations may have transitions occurring further downstream on the aerofoil on either the pressure- or the suction side respectively, as shown in the mentioned Risø experiment. This type of inflow regime may be modelled by altering the N_{crit} parameter.

N_{crit} is the user specified limit telling when transition from laminar to turbulent flow will take place. The N_{crit} parameter is a part of the Orr-Sommerfeld equation, also known as the e^N method[1].

Tuning N_{crit}, however, requires some trial and error to find a suitable value. By assuming that the transition point should be found around 10 % of the cord on the suction side at Reynolds number correspondning to rated wind speed and at small positive angles of attack, a siutable N_{crit} parameter was found to be 0.2. The physical effect of using the proposed N_{crit} method as opposed to the forced transition method, is that the former will allow for more laminar flow around the aerofoil for flow situations with low Reynolds numbers. I.e for low wind speeds and near the hub of the blade where the relative wind speed is lower. This type of airflow behaviour agrees better with the expected physical behaviour. However, the method of tuning the N_{crit} parameter to model this is not well documented, and the results should be used with caution. In a report from Risø from 1995 where XFOIL calculations were compared with measured values, some tuning of N_{crit} was done: Aerofoil characteristics of the NACA 63-215 aerofoil was investigated for N_{crit} values of 7, 9 and 12. The best consistency with the empirical data was found at $N_{crit} = 7$, but the maximum lift was overestimated by 15% [33].

Because the local Reynolds number is heavily dependent on the wind speed and the rotational speed the lift and drag curves will not be similar for the lowest and the highest winds. Considering this is especially important when a forced transition point is not used, as low Reynolds numbers may then yield laminar flow over the entire aerofoil, whereas high Reynolds numbers may yield transition close to the leading edge. To account for this, the lift and drag curves were developed at both cut-in and cut-out wind condition and rotational speeds to allow interpolation of the airfoil characteristics in the aeroelastic code.

Figure 5.8 shows the calculated distribution of the transition points for the low Reynolds number (cut-in) case of 3 m/s wind speed and 17 rpm rotational speed. Figure 5.9 shows the calculated distribution of the transition points for the high Reynolds number (cut-out) case of 25 m/s wind speed and 43 rpm rotational speed. A summary of the parameters used in Xfoil to produce these results is found in appendix E.

---

[1] The transition point theory is further discussed in the XFOIL manual available from the XFOIL web page. [15]

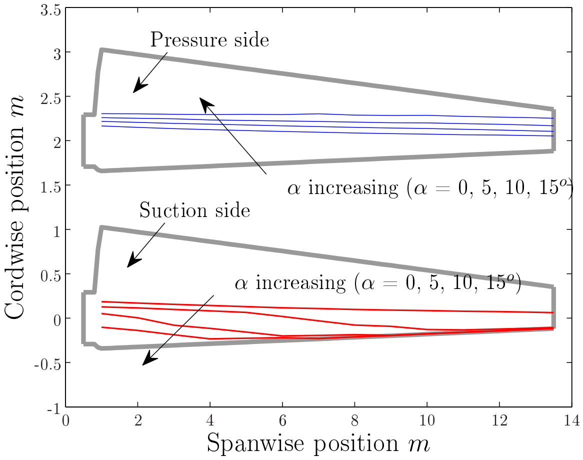

Figure 5.8: Transition lines at cut-in

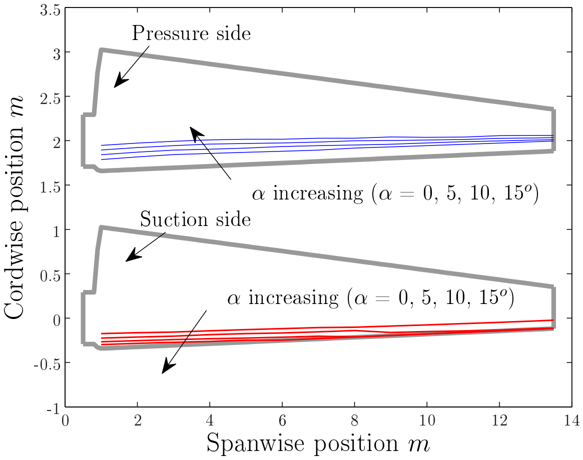

Figure 5.9: Transition lines at cut-out

The aerodynamic properties of the Vestas V27 turbine blades were calculated along with the transition points for the two Reynolds number cases above. These properties are the lift coefficient C_L, the drag coefficient C_D, and the pitching moment coefficient C_M. But as mentioned earlier, Xfoil only produces reliable coefficients for a limited range of angles of attack. For most practical applications this should be sufficient. But the aeroelastic solver uses an iterative procedure to calculate the forces, and it therefore needs the full range of angles of attack from -180°to +180°. The out-of-range coefficients can be estimated by using either flat plate theory or the Vitterna method [23]. These methods are not exact, but since the values in most situations will be used to ensure convergence within the original range of angles of attack, this does not reduce the overall accuracy of the code.

Extrapolation of the aerodynamic coefficients were carried out according to the Vitterna method, using an Excel tool called AirfoilPrep, which has been created by C. Hansen from Windward Engineering and is distributed through the NWTC web page [49]. AirfoilPrep was also used to calculate the Beddoes-Leishman dynamic stall coefficients that were mentioned in section 3.3.1. An example of extrapolated aerofoil properties are shown in figure 5.10.

Aerofoil properties similar to those of figure 5.10 were developed at 14 stations located along the blade as shown in figure 5.12 for both high and low Reynolds number cases. The aeroelastic solver can then interpolate between the lift ans drag tables for Reynolds numbers in between the cut-in and the cut-out case to improve the accuracy of the aerodynamic calculations. With the developed aerofoil characteristics the steady state power coefficient C_P was determined as a function of the tip speed ratio λ for a number of different pitch angles β. The steady-state C_P values were calculated by a code called WTPerf, which uses the blade element momentum (BEM) theory to compute the steady-state performance of wind turbines. The result is shown in figure 5.11. The graphs show that the optimal pitch angle setting of the newly developed blades is -1°. This compares well to the values specified by Vestas, which vary between 0 and -1 degree. The maximum power point is found at $\lambda_{opt} = 7.5$. The optimal tip speed ratio is an important parameter in variable speed turbines, as it defines the target rotational speed at below-rated wind speeds to ensure maximum power output from the turbine. The concept of

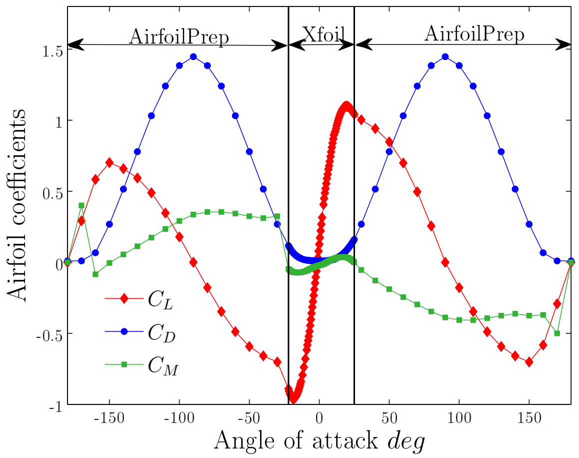

Figure 5.10: Extrapolated C_L, C_D and C_M

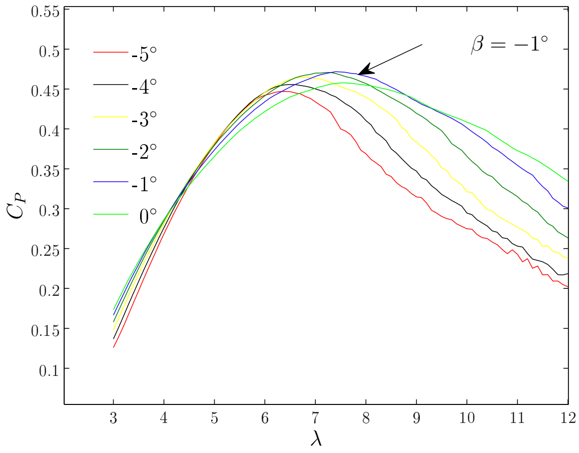

Figure 5.11: Optimal pitch angle β

variable turbine speed by maximum power point tracking is reviewed in section 9.1.1.

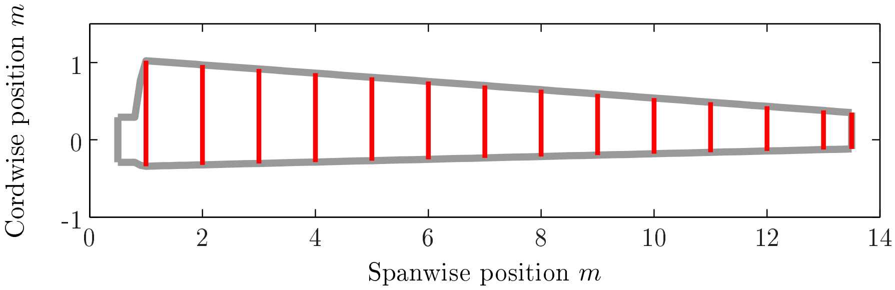

Figure 5.12: Blade station locations

With the developed aerofoil characteristics the power curves for the turbine is plotted in figure 5.13. The power curve is shown for two rotational speeds, because the original turbine has two rotational speeds, 32 *rpm* for low winds and 43 *rpm* for high wind speeds. The power curve of the original Vestas V27 turbine is also plotted for comparison. To compensate for the fact that the measured power is the electrical power delivered to the grid while the simulated power is the power on the main shaft, approximate drive train efficiencies of 90% and 85% are used for the two cases. The figure shows very good consistency between the measured power curve and the computed one. This suggests that the developed blade aerodynamics are quite accurate and that the simulated responses will be satisfactorily consistent with the real turbine response. However, a few discrepancies between the expected results of the aerodynamic investigations and what was found have been discovered: The C_L curves from XFOIL does not match the C_L curves from experimental data for the NACA 63-200 aerofoil series well. In figure 5.14 the discrepancy is shown for different aerofoil thicknesses throughout the blade. Both simulations and measurements are carried out with a Reynolds' number of 3 million. The graphs show that XFOIL yields too high lift coefficients, especially for thick aerofoils. This phenomenon is well known from other investigations [33]. The large discrepancy of the $C_L$max and the good consistency between the power curves suggest that the aerofoil series used on the actual turbine has better aerodynamic properties than the original NACA 63-200 series as tested by [1].

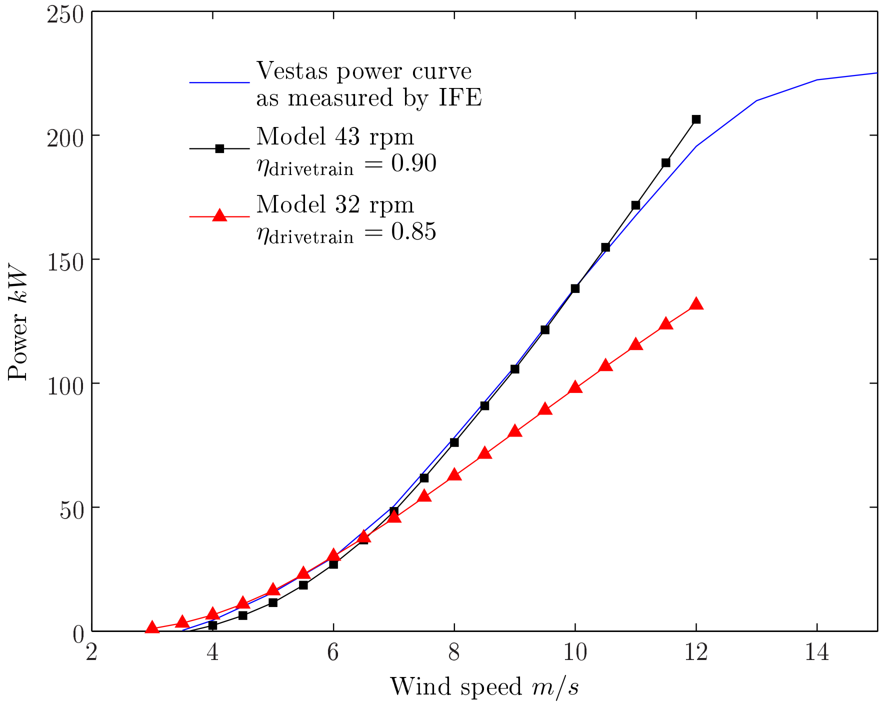

Figure 5.13: Measured and simulated power curves

The other discrepancy is the start-up pitch angle. The Vestas manual states that the turbine is programmed to start up with a pitch angle of 45°, while the maximum start-up torque for the aeroelastic model is found at approximately 65°, as is shown in figure 5.15. One would normally choose the pitch angle with maximum torque to ease the start-up of the turbine. This suggests that even if the developed airfoil characteristics match the power curve and the optimal pitch angle settings quite well they are not perfect.

5.4 Structural Dynamics

The aeroelastic code requires input of a number of blade and tower modal shapes. The vibration modes are calculated by finite element methods based on the mass and stiffness distribution of equivalent straight or twisted Bernoulli-Euler beams. The vibration modes of the tower and the blades are calculated by a program called Modes, which is capable of computing coupled mode shapes of rotating (blades) or stationary (tower) beams. The blades are assumed to be cantilevered at the blade root and the tower is assumed to be cantilevered at the base.

5.4.1 Blades

The basis for the creation of the mode shapes are the distribution of mass and stiffness of the tower and blades. For the blades, some structural properties have been provided by Vestas (see appendix D). The data provided in the section called *Bladedeflection and curvature* is believed to describe a test where the blade is cantilevered at the root and moments are applied normal to the twisted blade at a number of radial locations such that the blade is bent. Then the curvatures, deflections, stresses and strains are measured.

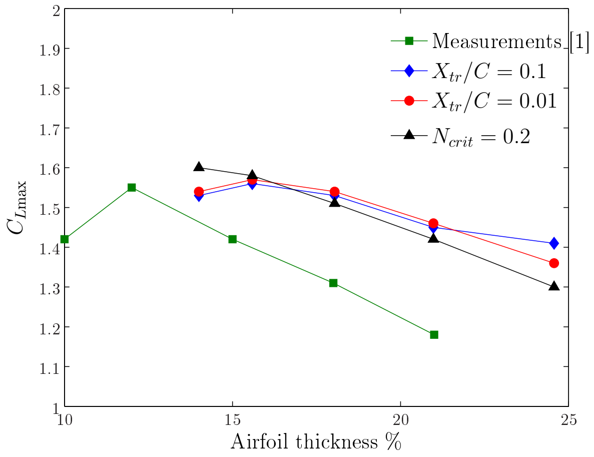

Figure 5.14: $C_{L\max}$ curves

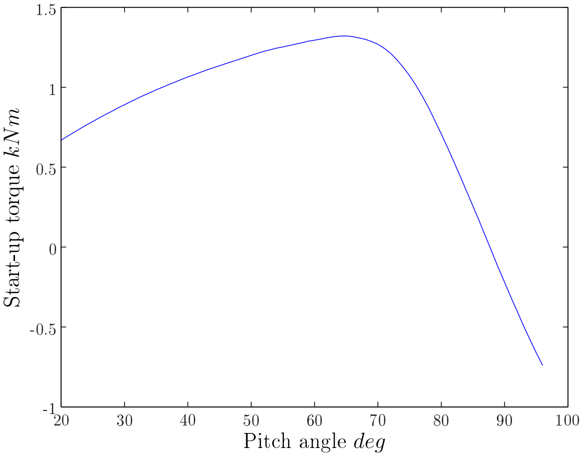

Figure 5.15: Start-up torque curve.

The flapwise stiffness can then be calculated by assuming that the blade is a straight uniform beam. Equation 5.3 describes the relations between the applied moments, the resulting curvature and the stiffness of such a structure [30].

$$\frac{1}{r} = \frac{M}{EI} \tag{5.3}$$

EI is the stiffness vector in Nm^2, M is the vector of applied moments and r is the resulting (local) radius of curvature of the beam. The resulting stiffness distribution is then plotted in figure 5.16 along with the stiffness distributions of a scaled version of the NREL 5 MW baseline turbine and the AWT C-27 turbine with 27 m rotor diameter, which are provided with the FAST archive [31]. The calculated flapwise stiffness of the V27 blade seems to be within a reasonable range compared to the others.

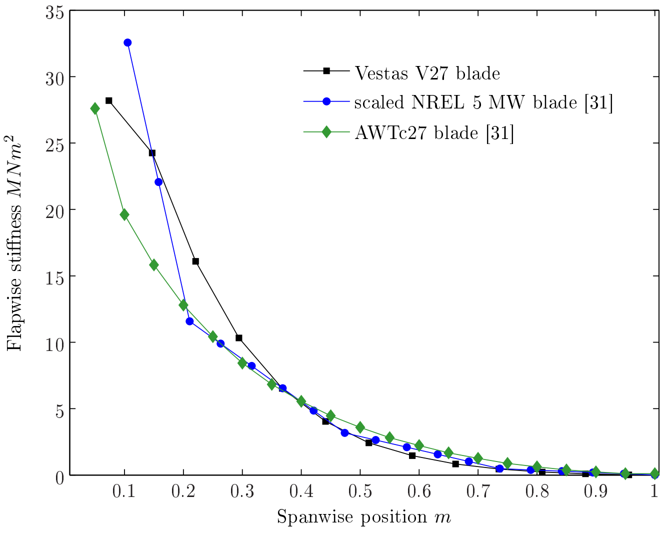

Figure 5.16: Flapwise stiffness distribution

The Vestas blade documentation [46] does not contain any information about the edgewise stiffness. In order to find a qualified estimate of this distribution a program called PreComp has been utilized. PreComp is specially designed to calculate the structural properties of isotropic laminated or composite wind turbine blades. PreComp needs detailed input of the internal structural geometry of the turbine blade and material data.

According to the Vestas blade documentation, the internal structure of the blade is as outlined in figure 5.17: It contains a central beam or spar, with thicker laminated surface than the rest of the shell, and it is held together with by two U-shaped webs. The U-webs run from near the root of the blade and almost to the blade tip and they serve as the main load bearing structure in the blade in spanwise and flapwise direction. The exact internal geometry and material properties of blade is, however, not known. Neither is the layout of the direction, thickness and number of the laminated plies as is required by PreComp. It has not been possible to obtain blade data of this detail level from Vestas, even for a discontinued wind turbine, as it is too close to their core technology. Instead a sample wind turbine blade, which was distributed with the PreComp package, was used as starting point: It was assumed that the directions, and thickness distribution of the different plies was applicable to the Vestas V27 blades, but that the number of plies would have to be adapted to create an approximate blade that would resemble the Vestas blade as close as possible. Also the material properties used could have to be changed, as the sample blade was constructed of glass-fibre reinforced polymer (GFRP), while modern turbine blades are built from a mixture of GFRP and carbon-fibre reinforced polymers (CFRP). Using CFRP gives stiffer and lighter turbine blades.

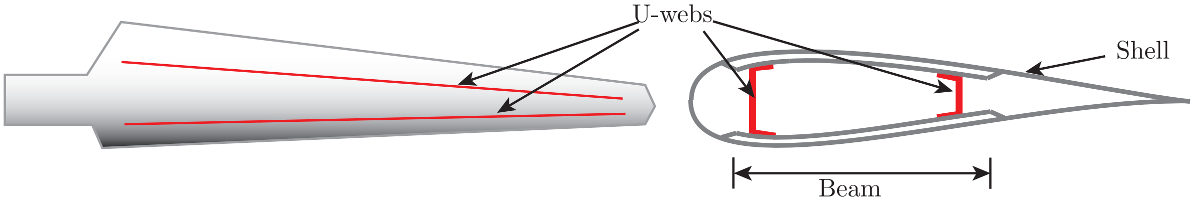

Figure 5.17: Blade interior geometry

By trial and error, the number of laminated plies was changed to match the weight distribution of the V27 blades as specified in the documentation. When the weight distribution was satisfactory, the modulus of elasticity of the GFRP was increased slightly (as would be the effect of introducing CFRP) until the flapwise stiffness distribution was satisfactory. The resulting turbine blade mass- and stiffness distributions are shown together with the original distributions from the V27 documentation. Now the structural properties of a turbine blade with the exact shape and approximate mass and stiffness distribution as the original blade had been created. And the blade that was created in PreComp had also got information on the stiffness distribution in edgewise direction. But because this data was found by roundabout ways with many possible sources of error, it needs some kind of verification: In figure 5.20 the edgewise stiffness distribution of the blade from PreComp is plotted together with a blade from the generic NREL 5 MW turbine [31]. The two distributions are plotted against the

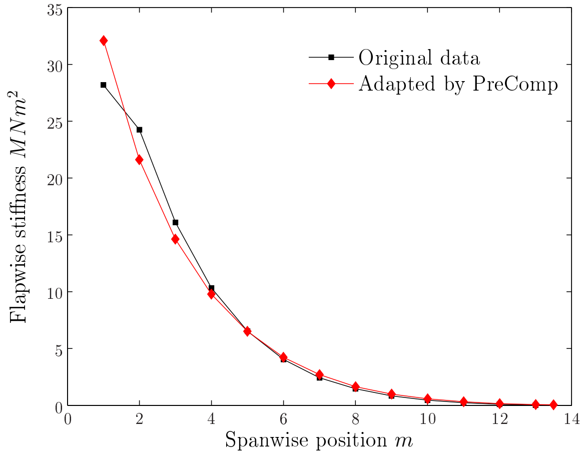

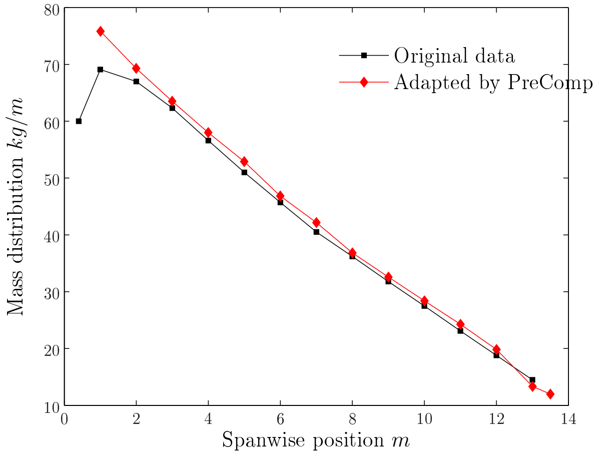

Figure 5.18: Flapwise stiffness

Figure 5.19: Mass distribution along blade

non-dimensional blade length and the NREL blade has been scaled so that the stiffness at 0.1 r/R is equal to the stiffness of the PreComp blade at the same spanwise position. The striking similarities of the two graphs suggests that sensible results have been produced, although it is not possible to tell exactly how accurate the result is, or if the resulting blade is softer or stiffer than the original. Until further verification of the blade stiffness, the result should be used with great caution.

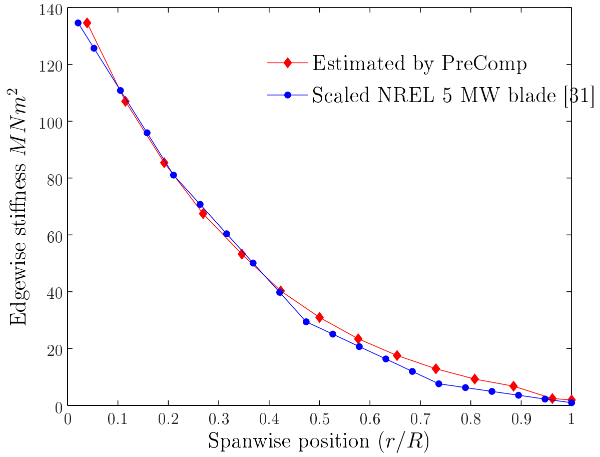

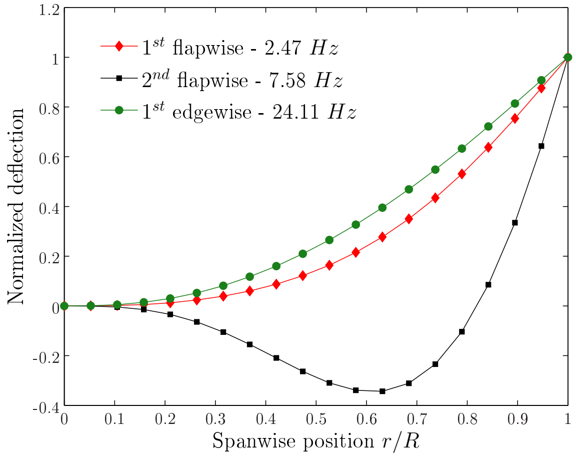

Figure 5.20: Edgewise stiffness distribution

Figure 5.21: Blade modal shapes

With the blade structural properties fully defined, the blade modal analysis was carried out. The resulting normalised mode shapes and natural frequencies are shown in figure 5.21.

5.4.2 Tower

The tower is a tapered, tubular tower. It consists of three parts of rolled conical steel tubes with thickness varying from 10 mm at the bottom to 6 mm at the top. The sections of different thickness are welded together, and the three parts are bolted together at the flanges. The exact tower geometry and other specifications are found in the Vestas documentation. The material is specified as Fe3608 mild steel. With this information, the tower stiffness distribution is calculated by inputting the geometrical and material properties into PreComp. Because a tubular tower is axisymmetric, the bending stiffness, the modal shapes and natural frequencies will be assumed to be equal in all directions. The first two tower modes and the corresponding natural frequencies are shown in figure 5.22.

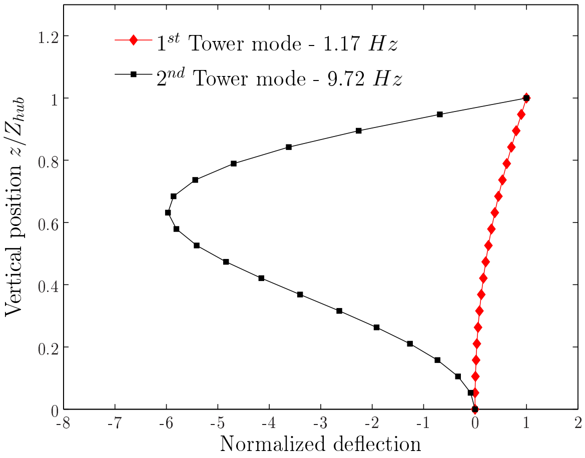

Figure 5.22: Tower modal shapes

Chapter 6

Hydraulic transmission

The principle and advantages of hydrostatic drives is well known and have been used for a long time in the mining industry. The advantage of the hydrostatic drive, besides its reliability, is the ability to supply a lot of power from a centralized pump through tubes or pipes to drive equipment in places where space and access is limited, or for other reasons an aggregate or electromotor is impractical. The idea of using the hydrostatic transmission as a drive train in a wind turbine, however, is quite new and this is the very heart of the ChapDrive concept. The principle of the transmission is outlined in figure 6.1.

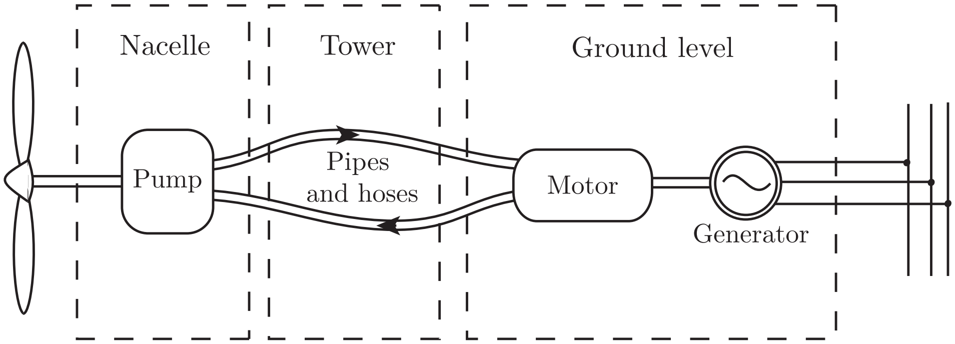

Figure 6.1: Principle of the ChapDrive hydraulic transmission

The complete hydraulic system on the modified Vestas V27 is a complex system including features for start-up and shut-down, safety systems, features for oil conditioning, heat exchange etc. The operation of these systems are important for the operation and reliability of the wind turbine, but they do not affect the power production during normal operation. For this reason, these auxiliary systems will not be considered herein, and they are not included in the simplified circuit diagram of figure 6.2.

Because the transmission is a closed circuit hydrostatic transmission, a boost system is required to compensate for the leakage flow through the seals of the pump and motor. The boost pump also serves to pressurize the low pressure side of the circuit to avoid cavitation in the inlet of the pump. Pressurizing the suction side of the pump is especially important for this system because the motor is placed on ground level while the pump is located in the nacelle. This gives an unfavourable suction head of 31.5 meters that could otherwise cause cavitation, with degraded pump performance and life time as a result.

The only safety system that is modelled is the safety release valve on the high pressure side of the circuit. The valve is normally closed, but it opens if the pressure exceeds the maximum

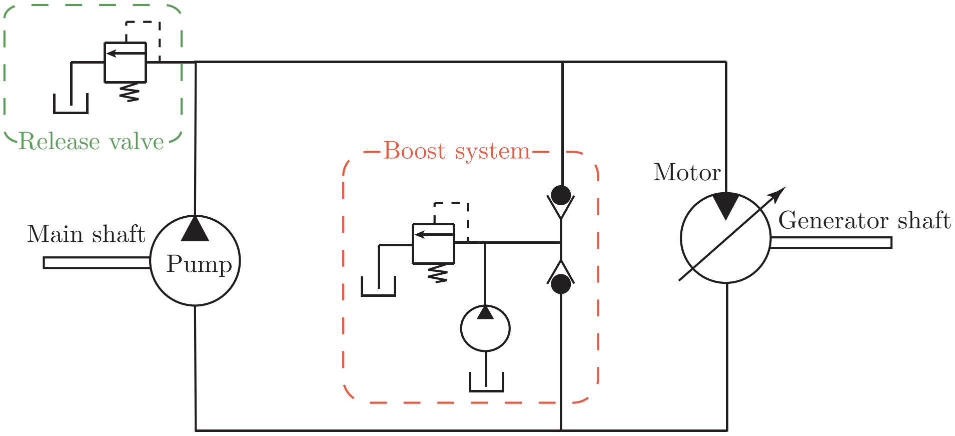

Figure 6.2: Hydraulic transmission circuit diagram

allowed pressure to relieve the circuit from dangerously high pressures.

The specifications for the hydrostatic pump, the boost system and the motor are given in table 6.1.

Table 6.1: Hydraulic transmission specifications

Max. oil pressure (Release valve)	350	bar
Boost pressure	25	bar
Main pipe Ø	58	mm
Main pipe length	82	m
Effective bulk modulus[1]	$1.0 \cdot 10^9$	Pa/m^3
Oil volume	216.7	ℓ
Pump displacement	11.3	ℓ/rev
Max. motor displacement	0.5	ℓ/rev
Oil kinematic viscosity	40	cSt
Oil density	870	kg/m^3
Motor internal leakage (C_{LM})	$14.5 \cdot 10^{-12}$	$m^3/s/Pa$
Motor drain leakage (C_{DM})	$8.87 \cdot 10^{-12}$	$m^3/s/Pa$
Pump internal leakage (C_{LP})	$9.05 \cdot 10^{-12}$	$m^3/s/Pa$
Pump drain leakage (C_{DM})	$4.38 \cdot 10^{-12}$	$m^3/s/Pa$

[1] Estimated. Smaller than the normal value of $1.5 \cdot 10^9$ Pa/m^3 because of tubes

The most important components in a hydrostatic transmission are the pumps and the motors. Displacement pumps and motors are mainly identical, only with opposite functionality in a hydraulic circuit. This means that the governing equations are the same, but the leakage and efficiency is defined differently. The equations governing displacement pumps and motors are listed in table 6.2.

The volumetric efficiency describes the amount of leakage oil with respect to the total oil flow through the pump and motor. The leakage includes both internal leakage from high pressure to low pressure side and external leakage to drain. The leakage flow is assumed linearly dependent on the differential pressure over the unit. This is a commonly accepted simplification because the leakage flow areas are small, so that the leakage resembles flow through very narrow orifices. This leads to a creeping flow that only depends on the pressure difference across the orifice when the absolute viscosity μ is constant [4,19]. The leakage flows introduce a loss in the

Table 6.2: Equations governing hydraulic power units

	Displacement pump	Displacement motor
Flow	$Q = \Omega_P D_P$	$Q = \Omega_M D_M$
Torque	$T_{\text{shaft}} = \frac{D_P \Delta p}{\eta_{\text{mech}}}$	$T_{\text{shaft}} = \eta_{\text{mech}} D_M \Delta p$
Power	$\mathcal{P}_{\text{shaft}} = \frac{Q \Delta p}{\eta_{\text{mech}}}$	$\mathcal{P}_{\text{shaft}} = \eta_{\text{mech}} Q \Delta p$
Drain leakage	$Q_{\text{drain}} = C_{DP} \Delta p$	$Q_{\text{drain}} = C_{DM} \Delta p$
Internal leakage	$Q_{\text{leak}} = C_{LP} \Delta p$	$Q_{\text{leak}} = C_{LM} \Delta p$
Volumetric efficiency	$\eta_{\text{vol}} = 1 - \frac{Q_{\text{drain}} + Q_{\text{leak}}}{\Omega D_P}$	$\eta_{\text{vol}} = \frac{\Omega D_M}{\Omega D_M - (Q_{\text{drain}} + Q_{\text{leak}})}$

circuit, but they also have an impact on the system dynamics. The leakage acts as a damping feature in the hydraulic circuit, and the increased damping with increased pressure should give an advantageous dynamic response of the system.

6.1 Pump and motor characteristics

The pump is a Hägglunds CA 210-180 radial piston pump. The efficiency diagram of the pump is shown in figure 6.3 with the wind turbine target speed-torque locus plotted on top to illustrate the operating efficiencies. The pressure loss as a function of rotational speed is plotted in figure 6.4. These curves are implemented in the Simulink model to simulate the losses in the hydraulic circuit related to the pump.

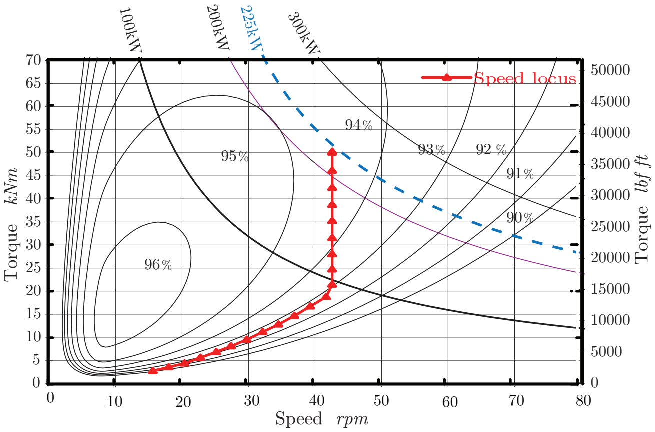

Figure 6.3: Pump total efficiency diagram
Reproduced from [27]

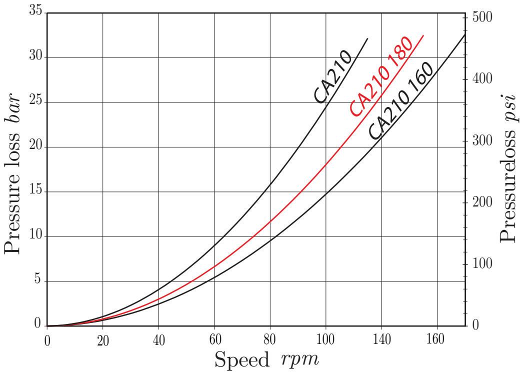

Figure 6.4: Pump pressure loss diagram
Reproduced from [27]

The efficiency characteristics for the actual hydraulic motor, a Bosch-Rexroth AV6M 500 cm^3 axial piston motor, has not been found. But the motor is quite similar to the motors that are installed in the NEG Micon NM52 wind turbine that was investigated in the project thesis. In lack of better efficiency characteristics, the efficiency curves for that motor will be used to simulate the losses in the hydraulic circuit. The efficiency coupling with pressure and motor displacement α is reproduced in figures 6.5 and 6.6.

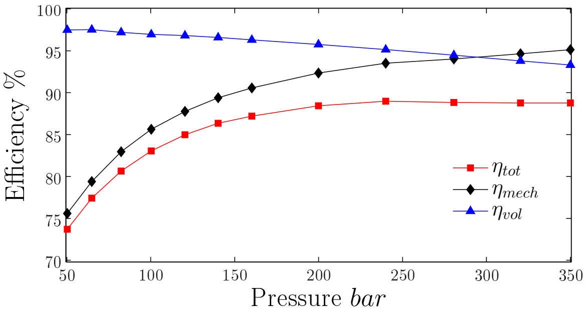

Figure 6.5: Motor efficiency at 1200 rpm Bosch-Rexroth A4VSG 1000 cm^3 [16]

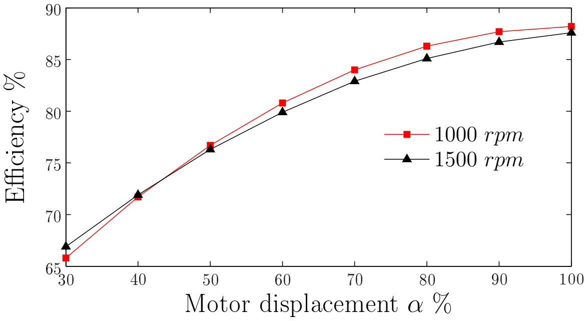

Figure 6.6: Swash-efficiency diagram Bosch-Rexroth A4VSO 750 cm^3 [16]

6.2 Pipe flow and pressure

In a hydrostatic transmission, the ratio of the pump and motor displacement resembles a gear box, and in the same manner the string of hydraulic fluid resembles a shaft transferring power between the two units. Normal wind turbine transmissions have thick steel shafts with so high torsional stiffness that the shaft dynamics often can be ignored. A hydraulic transmission will have relatively low stiffness in comparison, and this means that the drive dynamics will play an important role in the overall response of the turbine. The dynamics of the hydraulic circuit are modelled by by including leakage and friction (damping), compressibility (compliance) and fluid inertia (inertia).

The fluid compliance enters the calculations through the compressible continuity equation:

$$\frac{\mathrm{d}p}{\mathrm{d}t} = \frac{\beta}{V}(Q_{in} - Q_{out}) \tag{6.1}$$

The rate of change of pressure p in a pipe is determined by the bulk modulus β and the flows into and out of the pipe volume V. Here β is the effective compliance modulus of both the fluid and the pipes/tubes in the circuit. Steel pipes are quite rigid and will not influence the bulk modulus to any extent. Tubes, on the other hand, are more flexible and even steel-lined tubes will cause a noticeable decrease in the effective bulk modulus.

The pressure depends on net flow of oil into and out of the high pressure and low pressure pipes. The net flow can be expressed in terms of the displacement volumes, rotational speeds, boost flows, leakage flows and relief valve flows. The diagram in figure 6.7 shows the flow paths in the two separated fluid volumes, which are the high and low pressure pipes. Based on this figure the net flow rates can be expressed in equations 6.2 and 6.3.

$$\Delta Q_{HP} = (\Omega_T D_P - \Omega_G D_M) - (C_{LM} + C_{DP} + C_{LP})\Delta p - Q_{\text{drain}} \tag{6.2}$$

$$\Delta Q_{LP} = (\Omega_G D_M - \Omega_T D_P) - C_{DM}\Delta p + (C_{LM} + C_{LP})\Delta p + Q_{\text{boost}} \tag{6.3}$$

The leakage coefficients used in the simulations are found in table 6.1.

The frictional losses are calculated using the Darcy-Weissbach equation:

$$\Delta p = \frac{f \ell \rho v^2}{2D_{pipe}} \tag{6.4}$$

The friction factor f depends on whether the flow is turbulent or laminar. The thumb rule is that the flow is laminar for Reynolds numbers smaller than 2300 and fully turbulent flow is

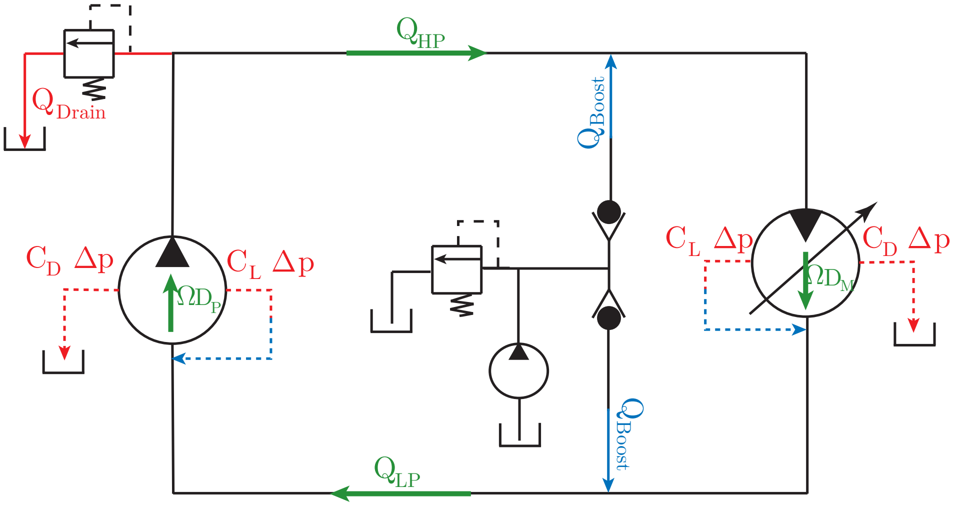

Figure 6.7: Hydraulic transmission flow paths

assumed for $Re > 4000$ [50] and a weighted average should be used in between. In the model, a simplified approach will be used with laminar flow below $Re = 2300$, and turbulent above. A summary of the friction theory used in the model is given in table 6.3.

Table 6.3: Viscous friction model

	Laminar	Turbulent
Reynolds number	$Re < 2300$	$Re > 2300$
Theory	Poiseuille	Blasius
Friction factor	$f = \frac{64}{Re}$	$f = \frac{0.3164}{Re^{0.25}}$

Only the main circuit is taken into consideration when calculating the frictional losses. And a pipe diameter of 58 mm is considered for the entire circuit, although hoses with other diameters are used in connection with pump/motor. Bends in the circuit are not considered, although they also would contribute to the pressure losses. The inaccuracy due to this is assumed small, as the frictional loss is of minor importance for the overall dynamics.

The fluid inertia is the inertia due to the mass of the fluid, $m = \rho \ell A$. When the fluid is accelerated a dynamic pressure will build up according to Newtons second law, so that:

$$\frac{\mathrm{d}v}{\mathrm{d}t} = \frac{\mathrm{d}Q}{A_{pipe}\mathrm{d}t} = \frac{\sum F}{m} = \frac{\Delta p A_{pipe}}{\rho \ell A_{pipe}} \tag{6.5}$$

Assuming that the unknown property Q is the average flow through the pipe, then:

$$Q = \frac{Q_{in} + Q_{out}}{2} \tag{6.6}$$

Rearranging equation 6.5 then yields the pressure change due to inertia:

$$\Delta p_{\text{inertia}} = \frac{1}{2}\frac{\mathrm{d}(Q_{in} + Q_{out})}{\mathrm{d}t}\frac{\rho \ell}{A_{pipe}} \tag{6.7}$$

6.3 Simulink model

The Simulink model is too large to present in the thesis. Instead the interested reader is referred to appendix F.

Chapter 7

Aeroelastic and quasi-steady aerodynamic model comparison

As mentioned earlier, two different models have been developed. One is the aeroelastic, fully dynamic model, and the other is a quasi-steady model. The two models have the exact same hydraulic transmission and generator implementation. The only difference between the two is the aerodynamics. The aeroelastic model can read in full field 3D wind files and calculate dynamic response of the turbine blades as they rotate through a transient and spatially varying wind field. The quasi steady model does not do blade element calculations, but it is rather based on the average performance of the wind turbine in a spatially averaged wind field. To ensure that the wind input is as equal as possible, the wind input to the quasi-steady model is the wind speed record from the point in the very centre of the hub at the aeroelastic model.

The main purpose of the simplified model is to serve as a verification of the FAST/Simulink combination. Although the short-term transient dynamics probably will be quite different, the two models should still have quite similar responses on a macroscopic scale.

7.1 Aeroelastic model

The characteristics, capabilities and shortcomings of the aeroelastic code has already been covered in section 3. The FAST model is implemented in the Simulink environment through a MEXw32 block function. The FAST block takes the the high speed shaft power and torque as input along with the yaw and pitch angles, and returns a number of aerodynamic parameters as specified by the user. The implementation of the FAST block in Simulink is shown in appendix F.

7.2 Quasi-steady model

In the quasi-steady model, steady-state coefficients will be used to simulate the dynamic response. This will not produce exact responses to quick changes in wind speed, but it is a common approach and it produces satisfactory results in most situations. The rotor power and torque is defined in equations 7.1 and 7.2, in terms of the non-dimensional power (C_P) and torque coefficients (C_Q)).

$$P_{\text{aero}} = \frac{1}{2}\rho\pi R^2 C_P(\lambda,\beta)\mathcal{V}^3 \tag{7.1}$$

$$T_{\text{aero}} = \frac{1}{2}\rho\pi R^3 C_Q(\lambda,\beta)\mathcal{V}^2 \tag{7.2}$$

Where the tip-speed-ratio λ is defined as

$$\lambda = \frac{\Omega_{\text{rotor}} R}{\mathcal{V}} \tag{7.3}$$

When the blade geometry and the lift and drag characteristics of the airfoils are known, the power coefficient can be calculated using a steady state BEM program. In this case, WTPerf was chosen to do the steady BEM calculations as was done in section 5.3 to find the optimal pitch setting. WTPerf uses the same format of the input files for the aerodynamic properties as the aeroelastic solver AeroDyn. This ensures good conformity between the aeroelastic model and the steady-state model.

The tip-speed-ratio λ is commonly used to express the C_P coefficient in a dimensionless frame of reference, as λ represents the non-dimensional relative wind speed over the airfoil. The representation of C_P as a function of λ for different wind speeds is nearly correct, but a small error will occur because of the change in Reynolds-number with changed relative wind speed as can be seen in figures 7.1 and 7.2. The peak of the C_P curve at 17 *rpm* is shifted to slightly higher λ-values than at 43 *rpm*, but the difference is so small that it is not necessary to interpolate between the two tables in the quasi-steady model. The aerodynamic torque will be calculated from equation 7.2 by using that

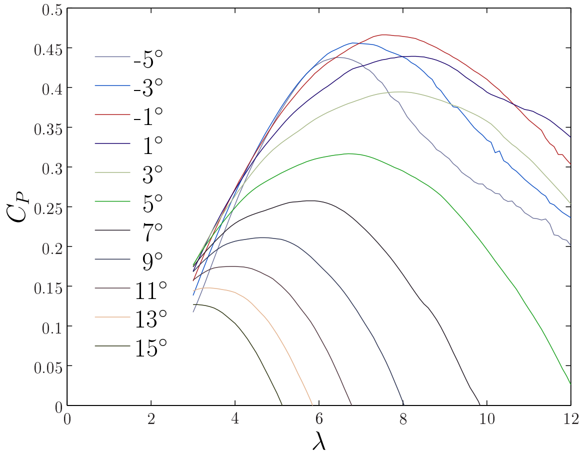

Figure 7.1: $C_P(\lambda, \beta)$ at 17 *rpm*

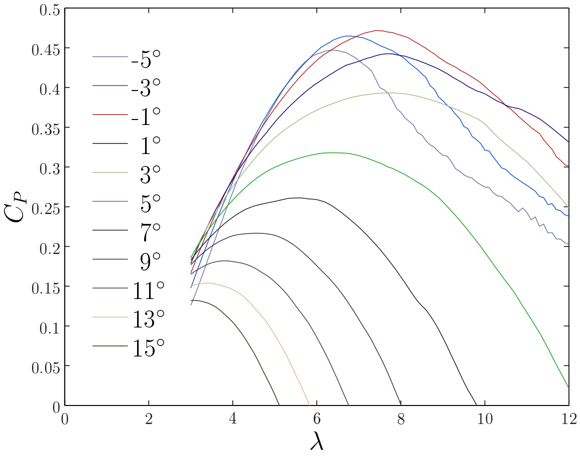

Figure 7.2: $C_P(\lambda, \beta)$ at 43 *rpm*

$$C_Q(\lambda, \beta) = \frac{C_P(\lambda, \beta)}{\lambda} \tag{7.4}$$

The change of rotor speed is then calculated according to Newtons second law in angular direction:

$$\frac{\mathrm{d}\Omega_{\text{rotor}}}{\mathrm{d}t} = \frac{T_{\text{aero}} - T_{\text{pump}}}{J_{\text{rotor}}} \tag{7.5}$$

The parts of the block diagram of the quasi steady model that differs from the Simulink block diagram of appendix F are shown in appendix G.

7.3 Comparison

To compare the two models they were run with similar wind input and similar control actions for constant rotor speed of 43 *rpm*, no pitch control and a mean wind speed of 12 m/s. The result is plotted in figure 7.3.

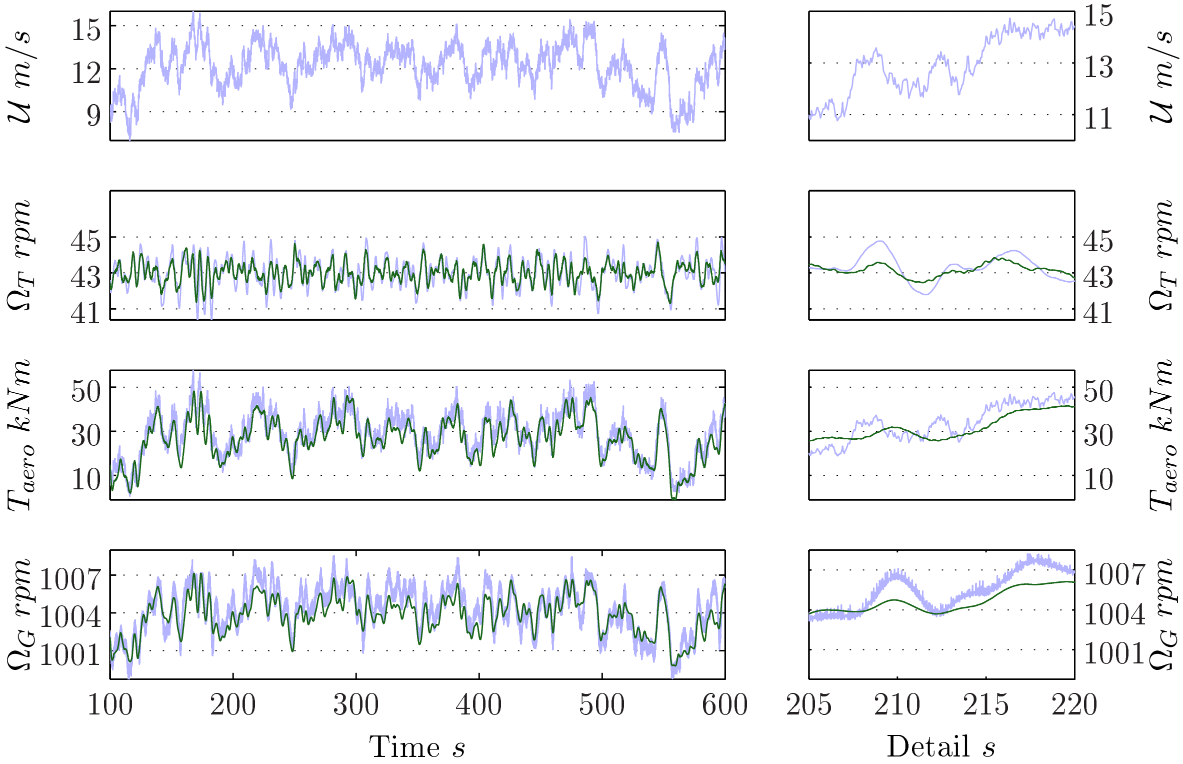

Figure 7.3: Model comparison at 12 m/s mean wind speed with detailed view. Light blue line is quasi-steady model. Dark green line is aeroelastic model.

The two simulations are quite similar, but some important observations can be made from the overview plot: Firstly, the oscillations in the generator speed,Ω_G, is larger for the simplified model. The explanation is related to the wind input to the model: Remember that the wind input to the simplified model was taken from the hub height wind history of the aeroelastic model to ensure similar wind conditions throughout the simulation. The difference occurs because the aeroelastic model uses a 3D wind wind field with spatial variations over the swept area so that small wind gusts and turbulence are smoothed out, while the simplified model uses the same wind speed input over the entire rotor area. The effective wind speed variations of the simplified wind turbine rotor will therefore be larger and thus also the rotor speed oscillations. Also the bending of the blades due to a sudden wind gust will have a smoothing effect.

Secondly, the aerodynamic torque T_T and the generator speed Ω_G is generally a little higher for the simplified model compared to the aeroelastic. The generator speed follows the aerodynamic torque to a large extent, so the two results are related and due to a difference in the treatment of the aerodynamics. Some of this difference can be due to deflections of the blades in the aeroelastic model, but most of it is simply due to the lack of wind shear in the simplified model. Because of the non-linearity of the shape of the wind shear, the average wind speed over the rotor area of the aeroelastic model is slightly smaller than the wind speed of the quasi-steady rotor.

When looking at the detailed views more differences become apparent: The Ω_T curve is smoother for the quasi-steady model. The reason for this is again the lack of wind shear: The shear causes a 3P oscillation of the rotor speed in the aeroelastic model that is not found in the simplified model.

The most important difference is found in the graph of Ω_G: The quasi steady model has small amplitude, high frequency oscillations in the generator speed while the aeroelastic curve is completely smooth. The reason for this is not fully understood, but it may have to do with instabilities due to lower damping in the quasi-steady model or it may be related with numerical instabilities.

The general conclusion that can be drawn from this comparison is that the aeroelastic model with the FAST/Simulink coupling produces sensible results, but comparison with measured data is necessary to explore how the model relates to the actual turbine.

Chapter 8

System frequencies and frequency response simulation

A wind turbine designer must bear in mind that a wind turbine is most of all a vibrating system of long, slender beams subject to an environment of heavy loading in a broad-band frequency spectrum. To avoid excessive damage of the turbine, the designer must ensure that none of the dominant frequencies overlap and cause resonance problems. The two most severe cases that must be avoided is the coincidence of the following frequencies:

- The first or second in-plane blade vibration mode, the drive train torsional frequency and the first or second tower side-to-side mode. Coincidence of any or all of these frequencies may cause side-to-side oscillations of the tower or oscillations in the rotor speed. The latter can quickly destroy the gearbox in a geared turbine or damage the generator in a direct drive turbine.
- The first or second out-of-plane blade mode, the fore-aft tower modes and the blade passing frequency and its higher harmonics (i.e 1P, 3P, 6P and 9P). Coincidence of any or all of these frequencies may cause dangerous fore-aft tower oscillations or out-of-plane blade oscillations that may cause a blade hitting the tower. The 1P excitation only occurs if there is a rotor imbalance due to icing etc.

Of course, the aim here is not to design a turbine, but because of the modifications made to the system by introducing the hydraulic drive train and variable speed there is a possibility that any of these situations can occur. If so, this must be addressed in the control system, and special care must be taken to avoid prolonged or permanent operation on these frequencies.

The blade and tower modes are already known from section 5.4, but they are only calculated for one speed and one no pitch angle. Pitching of the blade will cause decomposition in the in-plane and out-of-plane directions so that the vibration modes change according to the pitch control strategy, but this is treated in section 8.2. In addition, the drive train natural frequency will have to be found.

8.1 Drive train natural frequency

8.1.1 Linear approximation

If the boost pump operation and relief valves are neglected a hydrostatic transmission can be modelled as a rotating mass-spring-damper system as illustrated in figure 8.1. In the figure,

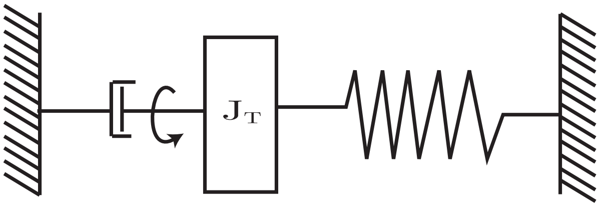

Figure 8.1: Hydraulic mass-spring damper analogy

the spring's right side is attached to a rigid non-rotating reference. The equivalent of this in the hydraulic circuit would be a non-rotating, entirely closed motor, which is not very interesting. But it would also be equivalent to a motor rotating at fixed speed, which is a good approximation (0.9% generator slip), and a fixed displacement volume. In reality the motor displacement will be varied constantly, and thus changing the drive train natural frequency. Opening up the motor swash will decrease the frequency, while closing the swash will increase it.

The pump torque is expressed in terms of the differential pressure, known as the load pressure Δp_{load}:

$$\mathcal{M} = (p_h - p_l)D_P = \Delta p_{\mathrm{load}} \tag{8.1}$$

The load pressure is in turn dependent of the oil accumulation ΔQ and the compressibility modulus β:

$$\Delta p_{\mathrm{load}} = \beta(\frac{\Delta Q_{\mathrm{h}}}{V_{\mathrm{h}}} - \frac{\Delta Q_{\mathrm{l}}}{V_{\mathrm{l}}}) \tag{8.2}$$

When θ is the angular displacement offset of the pump from dead-state, and the high and low pressure volumes are equal, the equation can be written as:

$$\Delta p_{\mathrm{load}} = \frac{\beta}{V}(Q_{\mathrm{h}} - Q_{\mathrm{l}}) = \frac{\beta}{V}(2\theta D_P - C_L \Delta p_{\mathrm{load}}) \tag{8.3}$$

Where C_L is the combined leakage coefficient of the motor and the pump. Inserting this into equation 8.1, the angular moment equation becomes:

$$\mathcal{M} = (p_h - p_l)D_P = \frac{\beta}{V}(2\theta D_P^2 - \cancel{C_L \Delta p_{\mathrm{load}}}) \tag{8.4}$$

To simplify the analysis, the leakage flow is cancelled in the equation, as it is small in comparison with the pump flow. The hydraulic spring constant equivalent is then found by dividing the torque on the angular displacement offset:

$$k = \frac{\mathcal{M}}{\theta} = \frac{\beta}{V}(2\theta D_P^2) \tag{8.5}$$

Then the undamped natural frequency is found by:

$$\omega_0 = \sqrt{\frac{k}{J_T}} = D_P\sqrt{\frac{2\beta}{V J_T}} \tag{8.6}$$

The hydraulic damping is approximated by the following equation [21]:

$$\zeta = \frac{\beta C_L}{2V J_T} \tag{8.7}$$

If the system is under-damped ($\zeta < 1$), the inclusion of the damping term changes the natural frequency according to

$$\omega_1 = \omega_0\sqrt{1-\zeta^2} \tag{8.8}$$

Because of the large volumes and long pipelines, the hydraulic damping will be negligible, as can be seen in table 8.1. Table 8.1 shows the assumed best and assumed worst cases of the hydraulic natural frequency with regards to the variation of the bulk modulus, but the results should be verified by measurements. The bulk modulus β varies with pressure and temperature, undissolved entrained air, but so so also the various leakages and the use of flexible hoses. All these dependencies complicates the calculation of the bulk modulus. A common engineering value for β is 1.5 GPa. In the table, it is assumed that the bulk modulus lies between 1.5 and 0.8 GPa, due to flexible hoses and air, which is a sensible range [21]. The result is that the drive train frequency is very uncertain.

Table 8.1: Drive train natural frequency

		Low frequency		High frequency		Modelled	
Bulk modulus	β	1.5	GPa	0.8	GPa	1	GPa
Damping	ζ	$4.7 \cdot 10^{-6}$	–	$4.7 \cdot 10^{-6}$	–	$4.7 \cdot 10^{-6}$	–
Undamped frequency	ω_0	0.21	Hz	0.15	Hz	0.17	Hz
Damped frequency	ω_1	0.21	Hz	0.15	Hz	0.17	Hz

8.1.2 Non-linear approach

The natural frequencies that are given in table 8.1 were based on the assumption of no boost or relief valve flows, so a few comments on the simplifications and the validity of these equations are in its place: In addition to effect of the motor displacement that was discussed above, the leakage into and out of the system also play an important role. The leakage terms were assumed negligible earlier, and this may be a fair assumption. But a different kind of leakage will play an important role: When the pressure level in the high pressure pipe exceeds the release valve pre-set pressure of 350 bar, the valve will open and bleed off the excess volume. The opposite happens in the low pressure pipe, where a boost pump refills oil when the pressure falls below 25 bar.

Introducing the boost system in the calculation changes dynamics noticeably. For low to medium wind speeds the boost system keeps the low pressure almost constant while the high pressure varies with the aerodynamic torque. An example of this is shown in figure 8.1.2. Note the different scales on the y-axes.

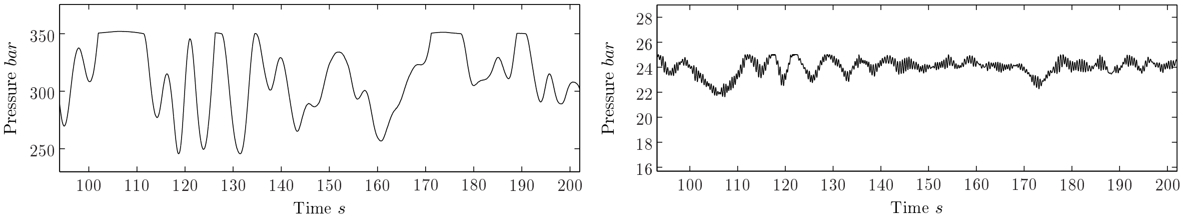

High pressure oscillations

Low pressure oscillations

Figure 8.2: Normal high and low pressure levels

The equation for the load pressure is still dependent of the oil accumulation ΔQ and the compressibility modulus β. But with the low pressure level constant the load pressure is now only dependent on the oil accumulation in the high pressure pipe. Neglecting the leakage flows the load pressure becomes:

$$\Delta p_{\text{load}} = \frac{\beta}{V}(\theta D_P - \frac{\Omega_G}{\Omega_T}\theta D_M - \cancel{C_L \Delta p_{\text{load}}}) \tag{8.9}$$

Performing a similar derivation as in section 8.1.1 the natural frequency then becomes:

$$\omega_0 = D_P \sqrt{\frac{\beta(1 - \frac{\Omega_G D_M}{\Omega_T D_P})}{V J_T}} \tag{8.10}$$

This equation is highly dependent on the operation point, as both Ω_T and D_M are variable. The highest possible natural frequency is found when $D_M = 0$. Then the natural frequency becomes:

$$\omega_0 = D_P \sqrt{\frac{\beta}{V J_T}} \tag{8.11}$$

With the system parameters, this frequency is 0.12 Hz. Equation 8.10 also states that the motor displacement can be governed in such a manner that the dynamics of the drive train disappears completely, if $\Omega_G D_M = \Omega_T D_P$.

If the system should start to oscillate such that the relief valves are frequently in operation the boost system may not be able to keep a constant pressure level in the low pressure pipe. And the result will be highly irregular oscillations, which may cause trouble for the governor. Two graphs illustrating the irregular oscillations in the high and low pressure pipes due to boost- and relief valve operation are shown in figure 8.1.2.

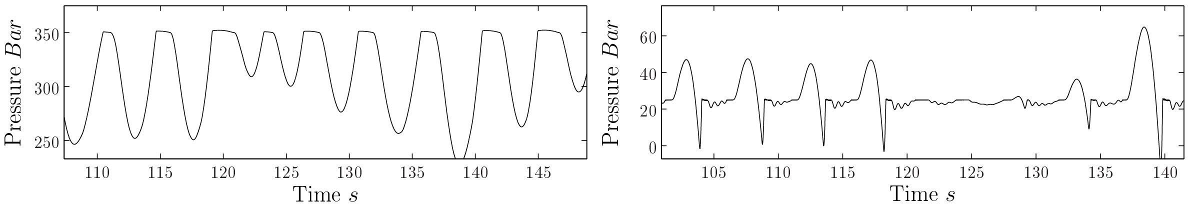

High pressure oscillations

Low pressure oscillations

Figure 8.3: Irregular pressure oscillations due to boost and relief valve

The conclusion is that the calculated drive train frequency from 8.1.1 is the highest possible natural frequency. The real frequencies will probably be lower and vary quite a bit, hence the wide shaded area in the Campbell diagram of figure 8.4.

8.2 Campbell diagram

The Campbell diagram is tool for indicating possible resonance frequencies of rotational machinery. The system frequencies are plotted on the y-axis against the rotational speed of the machine to highlight rotational speeds where resonant behaviour are expected. The points of interest are the triple-crossings, i.e where an nP rotational harmonic, a structural mode and the rotor speed interferes.

The Campbell diagram for the wind turbine is plotted in figure 8.4 and 8.5. The diagonal, dashed lines are the nP harmonics of the rotor speed and the almost horizontal, solid-drawn lines are the structural vibration modes. The triple-crossings are the points where a dashed line crosses a soild-drawn line within the turbine speed range. Around the rated turbine speed of 43 rpm the turbine will start to pitch according to the pitching scheme shown in figure 9.2. When the blades are pitched, the flapwise and edgewise direction are changed relative to the in-plane and out-of-plane directions. The in-plane and out-of-plane modes are decompositions of the flapwise and edgewise vibrations. So when the blades are pitched, the in-plane and out-of-plane frequencies change accordingly, as can be seen in the figures. The shaded envelopes appear because the pitch can have a wide range of values for one rotational speed around rated power, as the pitch and speed controllers act independently.

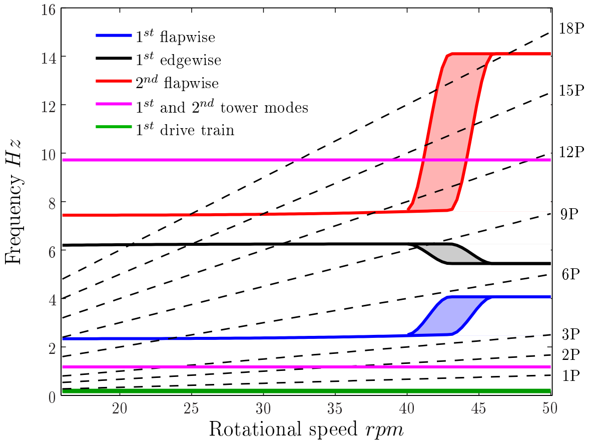

Figure 8.4: Campbell diagram

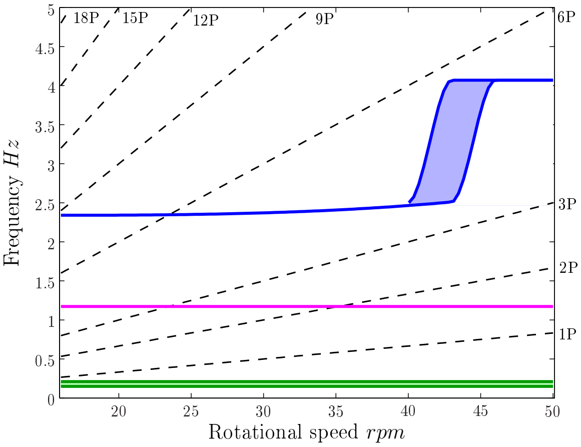

Figure 8.5: Campbell diagram detail

A few frequencies are found to be of special interest: At 23.5 rpm a double point of interference is found. Firstly the first flapwise mode crosses the 4P blade passing frequency. Secondly the first tower mode crosses the 3P blade passing frequency. The first of these occurrences would normally not be very dangerous, as the 4P frequency are not one of the dominant ones. The second occurrence probably needs special attention in itself, as the 3P is the dominant blade passing frequency that excites the tower. When these two occurs at the same rotor frequency, one must expect that oscillations may occur. If this is found to happen during testing of the turbine, one should consider to implement means to pass this rotor frequency fast in the control system. A suggestion to such a method is presented in [7], but that method requires good control over the rotor speed. It is not obvious that it would work for the hydraulic transmission with its low stiffness.

Another interesting frequency is at 31.2 rpm. Here the first edgewise and the 6P frequencies cross. This should not be a serious problem, but again, it may be of interest when designing the control system if any oscillations are found evident in the simulations.

The third point that calls for attention is in the pitched area. The second tower mode crosses the second flapwise blade mode. However, the secondary vibration modes have considerably less energy than the primary ones, and when considering that this frequency interference is also present in the original turbine, this should probably not cause any oscillations.

To check if the mentioned frequencies were evident in the time domain simulations of the turbine a frequency analysis was carried out, and four power spectral density (PSD) diagrams are shown in figure 8.2. All of the predicted dominant frequencies could be seen in the aeroelastic simulations.

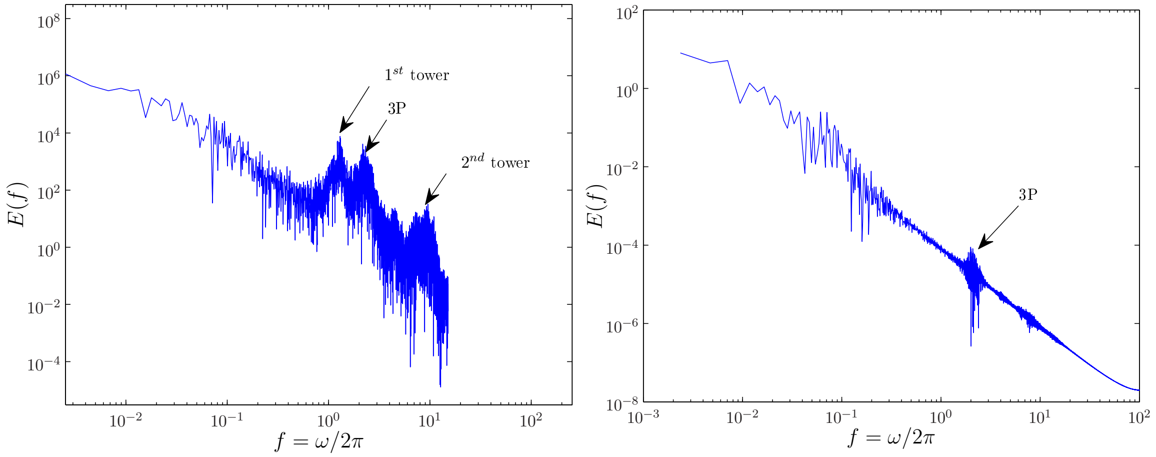

Tower fore-aft motion

Rotor speed

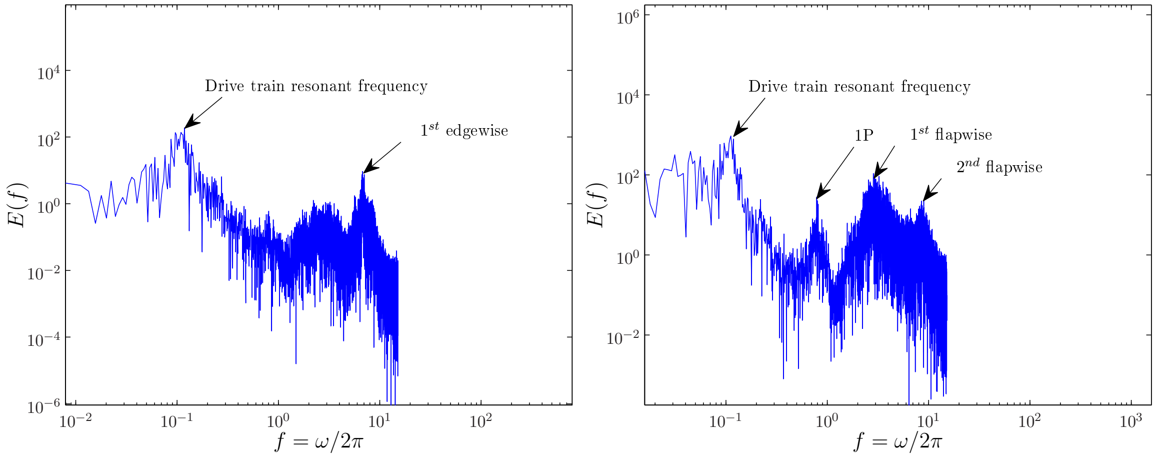

Blade in-plane motion

Blade out-of-plane motion

Figure 8.6: PSD plots showing the dominant system frequencies

8.3 Frequency responses in the non-linear system

Frequency response plots, known as amplitude-phase-frequency (APF) diagrams, are useful tools when designing controllers. APF diagrams show how the expected system behaviour varies according to the frequency of the input signal. In linear systems these are often used for stability analysis and prediction of the phase margin ψ and gain margin ΔK_p and to tune the controller parameters.

Non-linear systems must be linearised before one can utilize the linear control tools, but that can be a very challenging task for complex systems like the one considered herein. A linear analysis is carried out in section 10.2.1 and in appendix A, but in addition, an effort was made to create a Matlab program that could do a frequency response analysis directly on the full, non-linear systems.

A frequency analysis can be carried out on any system simply by applying a sinusoidally varying load or by changing the governing apparatus in a sinusoidal manner. This is a fairly common way of doing dynamic analysis on real applications. It is for example being used in hydro power applications in order to determine the dynamics of the waterways and to test the controller performance.

Doing a frequency analysis this way is of course a time consuming task, as the lowest relevant frequencies may be in the order of minutes. And to get a good result the system must be able to stabilise before moving on to the next frequency. The advantage of using this approach is that it is much more accurate than a linear analysis, as all the physical effects automatically are included. In theory one could then produce perfect frequency response diagrams, but because of the time issue one can only analyse a finite number of frequencies. The result is that while the general trend will be found, one might overlook important dynamic effects occurring in narrow bands.

Because the wind turbine has two independent control systems, a tool has been created to apply a sinusoidal input signal to each of the controllers and to analyse the response of the time domain simulation and plot it in a logarithmic APF diagram.

8.3.1 Speed control frequency response

Frequency response of the speed controller is done by inputting a sinusoidally varying signal with a sequence of different frequencies on the speed controller. The controller will then act on what it believes is the actual deviation and try to eliminate it by opening and closing the motor swash. The result is that the pressure in the high pressure line will be varied accordingly, eventually causing the turbine rotor oscillate. Then the amplitude ratio is found by comparing the amplitude of the input signal with the amplitude of the rotor speed oscillations, and the phase lag is found by measuring the time between the respective peaks and dividing by the input period.

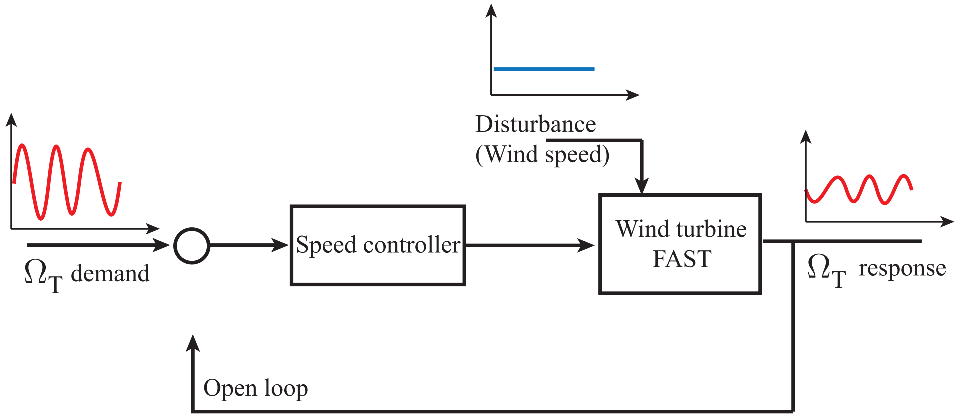

Figure 8.7: Turbine speed frequency response block diagram

Figure 8.7 shows principle of the frequency response simulation. To create a representative image of the system dynamics, the analysis must be carried out for different wind speeds and possibly also for different input amplitudes. The reason for this is that the system is inherently non-linear, and the aerodynamic power increases by the power of three. This means that although the simulations will be carried out with a constant wind speed the, steady state level of the wind speed will probably have an influence. In figure 8.8 the frequency response shows that the system behaviour is fairly constant: The response varies moderately with steady state

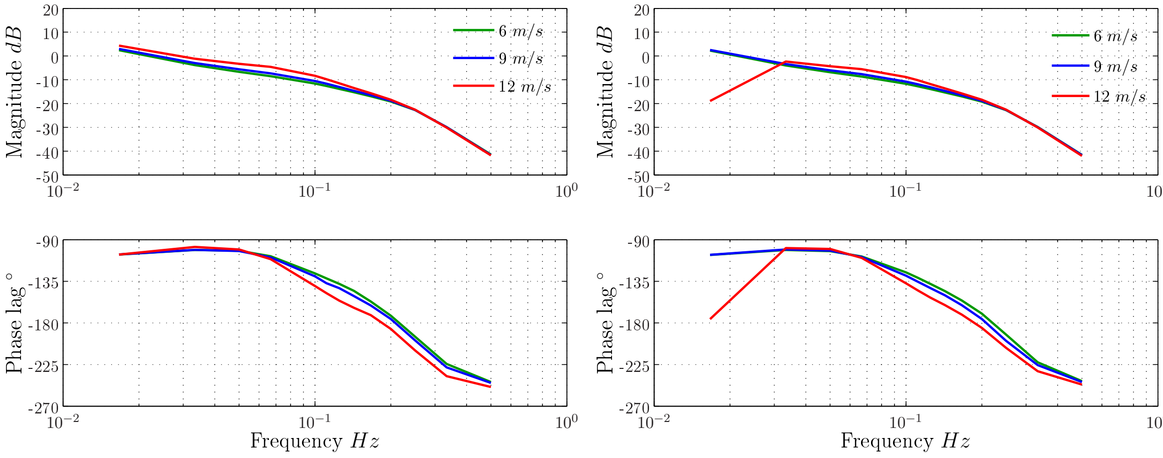

Amplitude $0.1 rad/s$ Amplitude $0.1 rad/s$

Figure 8.8: Rotor speed frequency response

wind speed, but it is not noticeably influenced by the amplitude of the input signal. Remember that 0.4 rad/s is quite a large oscillation in the rotor speed. The fall-off at the low frequencies for the response at 0.4 rad/s is beacuse the hydraulic relief vale started to operate at that point. This illustrates very well how even the most non-linear components play an important role in these kinds of analyses.

The frequency response here is presented as an example, and is carried out on an early version of the speed control system. A non-linear frequency response of one of the finished controllers are presented in section 10.4.

8.3.2 Pitch control frequency response

The method for finding the frequency response of the turbine through pitch control is almost similar to the speed control method. The difference is that while the speed controller is designed to govern the turbine speed, the pitch controller is designed to govern the turbine power (see section 9.1 for an overview of how the two controllers are supposed to act together). For this reason, the input signal to the controller is a sinusoidally varying power demand, and the output signal is the response of the turbine power to the input signal. This is illustrated in the block diagram of figure 8.9.

A frequency simulation was carried out on the pitch controller that is used in the control systems developed in section 10. The result is shown in figure 8.10 The frequency response simulations of the pitch controller turned out to be influenced by some kind of disturbance which caused problems for the developed peak-finding algorithm, although the response in it self was fine. This meant that quite a lot of manual manipulation was necessary to create a usable plot like the one in figure 8.10, and for that reason the non-linear frequency response tool was never utilized to tune the pitch control parameters. A more robust peak-finding algorithm is necessary in order to improve the performance of the non-linear frequency response tool.

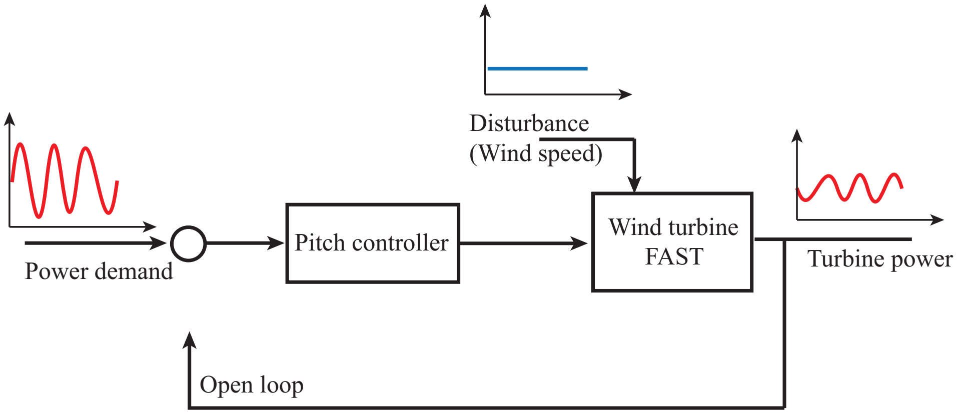
Disturbance
(Wind speed)
Power demand
Pitch controller
Wind turbine
FAST
Turbine power
Open loop

Figure 8.9: Turbine power frequency response block diagram

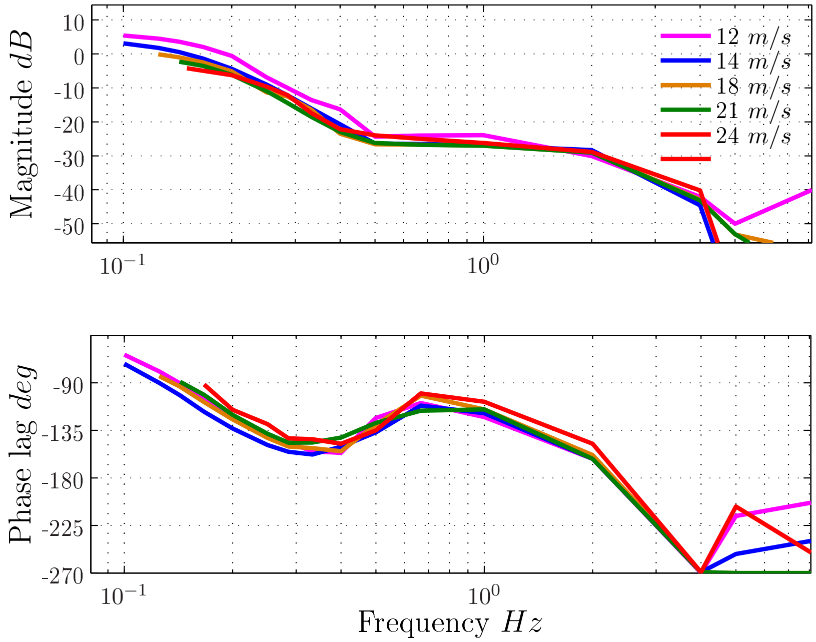

Figure 8.10: Response of the pitch controller

Chapter 9

Control objectives and definitions

The main motivations for controlling a wind turbine is to minimize the energy cost over the life span of the turbine. This includes means of maximising the energy capture efficiency, maximising the lifetime and minimizing the the cost of maintenance.

Control objectives for wind turbines are commonly divided into the following categories [7]:

- *Energy capture*
- *Mechanical loads*
- *Power quality*

Treatment of the power quality is not a central issue in this thesis and will only be treated briefly. The mechanical loads are treated in section 11 and the energy capture is treated in the following section.

9.1 Energy capture

The control objective with regards to energy capture can be summarized in a simple statement: The energy output should be as high as possible for every wind condition, without surpassing the rated energy limit. This is normally achieved by dividing the operational area into three zones as in figure 9.1.

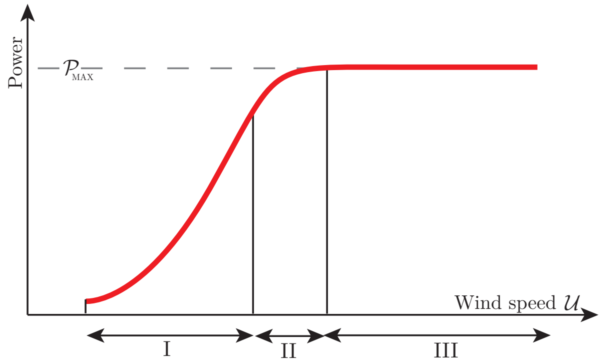

Figure 9.1: Ideal power curve

Zone I is the low-wind area above cut-in speed where the available power is lower than the rated power. This means that the turbine should be operated at the maximum efficiency point, i.e. at the optimal λ. Zone III is the high-wind area below cut-out speed where the available power is higher than than the rated speed. This means that surplus power must be limited by pitching of the blades. Zone II is known as the transition area. In this area λ has to be reduced to avoid turbine speed, torque or thrust forces above the maximum allowed limits. This area is also critical in variable speed pitch controlled turbines as both the pitch and the speed will be governed simultaneously and possibly have negative effect on each others performance [7].

The power, pitch and speed target for the wind turbine is shown in figure 9.2. The curves are based on BEM calculations.

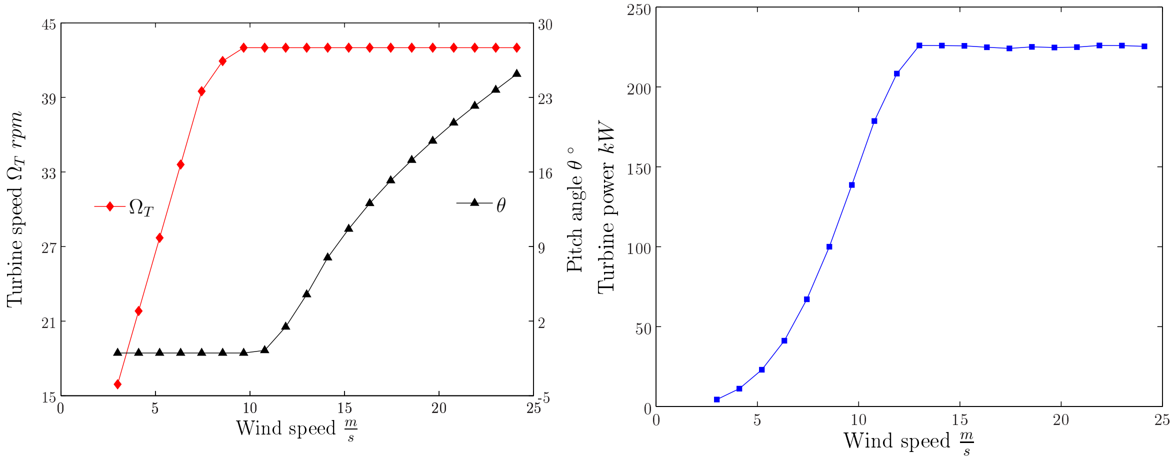

θ and Ω_T target

Power target

Figure 9.2: Turbine control target curves

9.1.1 Maximum power point tracking

The wind turbine of current interest is a variable pitch turbine that has been modified so it can operate at varying speed. For a variable-speed variable-pitch (VSVP) wind turbine, energy maximizing is carried out through maximum power point tracking (MPPT). MPPT means that the rotor is kept at the optimal tip speed ratio at below rated wind speeds. This is done by changing the rotor speed according to 9.1. The pitch angle is normally set at the optimal point, known as *fine*. The fine pitch angle is usually quite constant throughout the below-rated wind speeds, but some wind turbine manufacturers apply small changes of the pitch angle also in this area to reach the very peak of the efficiency curve.

$$\Omega_{T,\text{optimal}}(\mathcal{U}) = \frac{\lambda_{\text{optimal}}}{R}\mathcal{U} \tag{9.1}$$

Equation 9.1 shows that to be able to locate the maximum power point, one needs to know the wind speed. Wind turbines normally have an anemometer located at the top of the nacelle to measure the wind speed. This anemometer is down-wind of the rotor so that the measurements are disturbed by the heavy turbulence caused by the passing blades. For this reason, the wind speed measurements from the anemometer will not be as reliable as wanted [43].

Filtering methods for improved usability of anemometer measurements have been proposed [18], but a more common approach is to use some kind of wind speed estimation (WSE). The principle of WSE is to use equations 7.1 to 7.3 to calculate the wind speed from a known

$C_P(\lambda, \beta)$ distribution and a measurement of the shaft torque and rotational speed. The estimated wind speed can also be compared with the anemometer reading for verification.

9.1.2 Wind speed estimation

Figure 9.3 shows how the wind speed estimation is carried out: Along the turbine speed locus, the wind speed is uniquely known when the shaft torque and the rotor speed is known. The wind speed can also be estimated in the pitch controlled area, but this is not always necessary, as the pitch control could act on the measured power directly without going through a wind speed estimate.

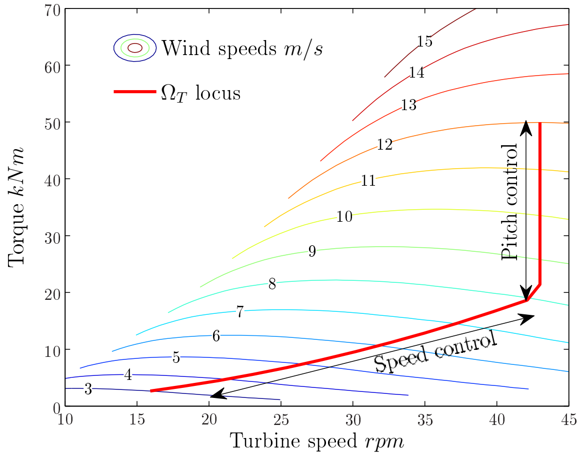

Figure 9.3: Principle of WSE

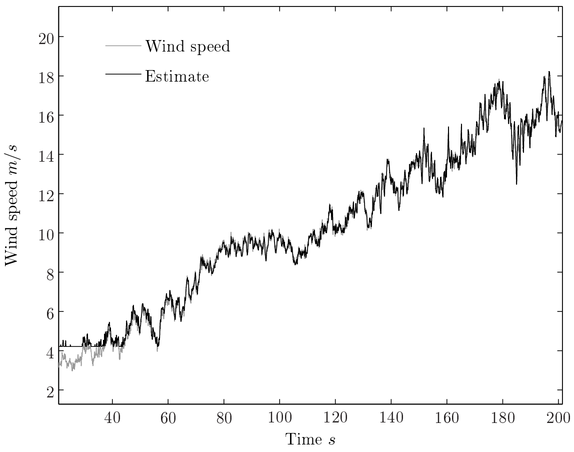

Figure 9.4: WSE performance

Figure 9.4 shows how the WSE performs at different wind speeds ranging from 4 to 18 m/s. The wind speed estimator performs very good for all wind speeds except below 5 m/s. How poor the low wind speed performance really is can clearly be seen in figure 9.6(a). The implications this has for the power production at low wind speeds was first underestimated,

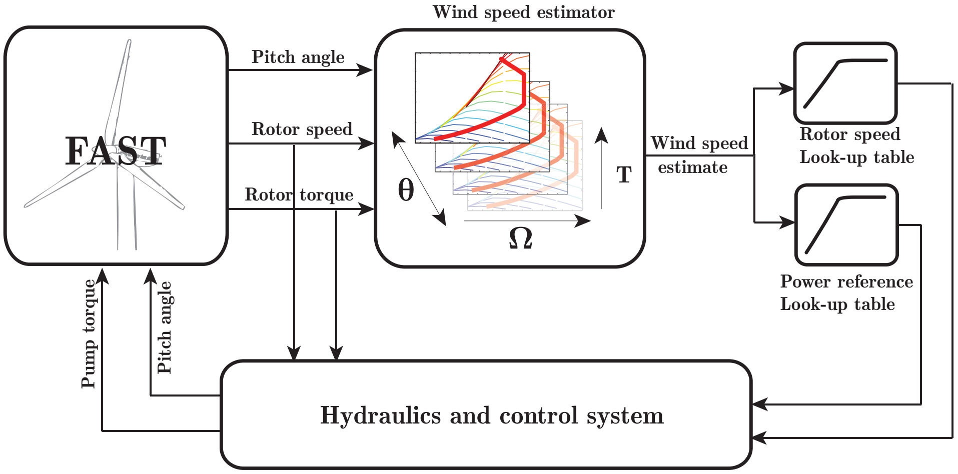

FAST
Pitch angle
Rotor speed
Rotor torque
Wind speed estimator
θ
Ω
T
Wind speed estimate
Rotor speed Look-up table
Power reference Look-up table
Pump torque
Pitch angle
Hydraulics and control system

Figure 9.5: WSE interaction with FAST and the control system

but the statistical analyses in section 11 show that the low wind speed performance is almost reduced to the level of the fixed speed turbine. This means that the wind speed estimator should be improved for low wind speeds, either by reworking the entire look-up table or by applying a correction. This problem was unfortunately discovered too late for this to be included in the thesis, but this is anyway an important task.

The output of the wind speed estimator is based on the turbine torque and speed, and the performance of the wind speed estimator is therefore highly dependent on how fast the turbine speed reacts to a change in wind speed. The plot in figure 9.4 was made with the model of the original V27 turbine, and this turbine reacts very fast to the changes in wind speed, first of all because of the stiff shaft. The response of the turbine with hydraulic drive train is, however, not as fast. Thus the WSE performance drops accordingly. This can be seen in figure 9.6(b). The performance of the WSE will automatically improve when the control system performance improves, as the two are closely related. It is imperative that the wind speed estimator performs well as it is central in both speed and pitch control of the wind turbine.

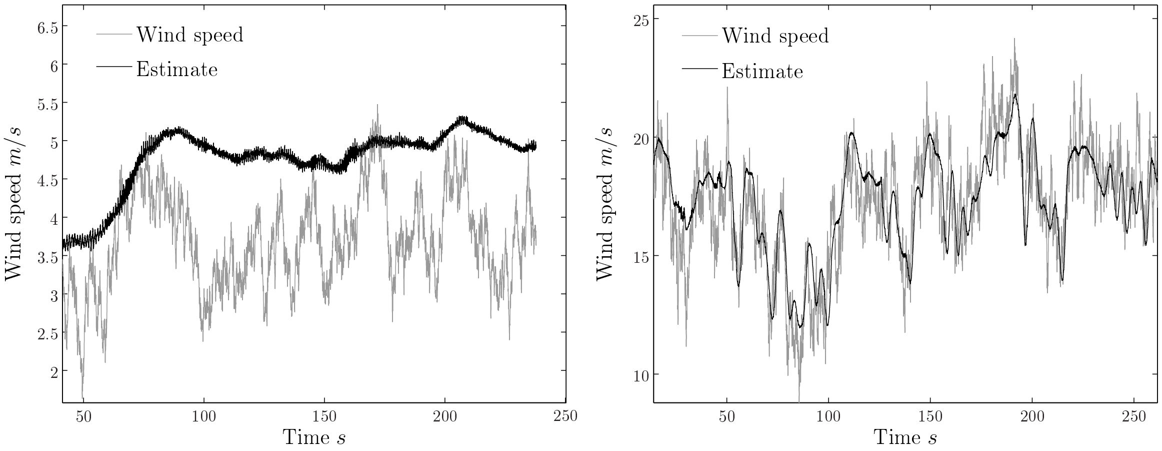

(a) Low speed performance (b) Hydraulic system performance

Figure 9.6: Challenges in wind speed estimator performance

Chapter 10

Control strategies

The control system for the modified Vestas V27 will be based on the two most common types of wind turbine control; pitch control and speed control. The pitch control system used in these simulations will be explained in section 10.1, and the speed control will be considered in section 10.2.

10.1 Base case: Original Vestas V27

A model of the original wind turbine has been created to serve as a basis of comparison. The original wind turbine is a fixed speed turbine with pitch control, hence the model will also be equipped with a model of the pitch control. The idea was to make a controller according to the documentation of the Vestas V27, so that the model behaviour would be as close to he real turbine as possible, but the documentation does not reveal enough of the governor structure to make an exact copy. Instead, the pitch controller will be reconstructed in accordance with the information that is provided.

The original pitch controller is a PID controller with a non-linear gain-scheduling approach for the pitch reference value. The controller is a limited derivative PID controller which is mathematically described by equation 10.1. The original controller is set up with the parameters listed in table 10.1

$$H_{\text{PID}} = K_p \frac{1+\mathcal{T}_i s}{\mathcal{T}_i s} \frac{1+\mathcal{T}_d s}{1+\alpha \mathcal{T}_d s} \tag{10.1}$$

Table 10.1: Vestas V27 prototype control parameters

		6 pole winding		8 pole winding	
Proportional gain	K_p	$-2 \cdot 10^{-6}$	–	$-11 \cdot 10^{-6}$	–
Derivative time	$\mathcal{T}_d$	0.1	s	0.1	s
Derivative cut-off	α	1	–	0.1	–
Integral time	$\mathcal{T}_i$	0.06	s	0.3	s

From the Vestas V27 electrical manual [47]

The α value shows that the derivative controller is deactivated for the main generator, and thus is reduced to a PI controller.

The gain scheduling of the pitch reference point is not fully described in the documentation, so an approximate approach has to be used: It is believed that some kind of wind speed estimation is used to set the reference pitch angle according to the generator power. But because the power is supposed to be constant for a wide range of wind speeds in the above rated wind regime the controller will not have any information above that point, and a correction has to be made to account for the apparently missing information in that area. Which method that is used in the original controller is not known, but one possible solution would be the wind speed estimator that is described in chapter 9.

The wind speed estimator will calculate an approximate pitch reference point and a power reference point. Then the first PI controller will act on difference between the power reference and the actual produced power as shown in figure 10.1. The first (or primary) PI(D) controller makes a correction to the pitch reference point from the wind speed estimator and a secondary PID controller then tries to follow the corrected reference by minimizing the error of the actual pitch angle as measured by the pitch sensor. There may be other feasible solutions of PI based pitch controllers, but this type is relatively simple and commonly in use. This type of controller is described in [3] and [32].

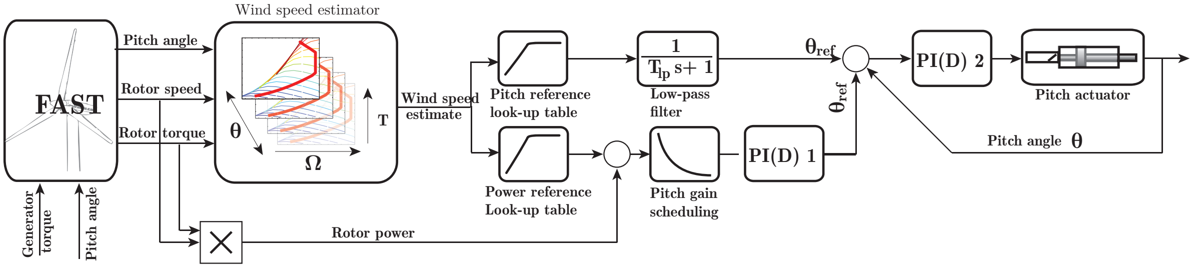

Figure 10.1: Pitch control layout

The gain scheduling of the pitch set point is due to the non-linear sensitivity of the produced power to the pitch error at different wind speeds. A 1°pitch error at low wind speeds will only yield a minor deviation in the power, whereas a 1°pitch error at 24 m/s yields a power deviation of almost 25 kW, which is 10% of the rated power. Consequently, for the PI controller to be effective across all wind speeds, the pitch reference point must be scheduled to account for the non-linearity. One way is to schedule according to the pitch angle, which is the method that has been implemented here. An analysis of the rate of change of turbine power with pitch angle has been carried out using the steady-state BEM model, and is displayed in figure 10.2. The gain scheduling means that the pitch controller must be less aggressive at high winds to provide stable power regulation. However, because of the choice of the pitch angle as the scheduling parameter, the approach relies on that the pitch angle is almost correct according to the wind speed. Large pitch errors due to for instance pitch oscillations may cause a too large or too small gain, which may further increase the oscillations.

The documentation of the control system also describes the valve characteristics of hydraulic servo valve that governs the pitch. The valve has a dead-band centre, and to increase the responsiveness of the valve, it also has a special servo controller that compensates for the dead-band. The two servo characteristics have been implemented in Simulink, and they are shown in figures 10.3 and 10.4

The control system in figure 10.1 was first constructed with the parameters from the electrical manual. But the controller response and was found to be unstable. This suggests that the controller has not been modelled correctly, or that the wind speed estimator is not the correct approach with the given parameters.

To improve controller performance, the gain was reduced slightly and a derivative term was introduced in both PI controllers (making them PID controllers)to improve the response time. After some trial and error, a set of reasonably good parameters were found. The Simulink

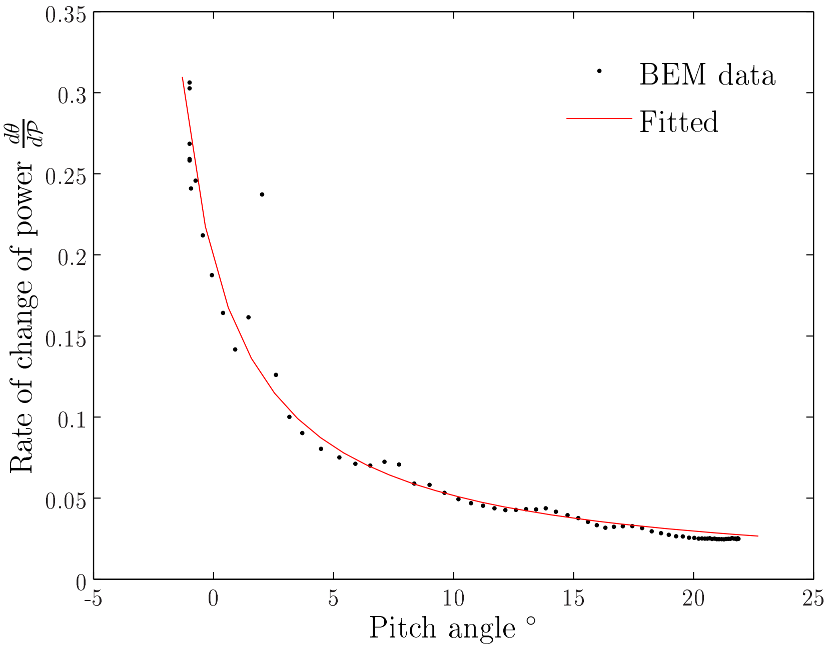

Figure 10.2: Pitch/power sensitivity to wind

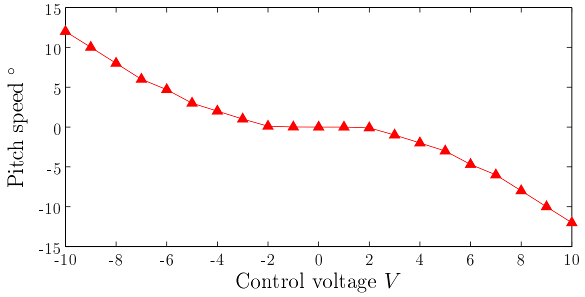

Figure 10.3: Servo valve characteristic

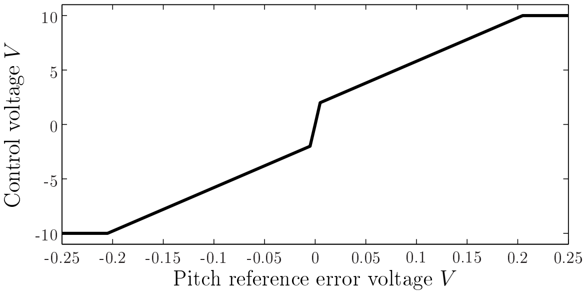

Figure 10.4: Servo controller

implementation can be found in appendix F, and the controller parameters are listed in table 10.2.

Because the final pitch controller is not similar to the controller installed in the turbine, the model of the original turbine looses some of its value as a basis of comparison for the hydraulic model. But still, the aeroelastic model of the original turbine with the developed controller will probably have quite similar dynamic response, so it will be used anyway. It was never the intention to analyse the original control system, but a better match would have been beneficial, as it could have been used for further verification of the aeroelastic model.

Note that the parameters of the primary and secondary controllers will be changed somewhat for the different control strategies that is developed later. The reason for this is that due to the low stiffness of the hydraulic circuit the controller must be tuned less aggressively in order to maintain stability.

Table 10.2: Vestas V27 model pitch control parameters

		Primary controller		Secondary controller	
Gain	K_P	-0.002	–	-0.8	–
Integral	$\mathcal{T}_i$	10	s	10	s
Derivative	$\mathcal{T}_d$	0.7	s	0.5	s
Derivative cut-off	α	0.5	–	0.2	–

10.1.1 Simulation results

To evaluate the performance of a control system, one common approach is to simulate the turbine response to a wind speed input of sequential 1 m/s wind steps from cut-in to cut-out [32]. This type of wind regime is very challenging for the controller, especially in the upper range of wind speeds. The resulting power, speed and pitch actions will then likely reveal any weaknesses of the control system. If the responses are too sluggish the power output will suffer, and if the responses are too quick, over-shooting will occur and possibly trigger instabilities. Of course, some overshooting is inevitable, especially at high wind speeds where the difference in aerodynamic power of a 1 m/s wind step is very large. Recall that the aerodynamic power is proportional to the wind speed to the power of three. A wind step from 23 to 24 m/s increases the aerodynamic power by 580 kW, more than twice the rated power. This increase has to be compensated for by pitching. But since the control system and the pitching mechanism is not instantaneous, large power overshooting in the rotor power will be a result. In this case, as the original V27 is a fixed pitch turbine, the speed is not of interest. Instead the wind speed estimator performance is plotted along with the pitch response and power response in figure 10.1.1. The simulation shows that the WSE and the control system is working very well. Both the pitch angle and the power curve follows the reference curves almost perfectly.

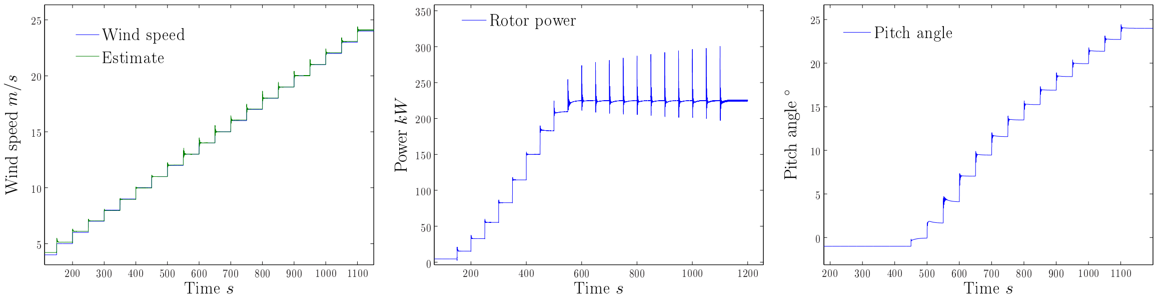

Figure 10.5: Step response of original V27 power and pitch

The turbine was also simulated in a 3D turbulent wind field to check the dynamic performance. The simulation results are presented in figures 10.6, 10.7 and 10.8. The results again show that the wind speed estimator is working very well. The pitch system is quite responsive, but not quick enough to avoid over loading of the turbine power. The simulations show that the developed control system for the V27 with the original drive train is sufficiently good to serve as a reference case for comparison of hydraulic and conventional drive trains.

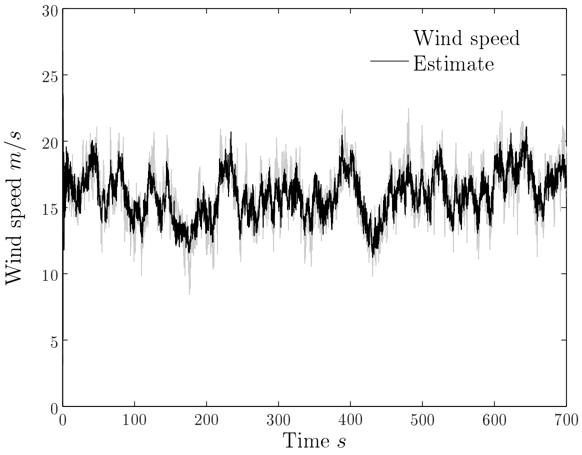

Figure 10.6: V27 turbulent wind

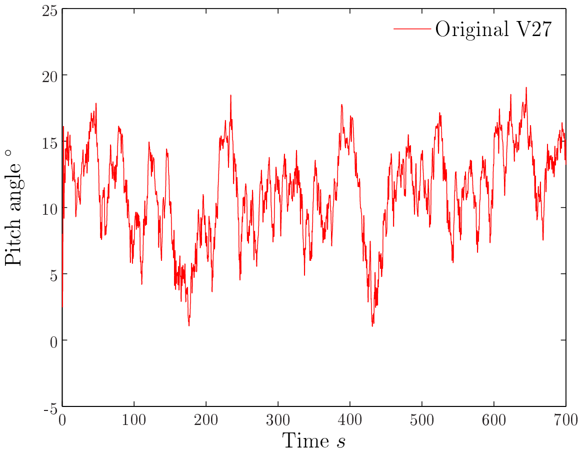

Figure 10.7: V27 turbulent pitch response

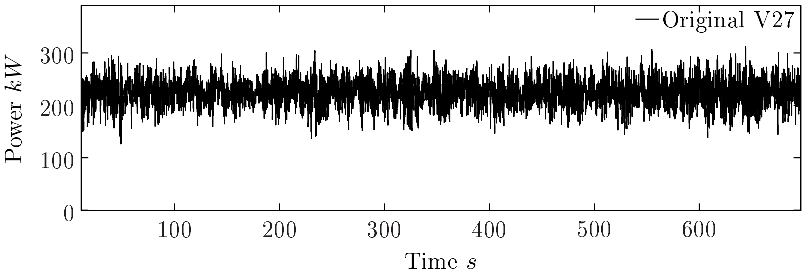

Figure 10.8: V27 turbulent rotor power

10.2 MPPT constant PID control

To utilize the advantages of the hydraulic circuit, the turbine should be run at variable rotor speed at below rated wind speeds, according to the concept of MPPT, as outlined in section 9.1.1. This is possible by governing the motor displacement volume according to the wind speed, to keep the turbine running at the optimal tip-speed-ratio.

The rotor speed reference point is set according to the wind speed, and the wind speed is estimated using the wind speed estimator discussed in section 9.1.2. The actual turbine speed is measured, and a PID controller then changes the motor displacement to counteract the deviation of the rotor speed from the reference point. The controller is outlined in figure 10.9.

With this speed control layout and the original pitch control system, the turbine was stable and fairly responsive at low wind speeds, but oscillations started to occur when the wind speeds rose to approximately 13 m/s. The step response in figure 10.2 shows the nature of the instabilities. According to Per Olav Haarberg from ChapDrive, the prototype had a lot of problems with oscillations when it was installed. These problems were solved by reducing the gains in the pitch controller. In the modelled system this did not help. After some unfruitful tinkering of the controller variables by trial and error, it was decided that a linear analysis should be carried out to see the problem from a different perspective.

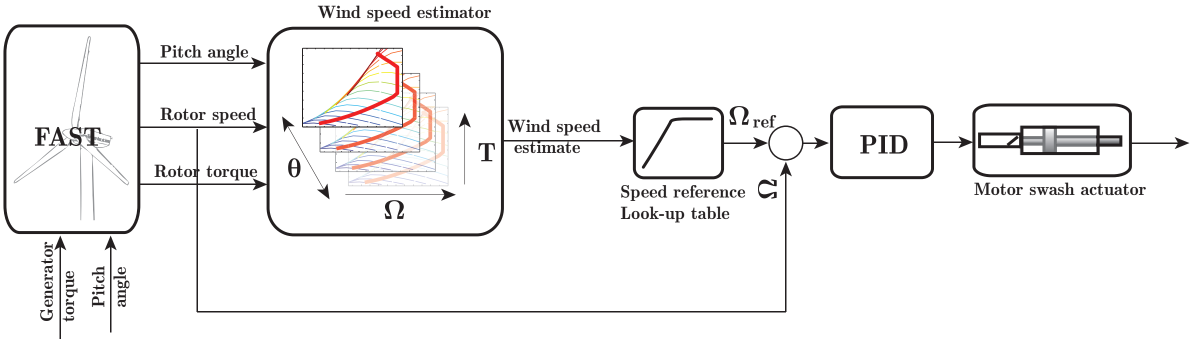

Figure 10.9: Speed control system outline

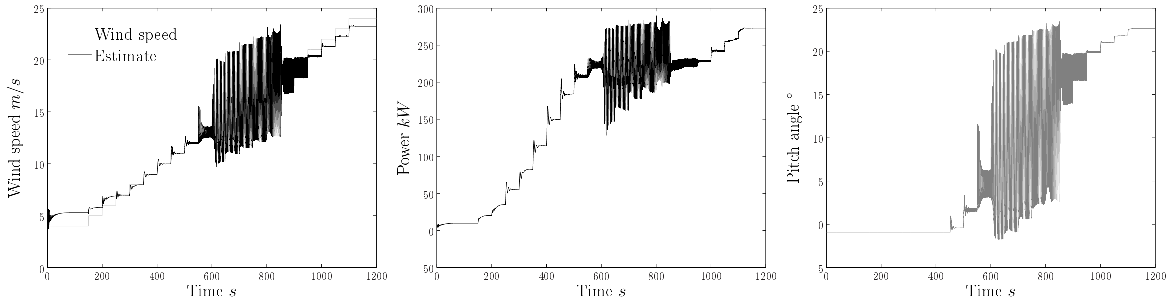

Figure 10.10: Step response of ChapDrive I model

10.2.1 Linear analysis

Although the system considered herein is highly non-linear, a linear analysis can still be a useful tool when determining the controller parameters. The main non-linearities in the system are the aerodynamic forces on the rotor and leakages from the hydraulic circuit, especially the boost and release valve flows. At low wind speeds, where pitch control is inactive and the oil pressure level is well below 350 *bar*, which is the pressure release valve set pressure, the hydraulic circuit could be regarded as linear around an operation point defined by the wind speed and the rotor speed.

In the project thesis, a linear analysis of a similar hydraulic system was carried out. The main difference is that the wind turbine that was analysed then was a stall controlled turbine. The same analysis has been carried out for the Vestas V27 with the hydraulic transmission. Only the results will be presented here, but the full theory and analysis is found in appendix A.

Figure 10.11 and 10.12 show the frequency response of the speed controller of the linearized wind turbine including aerodynamics and the hydraulic circuit. The frequency responses are calculated for the complete range of wind speeds according to the linear analysis in appendix A. The difference between the two figures is only the aerodynamics. Figure 10.11 shows the frequency response without pitching and figure 10.12 show the frequency response with ideal pitching according to the wind speed. The real situation will be something in between, as the pitch control is not perfect. Without pitching is the turbine unconditionally unstable for high wind speeds, but pitching stabilizes it. If one could rely on an ideal pitch control, no further action would be necessary, but as simulations have shown that the pitch control can become very oscillating and thus cause the speed control to become unstable. Also note the dominant

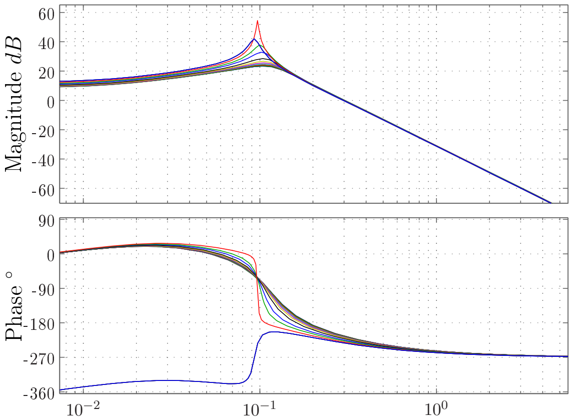

Figure 10.11: APF: No pitch control

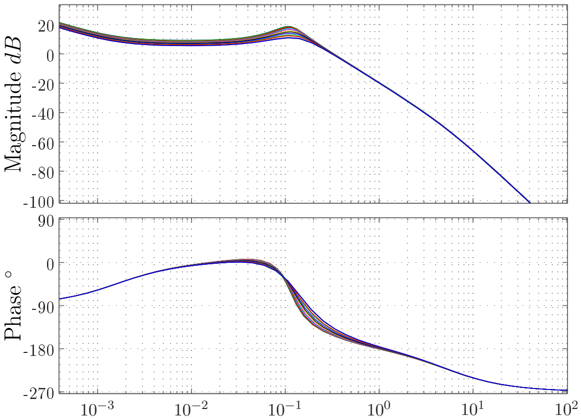

Figure 10.12: APF: Ideal pitch control

frequency at 10^{-1} Hz in both APF diagrams. This is the resonant frequency of the drive train due to the speed control action, and it can be seen in the aeroelastic simulations. See e.g figure 8.2.

A well known method from the discipline of fluid power control to dampen out oscillations in rotary machinery is to use damping injection from the high pressure side. This approach was used with success in the project thesis [16], and it has been tested with promising results in the prototype. The principle of the pressure injection damping is explained in appendix A

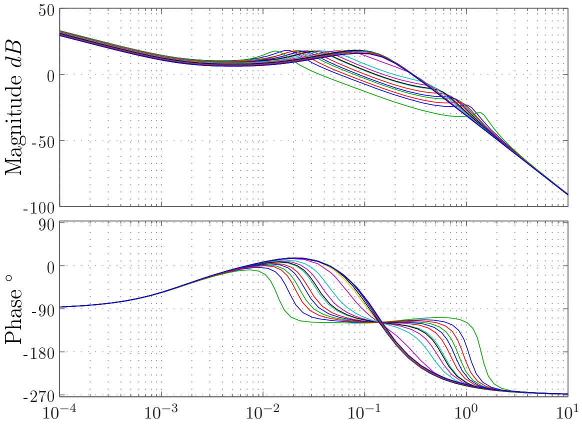

Figure 10.13: Pressure feedback, constant gain

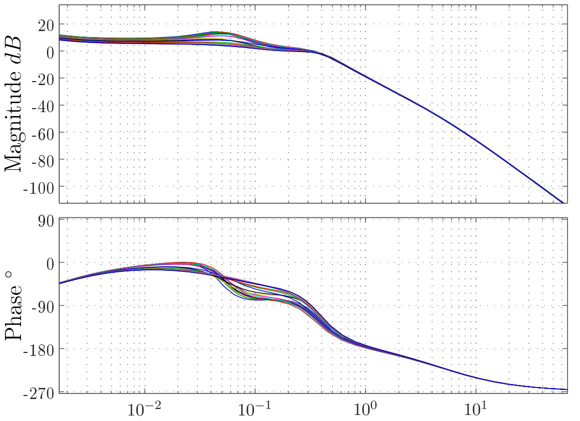

Figure 10.14: Scheduled gain

Figure 10.13 shows the frequency response of the speed controller with a pressure feedback injection from the high pressure side. The turbine is no longer unconditionally unstable, but the turbine response has varying characteristics for different wind speeds and an oddly looking shape. Varying characteristics are more challenging for the controller, and should be avoided as much as possible. In figure 10.14 the pressure feedback gain has been scheduled according to wind speed, and the results are much more uniform characteristics. Also note that the dominant peak at 10^{-1} Hz is now smeared out over a broad frequency range.

This linear analysis indicates that pressure injection is a stabilizing factor. It also suggest a possible explanation for the oscillations that was mentioned earlier (see figure 10.2). The resonant peak in figure 10.11 clearly shows that low frequency oscillations can occur if the pitch angle is not correct.

10.2.2 Controller implementation

Already before this linear analysis was carried out, a pressure injection path was added to the control system in Simulink, but it was not very fruitful with regards to the oscillations. A lot of different measures was taken to try to stabilise the system, including among others:

- Pressure feedback in the pitch system, similar to the pressure injection in the speed controller. This did not have any stabilizing effect.
- Coupling of the pitch actuator cylinders to a relief valve on the high pressure side directly so that the pitch was self controlling when the pressure rose above a specified level. This worked quite well, but the pitch response was too slow to limit the turbine power at high wind speeds so this approach was rejected. It could still be utilized as a safety feature to pitch back the blades if the other system should fail. Such an implementation could save a turbine from runaway and destruction. This concept is further analysed in section 10.6.

None of these approaches were successful, and neither was scheduling of the pressure injection gain. In fact the calculated pressure injection gains were too large, and triggered instability even at low wind speeds. The conclusion drawn from this is that the system may be too nonlinear in its behaviour for the linear analysis tools to provide assured stability. The output from the gain scheduled pressure feedback loop revealed a very peaky signal in turbulent wind. To avoid instabilities, the gain had to be reduced so that the feedback loop lost almost all effect for all but the highest wind speeds. Because of this, the gain scheduling on the pressure injection will not be used, but it might be worth a closer look at a later point. A pressure feedback loop with a constant gain is chosen instead, based on the experience from ChapDrive and advice from prof. Peter Chapple.

By systematically changing the parameters of the control system, the source of the instabilities was located to the wind speed estimator. Even though the wind speed estimator works flawlessly for the conventional drive train, the same was not the case with the hydraulic drive train. Recall that the wind speed estimator calculates the wind speed based on the rotor torque and speed and the pitch angle. This estimated wind speed is then used to calculate both the speed, power and torque reference. This means that a feed-forward loop from the response is used to set the reference of the feedback loops. The result is that when oscillations occur in either the speed or the pitch system, instead of being damped out, the oscillations are fed back into the wind speed estimator and is propagated from there to the other control loop.

The solution is to use heavy low-pass filtering on one of the control loops so that they are brought sufficiently out of phase to avoid self-excitation. Filtering any of the three references would work, but such filtering causes very sluggish responses of that control loop. The speed loop is necessary at low wind speeds to maximize the energy production, and the power feedback is necessary at high wind speeds to reduce over-loading of the turbine. Thus the natural choice was to filter the pitch reference. A filtering time constants $\mathcal{T}_{lp}$ of 10 seconds was found to be necessary. Larger values also provided stability, but the pitch response became more sluggish. The explanation for this relatively large value is that filter must be able to reduce the resonant frequency that appears due to the interaction of the speed control system with hydraulic circuit. This resonant frequency has been found both through linear analysis and in the aeroelastic simulations to be approximately 10 seconds. The need of using filtering to avoid instabilities has also been reported for simulations of PI-controlled pitchable wind turbines with conventional drive trains [22]. In that case, the drive train frequency was constant, and thus a narrow band-stop filter was sufficient. Here the drive train frequencies appear in a relatively broad band due to the effects discussed in section 8.1. For this reason, a low pass filter that would eliminate the entire band of possibly resonant frequencies was chosen. It should be noted that the inclusion of the filter is not based on application of control theory, but it is rather an ad-hoc solution to the experienced instability problem.

Another possible solution would be to remove the feed-forwarding of the pitch reference to the secondary pitch controller. Feed-forwarding the pitch reference to the pitch controller should in theory not be necessary, as the pitch controller could act solely on the power deviation. However, the pitch-power control needs an integral term to avoid steady-state errors, and without the feed-forwarding, the integrator would suffer severe wind-up at low wind speeds where the pitch angle is held constant at -1°. This issue can be resolved by applying anti-wind up techniques[1]. However, the response using this approach was found inferior to a filtered feed-forward of the pitch reference.

The resulting PID speed controller block diagram is shown in figure 10.15, with the parameters listed in table 10.3. The sequential step response is shown in figure 10.2.2.

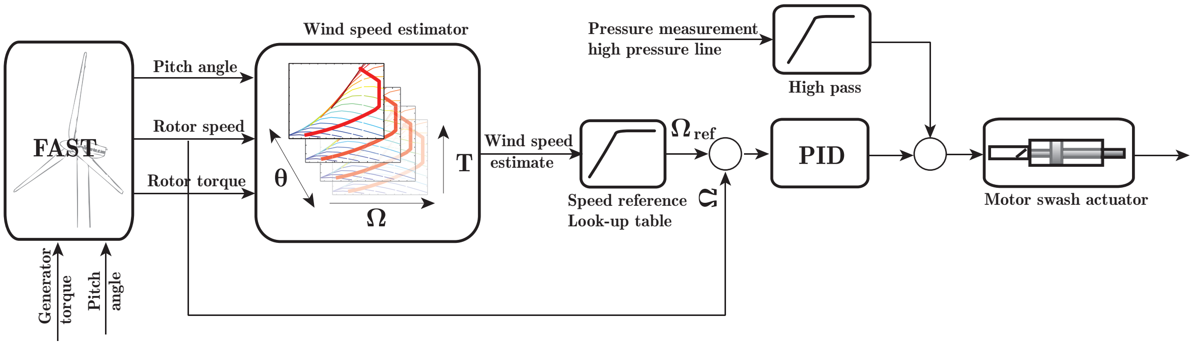
FAST
Pitch angle
Rotor speed
Rotor torque
Wind speed estimator
θ
Ω
T
Wind speed estimate
Speed reference
Look-up table
Pressure measurement
high pressure line
High pass
Ω ref
Ω
PID
Motor swash actuator
Generator torque
Pitch angle

Figure 10.15: Speed control feedback loop block with damping injection

Table 10.3: ChapDrive 1 modelled control parameters

		Speed controller		Pitch controller	
Gain	K_P	$6 \cdot 10^{-6}$	–	0.8	–
Integral	$\mathcal{T}_i$	200	s	20	s
Derivative	$\mathcal{T}_d$	3	s	0.7	s
Derivative cut-off	α	0.2	–	0.2	–
Pressure injection gain	K_T	10^{-12}	–	–	–
Pressure injection high-pass	$\mathcal{T}_f$	0.5	s	–	–

The parameters of the secondary pitch controller are the same as in table 10.4

---

[1] An explanation of the phenomenon and a number of different anti wind-up techniques can be found in reference [48]

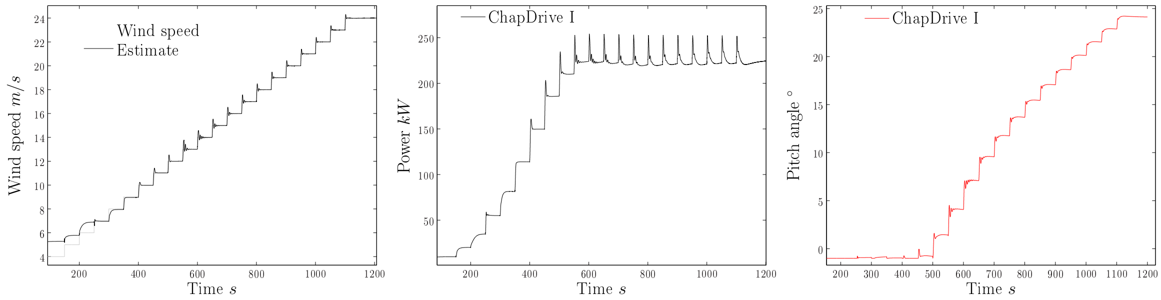

Figure 10.16: Step response of ChapDrive I model

10.3 Gear box substitute

The first approach to running the prototype of the ChapDrive I wind turbine with a hydraulic drive train was to use it as a gearbox substitute. As the name implies, the idea of this approach is to let the turbine run as the original turbine with the same pitch controller as modelled for the original turbine configuration. The only difference is that the hydraulic transmission that has been described earlier is used instead of the gearbox. This is done by having a fixed motor displacement, so that the ratio between the pump displacement and the motor displacement equals the gearbox ratio. This control strategy lacks the advantage of the hydraulic transmission, which is the stepless gear ratio, but it incorporates the main disadvantage, which is the relatively higher losses. Due to this, the approach does not have any practical application, but it is interesting in that it is directly comparable with the original. The difference in dynamic behaviour reveals the large impact the low stiffness has on stability and performance.

To ensure stability, the pitch controller had to be tuned even less aggressively than for the MPPT model. And while this improves stability, it also reduces the pitch responsiveness and the ability to quickly reduce the power at high wind speeds. The controller parameters are listed in table 10.4.

Table 10.4: ChapDrive 1 gearbox substitute model pitch control parameters

		Primary controller		Secondary controller	
Gain	K_P	-0.001	$-$	-0.4	$-$
Integral	$\mathcal{T}_i$	20	s	10	s
Derivative	$\mathcal{T}_d$	0.7	s	0.5	s
Derivative cut-off	α	0.2	$-$	0.2	$-$

The system was simulated for a number of wind speeds with varying results with regarding stability and performance. The results are summarized below:

- At low wind speeds the turbine is simulated with the secondary generator. The turbine is stable and operating at an almost fixed rotor speed of 33 rpm, as the original turbine would do with the secondary generator windings. The rotational speed is therefore not optimal, but the aerodynamic performance should match the original turbine well. With the extra losses of the hydraulic circuit, the produced power is of course lower than the original turbine. On the other hand, the turbine speed oscillations are small and of low frequency, which should give little fatigue damage.

- At high wind speeds the turbine is simulated with the primary generator. The turbine is stable, but the speed oscillations are quite noticeable. Due to the increased leakage flow associated with the higher oil pressures, the motor is not capable of limiting the turbine speed. The pitch control limits the power as one would expect, but because the turbine is constantly running at above rated speed this turbine configuration is not suitable for high wind speeds.

Results from the low wind speed simulation is found in figure 10.17.

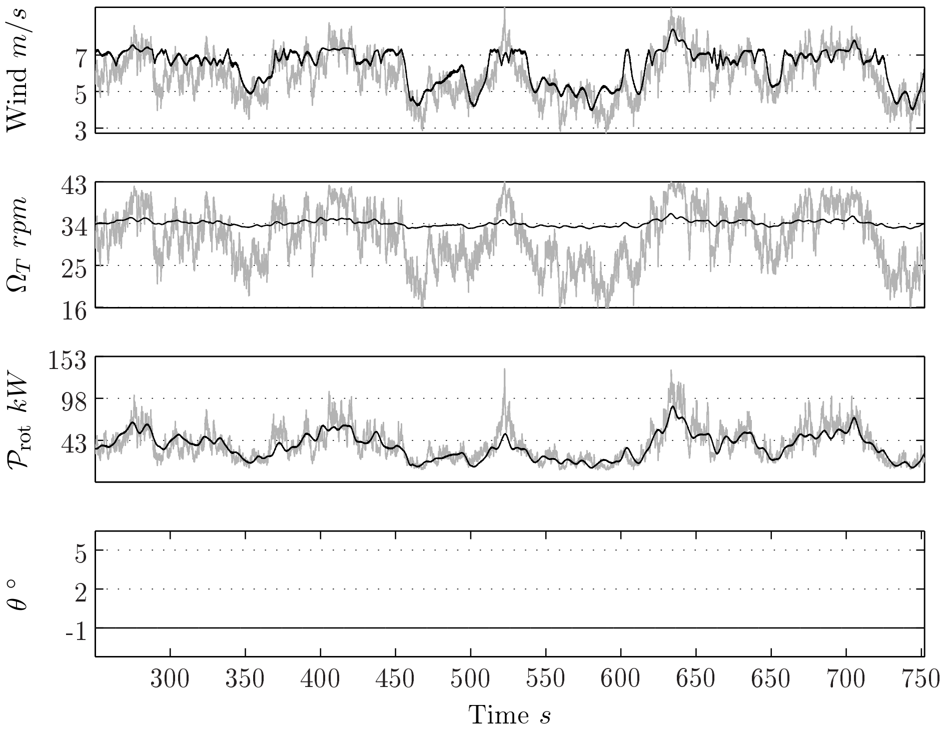

Wind speed plot: Grey line actual wind. Black line wind speed estimate
Other plots: Grey lines optimal performance. Black lines actual performance

Figure 10.17: Gearbox substitute performance - low wind speed

10.3.1 Improved gearbox substitute

In order to develop a gearbox substitute that can be used in comparison with the other control strategies, an improved model was created that compensated for the extra leakage. The pitch controller implemented is the same as in table 10.4. The fixed motor displacement was chosen to be 410 cm^3/rev which is 82% of maximum displacement.

With this setting the fixed displacement controller was able to limit the rotor speed even at the highest wind speeds. The step response of the improved gearbox substitute model shows that it is stable and well-behaving even at the highest winds. The step response is shown in figure 10.3.1.

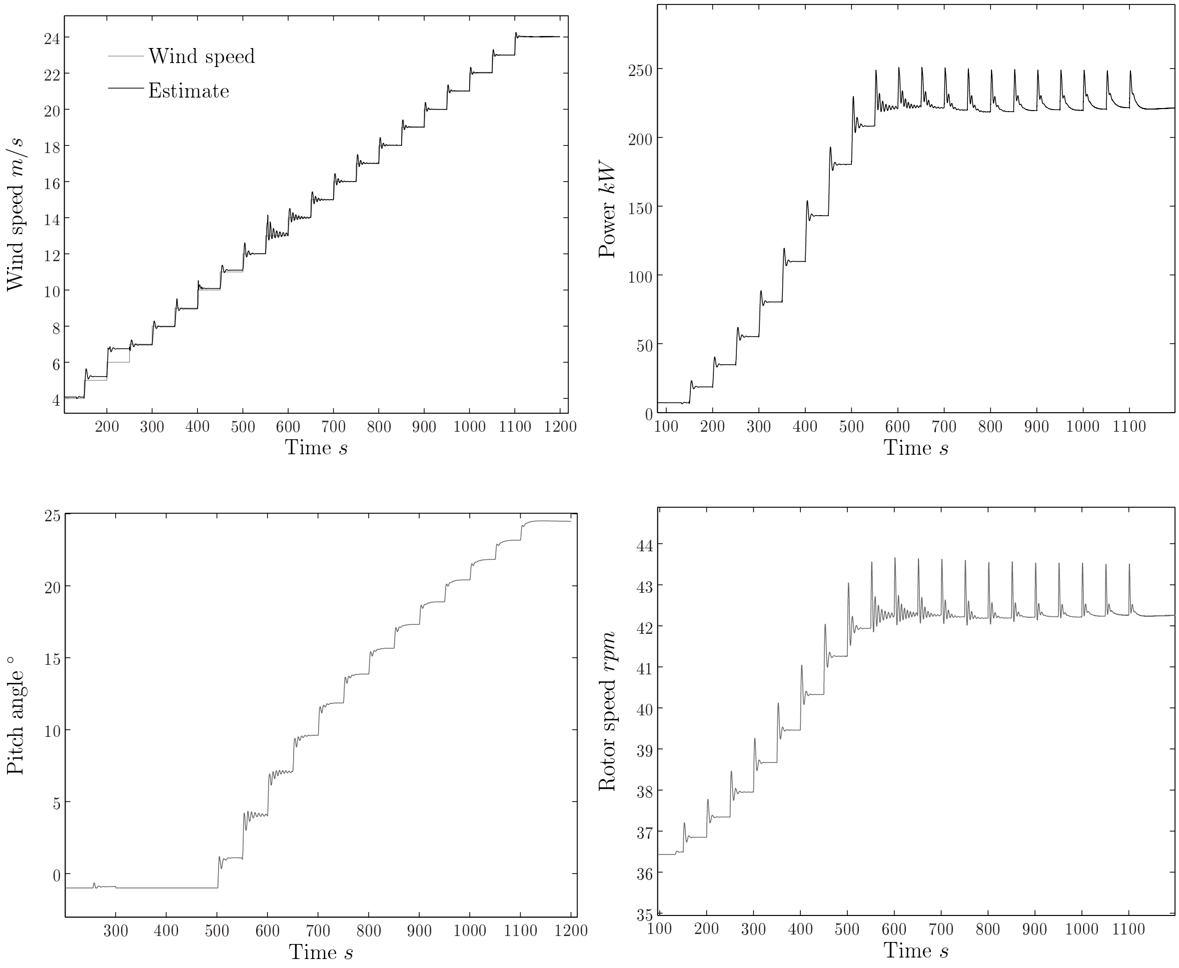

Figure 10.18: Step response of ChapDrive I improved gearbox substitute model

10.4 MPPT Gain scheduling PID control

In the project thesis [16], it was shown that gain scheduling of the speed controller could improve the controller response at low wind speeds while maintaining stability at high wind speeds. However, in the project thesis a stall controlled turbine was investigated, and because of the negative aerodynamic damping associated with this type of turbines, large corrections on the gains were necessary. In a pitch controlled turbine, the necessary changes does not need to be so dramatic, as the turbine response is more similar throughout the wind speed range. But some improvement could still be possible.

The gain scheduling controller block diagram is illustrated in figure 10.19.

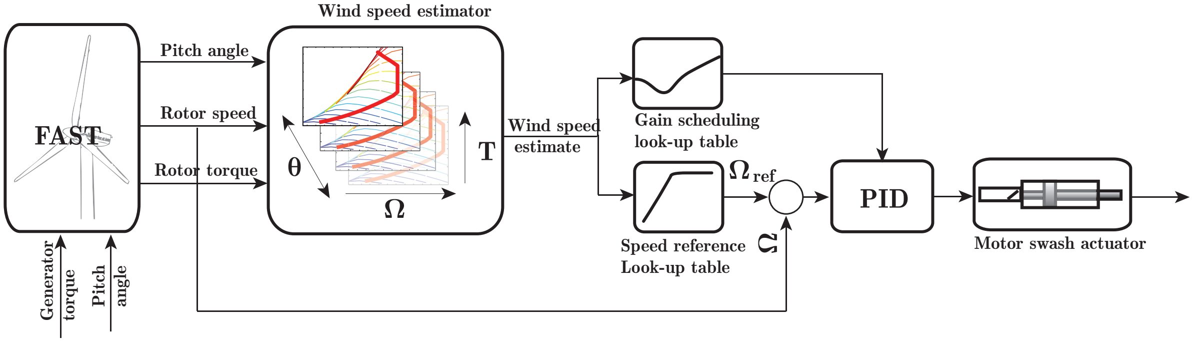
Wind speed estimator
Pitch angle
Rotor speed
Rotor torque
FAST
θ
Ω
T
Wind speed estimate
Gain scheduling look-up table
Ω_{ref}
PID
Motor swash actuator
Speed reference Look-up table
Ω
Generator torque
Pitch angle

Figure 10.19: Speed control feedback loop gain scheduling

10.4.1 First attempt

A first attempt on scheduling the control system was carried out by utilizing the time-domain frequency response tools that were discussed in section 8.3. The frequency response plots of of the MPPT speed controller is shown in figure 10.4.1. The amplitude of the sinusoidal signals used to create these responses was $\Delta\Omega_T = 0.1\ rad/s$. It was shown earlier that the rotor speed frequency response was almost independent of the amplitude.

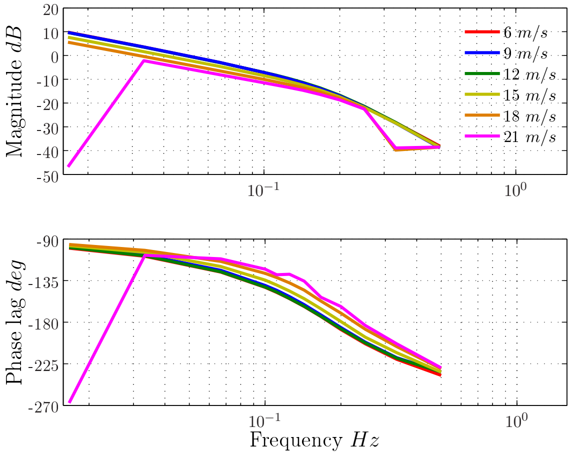

Figure 10.20: Ω_T frequency response

The similarities with the frequency response plots from the linear analysis are not striking, but the corner frequency at 0.1 Hz can be found in the diagrams from both analyses. However, the resonant peak at that frequency, which was very evident in the linear analysis plots, is non-existent in this non-linear analysis. The reason for this might be that a finite number of frequencies has been tested, whereas the linear analysis tests for all frequencies. The lack of an evident peak might be because the exact right frequency has not been tested. The other possible explanation is that the peak is damped out, due to the non-linearities in the system. The last explanation is the most likely, as a resonant peak as evident as in the linear analysis probably would be more dominant in the PSD plots in section 8.

The phase- and gain margins from figure 10.4.1 is well above what is the recommended minimum in linear control theory literature[2]. Common rule-of-thumb values are that the phase margin $\psi > 45°$ and the gain margin $K_P > 6\ dB$. By applying a gain scheduling scheme, so that all the gain margins are reduced to 6 dB, the controller performance should in theory improve as long as the ψ is kept above the recommended value. In this case, it means that a gain scheduling in figure 10.21 can be added to the existing gain.

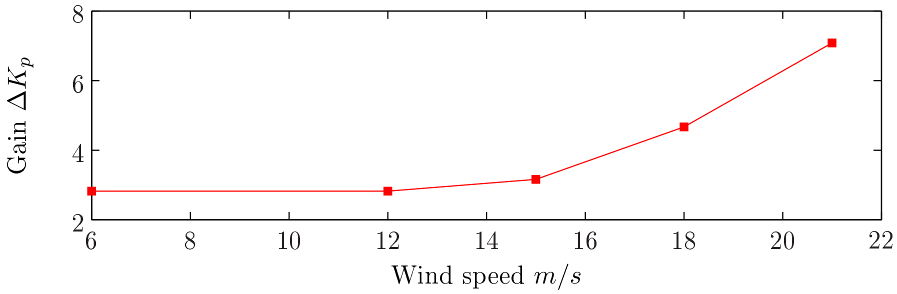

Figure 10.21: Non-linear analysis gain scheduling scheme

With this gain scheduling scheme, the step response is shown in figure 10.4.1. The figure

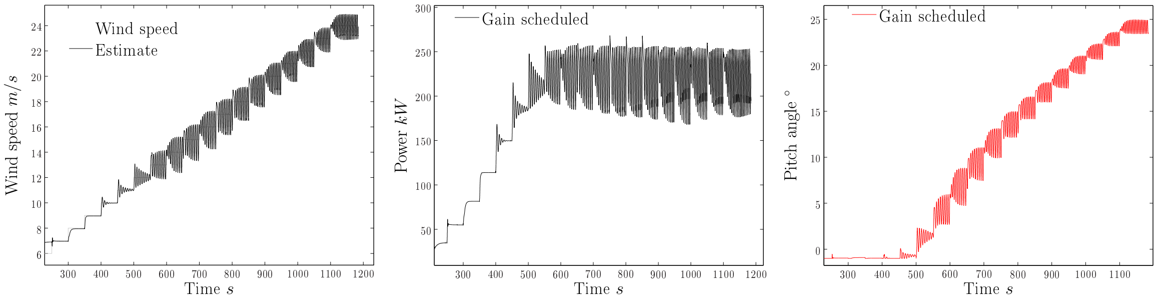

Figure 10.22: Step response of ChapDrive I gain scheduling. Approach 1

shows that the gain scheduling causes early instabilities to occur. Even when the constant gain increase was lowered, so that the system became stable, the trend of increasing the gain towards higher wind speeds seemed to cause more oscillations. consequently, this attempt was not further investigated.

---

[2] See appendix A for more information on these parameters and the use of frequency response diagrams in linear control theory

10.4.2 Second attempt

A second attempt of improving the controller performance through gain scheduling was attempted. Instead of using any of the frequency response as basis, the plot of the wind speed estimator performance is used as a basis. The occurrences of oscillations occur around 10 m/s. Until that point a relatively large gain should be possible, but then the gain has to be reduced until approximately 15 m/s. From that point on the gain can again be increased. By visual inspection of the graphs in figure 10.3.1 the gain scheduling scheme of figure 10.23 was created.

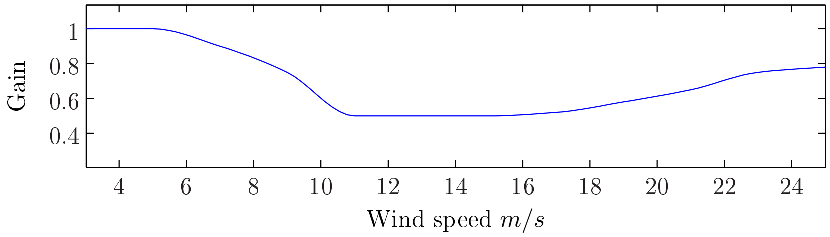

Figure 10.23: Visual analysis gain scheduling scheme

This scheme turned out to have a much nicer response to the sequential wind steps than the other gain scheduling scheme, as is shown in figure 10.4.2. This controller is much more aggressive at low wind speeds, and to check what effect that has on energy production and fatigue damage, this model will be part of the comparison in chapter 11. The control scheme does not claim to be optimal in any way, and it could probably be tuned further for better performance. But as the scheme is developed based on visual impressions, this will have to be based on trial and error, and this has not been done here. The idea is merely to see if gain scheduling can have a positive effect. The remaining control parameters are listed in table 10.5, and the parameters are listed in table 10.3.

Table 10.5: ChapDrive 1 modelled control parameters

		Speed controller		Pitch controller	
Gain	K_P	1.5	–	0.8	–
Integral	$\mathcal{T}_i$	200	s	20	s
Derivative	$\mathcal{T}_d$	3	s	0.7	s
Derivative cut-off	α	0.2	–	0.2	–
Pressure injection gain	K_T	10^{-12}	–	–	–
Pressure injection high-pass	$\mathcal{T}_f$	0.5	s	–	–

The parameters of the secondary pitch controller are the same as in table 10.4

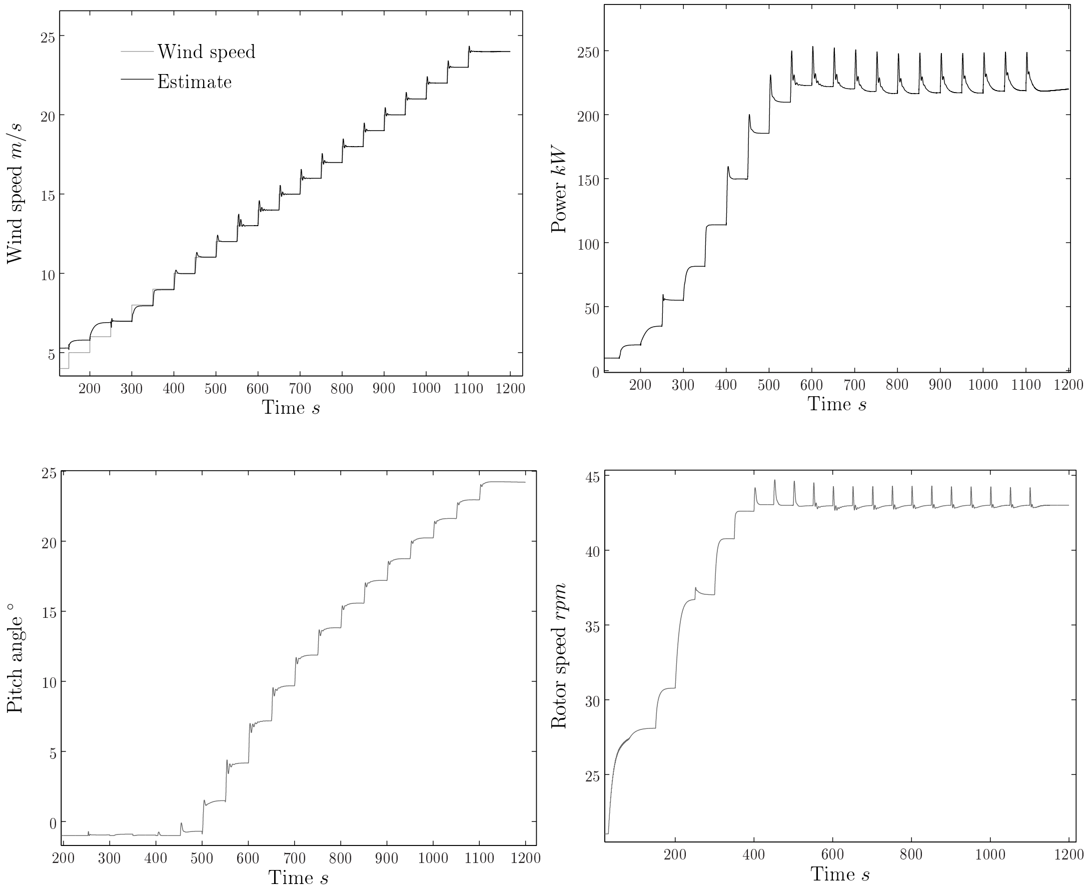

Figure 10.24: Step response of ChapDrive I gain scheduling. Approach 2

10.5 Reduced power point tracking (RPPT)

The principle of reduced power point tracking (RPPT) is closely related to maximum power point tracking, only the aim is not to follow $C_{P\max}$, but rather 0.99 $C_{P\max}$ or 0.98 $C_{P\max}$. Pursuing a less than optimal power curve may seem a little odd, but the reason why this could be beneficial has to do with stability issues: Figure 10.26 shows a typical C_P-C_Q relation with λ. When operating at $C_{P\max}$, the turbine is on a stable operating point on the C_Q-curve, i.e. the slope of C_Q is negative. This means that when the turbine speed increases, the aerodynamic torque decreases. However, if there was a sudden increase in the wind speed due to a gust, λ would decrease according to equation 7.3. If the gust was sufficiently strong, the turbine might end up on the left side of the C_Q-peak. This is an unstable operating point, where an increase in turbine speed would cause an increase in aerodynamic torque. Frequent translations across the C_Q-peak would cause more oscillations in the turbine rotational speed and, consequently, less produced power due to effects like dynamic stall.

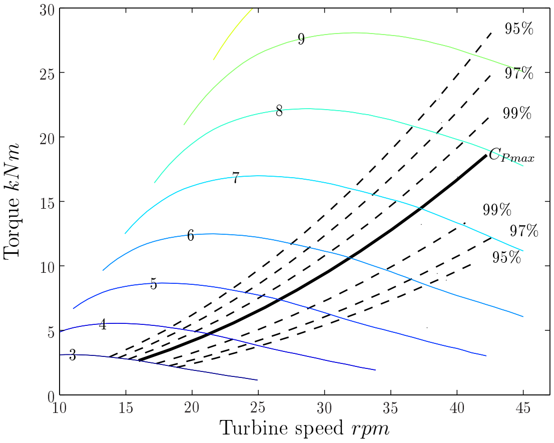

Figure 10.25: Reduced C_P target curves

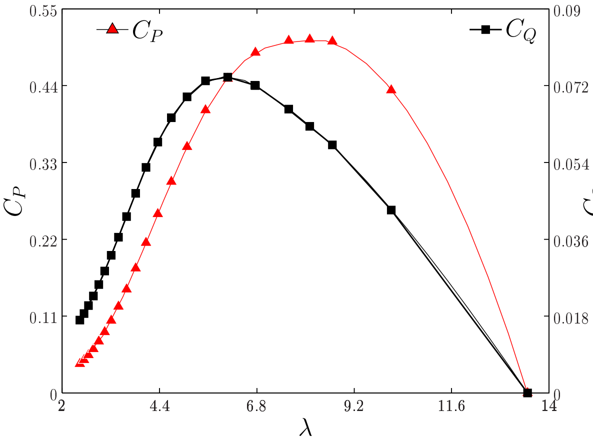

Figure 10.26: Power and torque coefficients

The amplitude of the wind gust needed to create unstable behaviour is seen in figure 10.25, where the $C_{P\max}$ and some reduced C_P locus curves are plotted. The dashed curves above the $C_{P\max}$-curve are to the left of the $C_{P\max}$ point in figure 10.26, and the curves below are to the right. To show the difference between the two sides, the 95% curves will be used as an example: If the turbine was running at 4 m/s wind and at the 95% point left of the $C_{P\max}$ point, a wind gust reaching 6 m/s would be sufficient to cross the C_Q-peak. If the turbine was running at 4 m/s wind and at the 95% point to the rigth of the $C_{P\max}$ point, a wind gust twice as powerful, reaching 8 m/s, would be necessary to produce the same result. Of course, when comparing for instance the 99% curves, the difference would not be that dramatic, but som improved stability could be gained with virtually no loss.

The RPPT principle could also have another useful feature, especially when considering a hydraulic transmission: If the stability was not an issue, for instance for a low turbulence site, or with a very good control system, the turbine could be run at a reduced power point to the left of $C_{P\max}$ giving a lower turbine speed with higher aerodynamic torque. This would yield a minor loss in aerodynamic efficiency, while the efficiency of the hydraulic circuit could improve considerably, because the pump and motor efficiencies are highly dependent on the system pressure, which in turn is dependent on the rotor torque. An optimal reduced power point can be found by optimizing in accordance with the pump and motor power curves. Due to time constraints, this will not be pursued further. Instead, to test the phenomenon, both 95% reduced power points will be tested to see if there is any significant differences. In figure 10.29, a time simulation of the two reduced power points at 4 m/s average wind speed is shown. The grey line is below the optimal speed locus, and the black line is above. The difference in pressure and turbine speed can easily be seen, as one would expect, but the figure also shows that the power production is slightly higher for the lowest rotor speed, as predicted. What this implies in terms of stability and overall power production is further analysed in chaper 11.

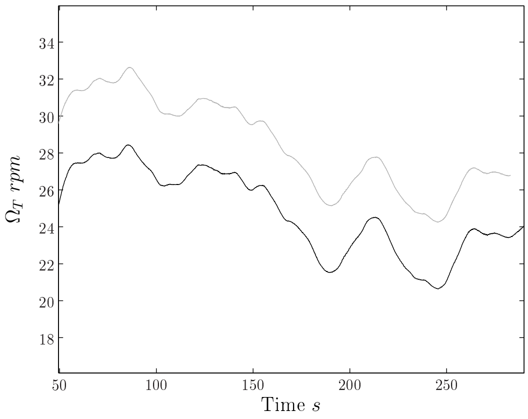

Figure 10.27: RPPT turbine speed

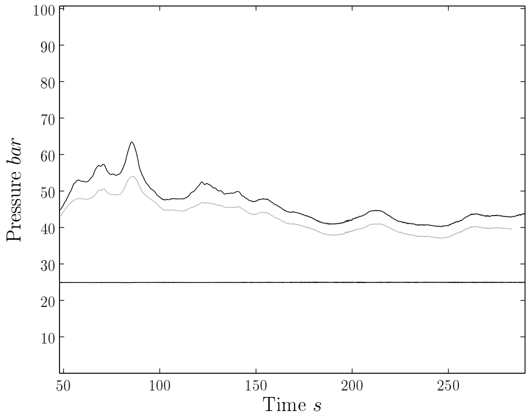

Figure 10.28: RPPT hydraulic pressure

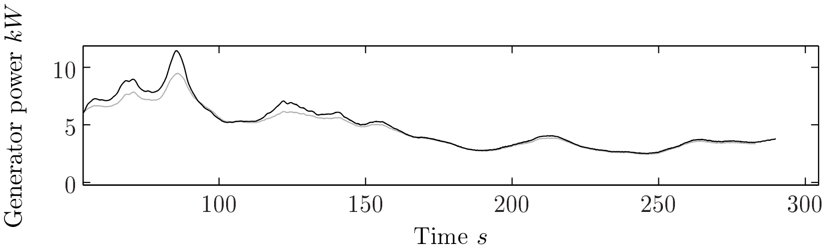

Figure 10.29: RPPT generator power comparison

10.6 Self governed turbine

The final control strategy that will be examined is a self governing turbine. It incorporates the improved gearbox solution from section 10.3.1. In addition it will use a pitch control system that parasites on the high pressure line to feed the hydraulic actuator. The principle is outlined in figure 10.30.

This control system is not meant as a challenger to the conventional control systems at the point, but the idea could be used as a security feature to feather the blades if the hydraulic pressure should become too high. In that case, a spring return would probably not be beneficial, but rather an electromagnetic return. Such an arrangement would ensure that the blades be feathered if turbine should suffer loss of electricity, or an error would occur in the hydraulic circuit.

The slide valve is modelled by a mass-spring-damper system. The working area of the pilot

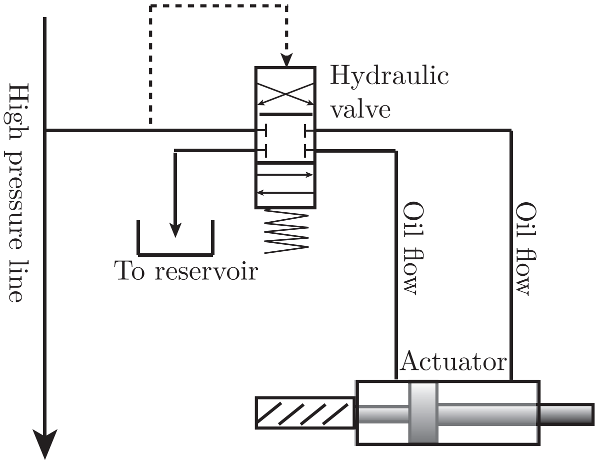

Figure 10.30: Self governed hydraulic pitch system

flow and the stiffness of the spring is tuned, so that the system is balanced at 220 *bar*. This is a low setting that will cause the system to start pitching already before rated power.

To avoid oscillations, the mass and damper is tuned so that the system is almost critically damped with $\zeta = 0.7$. This makes the system more stable, but quite a bit slower. At a later stage it would be interesting to test this kind of arrangement with a less damped system to improve the actuation speed.

A time step simulation in figure 10.31 shows how the parameter tuning eliminates overshooting and oscillations of the pitch movement. Because of the automated pitch movement, the system can be made very simple. It does not require any wind speed estimator or a complicated controller. And it probably will require only a minimum of sensors and monitoring. The model that is tested here has not been optimised in any way, which means that the performance may be suboptimal, but as an indication of how such a system could be implemented the experience is valuable.

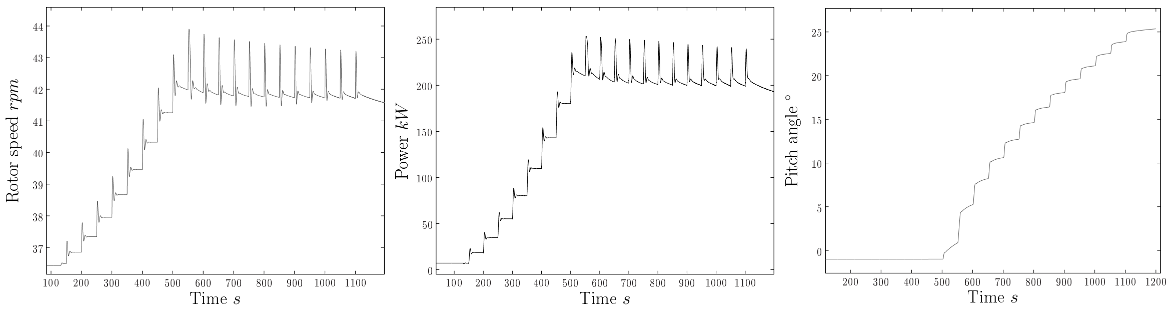

Figure 10.31: Step response of the self governed turbine

This self governed system is evaluated along with six of the above mentioned control strategies in the following chapter.

Chapter 11

Evaluation and comparison

In section 10, a number of different control strategies were established for a wind turbine with hydraulic drive train. The control systems were tested with subsequent wind steps and some full field turbulent wind simulations to check stability and to get an idea of the performance. All the different strategies were eventually found to be stable, and with different strengths and weaknesses. In order to get substantial indices on the performance of each of the control strategies in comparison with the others, a systematic analysis had to be carried out.

The IEC 61400 standard on design requirements for wind turbines presents a list of design load cases for which the wind turbine should be tested before certification [29]. This list includes, in addition to normal operation, fault situations, extreme wind gusts and loads during start-up, shut-down and parked conditions. As the aim here is not to certify the turbine, most of these load cases will not be used. Instead, a simplified load case analysis will be performed based on the load cases from the normal power production category. However, the IEC standard requires the use of five 600 second simulations, each with different seeds for the random wind speed generator, at every wind speed from cut-in to cut-out to ensure statistically independent results.

In the simplified analysis, each of the control strategies will be tested once for every wind speed from cut-in to cut-out. This limitation is applied due to time constraints, but a full analysis of all the load cases in the IEC standard could easily be run at a later point. As the name implies, FAST is a time inexpensive aeroelastic code, as it runs at approximately 2× real-time, even within the Simulink interface and with the hydraulic model. Still, to be able to test all the cases, each wind speed will only be tested for 300 seconds, half of the recommended practice. To ensure that the turbine has time to stabilize, the first 100 seconds of each simulation will be discarded, so that the total simulation time for each case will be 400 seconds. To ensure comparability, all the different control strategies have been tested with identical wind speed histories. A total of 22 turbulent wind speed sequences have been created, one for every wind speed from 3 to 24 m/s. Each of these 22 sequences have been created with different random seeds so that each wind speed input is statistically independent of the others.

The comparison will include both performance in terms of power production and damage in terms of reduced lifetime calculations. The results will be presented in three groups: For low wind speeds (below and including 9 m/s average wind), high wind speeds (above 10 m/s average wind) and totals. The reason for this division is the essential differences between operation at high and low wind speeds, and a turbine configuration that works well in limiting the power at high wind speed may not work as well in maximising the energy at low winds. To get the full picture these analyses must be carried out separately.

The performance will be evaluated according to the following criteria:

- Power production (Generator power)
- Rotor power
- Tip speed ratio

The tip speed ratio will only be presented in the low wind speed group, as this parameter gives no useful information in the other cases.

The fatigue damage will be evaluated by rain flow cycle counting of the following parameters.

1. Tower base moments in fore-aft, side-to-side and torsional directions
2. Blade root moments in in-plane and out-of-plane directions
3. Rotor speed (to indicate the wear on the gearbox (where one exists) and drive train)
4. Generator speed (to indicate the wear on the generator and drive train)

To find the differences in lifetime damage, the individual damage equivalent loads from each wind speed simulation will be weighted according to the Weibull approximation of the wind turbine distribution at Valsneset, which is shown in figure 11.1.

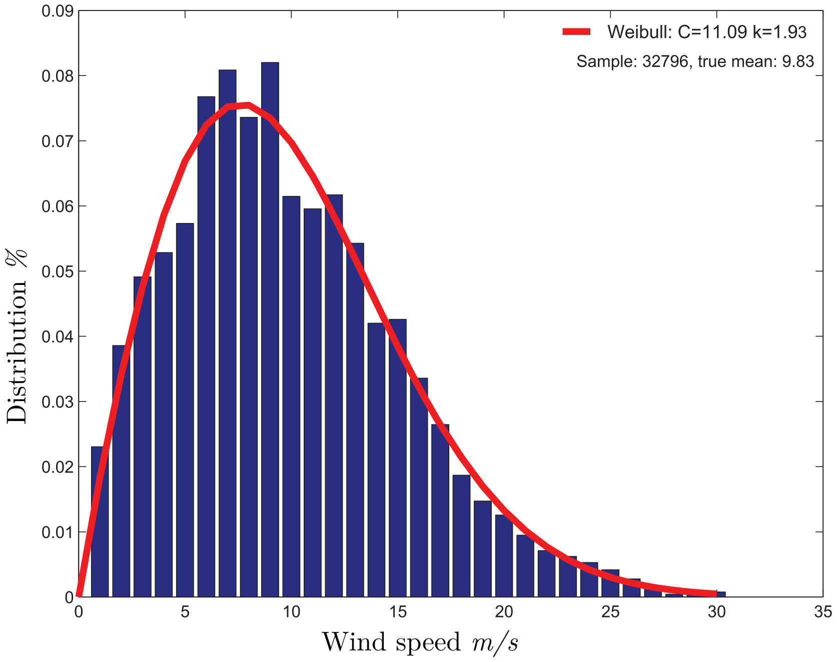

Figure 11.1: Valsneset wind distribution

The statistical and fatigue life analyses are carried out in a free-ware Matlab program called MCrunch. MCrunch is a specialized post-processing tool for wind energy applications that has the following capabilities:

- Plotting of time series.
- Binning and plotting of binned data (e.g creation of power curves from the turbine power time series and similar tasks).

- Powerful statistics capabilities through the Matlab Statistics Toolbox.
- Creation and plotting of power spectral densities.
- Rain-flow cycle counting of loads.
- Calculating probability of exceedance of loads for ultimate strength analyses.
- Calculation of damage equivalent loads and life time damage.

Further description of the capabilities and limitations can be found in the user manual, which is available from the NWTC web page [49].

Calculation of the absolute life time damage of a component requires detailed knowledge of the structural and material properties, especially the SN curves. As this information is not available for the components to be examined, the best alternative is to calculate the relative life time damage compared to that of the original V27 turbine. This means that all cases will be compared with the model of the original V27 wind turbine. For all parameters the original V27 will have value equal to one, with the other control strategies having a value larger or smaller than one, according to their performance relative to the original turbine.

The cases that will be examined are the following:

1. *Original V27* - This is the Vestas V27 with the original drive train and the pitch control system as developed in section 10.1. This is the base case that serve as a basis for comparison of the other cases.
2. *Constant gain* - This is the Vestas V27 with the ChapDrive hydraulic transmission and the maximum power point tracking speed controller with constant gains, as described in section 10.2.
3. *Gearbox subst.* - This is the Vestas V27 with the ChapDrive hydraulic transmission in the improved gearbox substitute configuration as described in section 10.3.
4. *Scheduled gain* - This is the Vestas V27 with the ChapDrive hydraulic transmission and the maximum power point tracking speed controller with scheduled gains as described in section 10.4.2.
5. *RPPT low* Ω_T - This is the Vestas V27 with the ChapDrive hydraulic transmission and the maximum power point tracking speed controller with constant gains as described in section 10.2. But the turbine is run according to the reduced power point tracking control strategy with low turbine speeds, as described in section 10.5.
6. *RPPT high* Ω_T - This is the Vestas V27 with the ChapDrive hydraulic transmission and the maximum power point tracking speed controller with constant gains as described in section 10.2. But the turbine is run according to the reduced power point tracking control strategy with high turbine speeds, as described in section 10.5.
7. *Self governed* - This is the Vestas V27 with the ChapDrive hydraulic transmission in the improved gearbox substitute configuration as described in section 10.3. The turbine uses the self governing pitch control based on the oil pressure level as described in section 10.6.

11.1 Results

The results of the aeroelastic analysis are presented through bar graphs in the next two sections. Each of the figures, except for the one presenting λ, contains three sub-figures for low wind speed, high wind speed and all wind speeds respectively. Most of the figures are self-explanatory and will only require a brief explanation. Important details, unexpected results and so on will be discussed consecutively.

Furthermore, plots of the binned power curves for both the rotor power and the generator power from all the simulations are shown in appendix B. The power curves are plotted in 1 m/s bins with all the raw data plotted on top. This is a very intuitive way of displaying all the information from the simulations. The power curves make an excellent supplement to the bar diagrams in visualizing the performance of the controllers.

Binned rotor speed and pitch angle plots created in the same manner are found in appendix C. A lot of different information on the functioning and performance of both the controllers and the turbines could be extracted by binning different parameters in this way, but because of time limitations only these four representations have been created as they are regarded as the most useful in providing information on the control system issue.

A short conclusion on the binned curves are given in section 11.2.

11.1.1 Performance

The average rotor power is shown in figure 11.2. As expected, the power at low wind speeds is a little higher for the variable speed turbines than for the fixed speed ones. The difference is however smaller than one could expect. There are several reasons for this: Firstly, as can be seen on the tip speed ratio in figure 11.3, the tip speed ratio is closer to the optimal than for the fixed speed turbines, but there is still some deviation. This is first of all due to the wind speed estimator, which predicts too high winds below 7 m/s, as can be seen in figure 9.6. By setting the rotor speed target artificially low, as in case number 5, the deviation from λ_{opt} actually decreases. This suggests that the wind speed estimator should be corrected for low wind speeds to achieve better performance. One other important point here is that Valsneset is a location with high average wind speed, so that most of the energy is in the high wind speed region. The third reason is that the two-generator solution evens out some of the differences and aids the fixed speed configurations in the low wind speed regime. At high wind speeds the modified turbines have a little higher power production than the original V27 turbine. This is because the relatively lower stiffness of the drive train makes it more difficult to control the

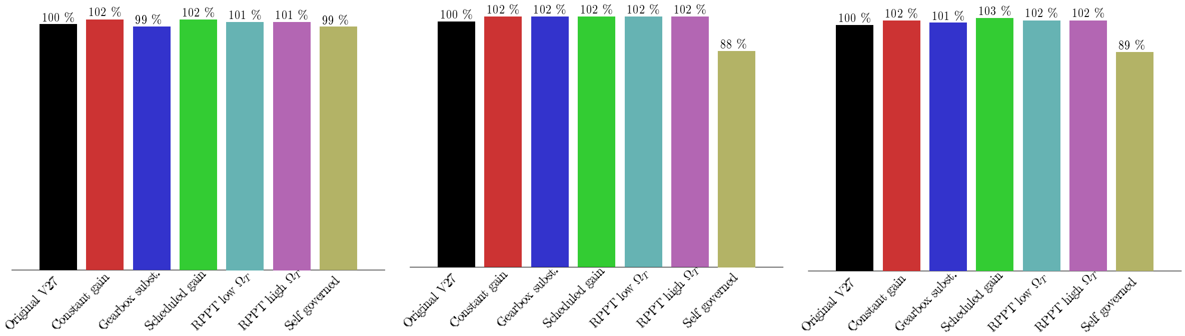

Low wind High wind Total

Figure 11.2: Relative average rotor power

power. The exception is the self governed turbine. The reason for this is that the relief valve for the pitch actuator is set at 220 bar. This means that this turbine will start pitching before the turbine reaches its rated power.

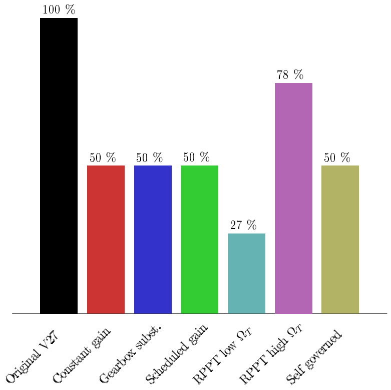

Low wind

Figure 11.3: Relative average deviation from λ_{opt}

The generator power curves are shown in figure 11.4 and shows the same trends as the rotor power. The difference is that the losses in the hydraulic pump and motor and the pressure loss in the pipes reduces the efficiency and thus also the generated power.

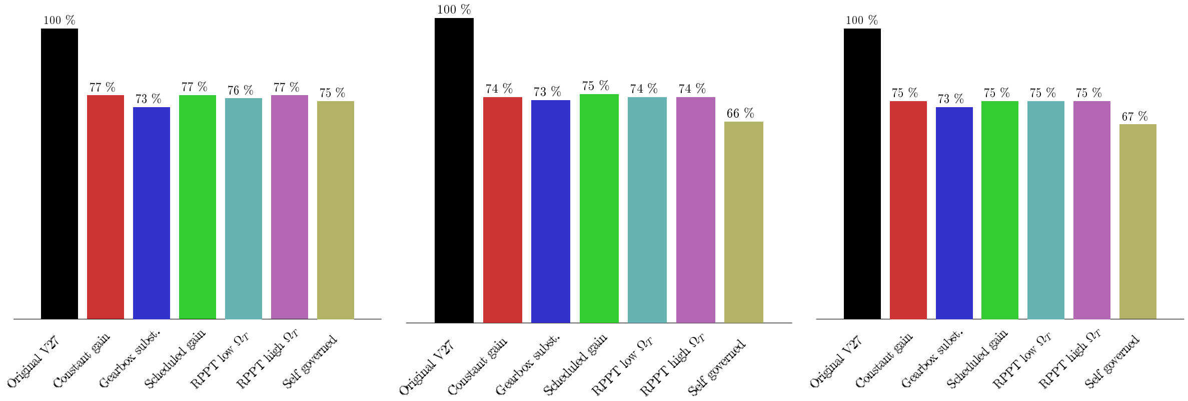

Low wind

High wind

Total

Figure 11.4: Relative average generator power

11.1.2 Fatigue life time damage

The in-plane, blade root cumulative damage is shown in figure 11.5. The damage is quite similar for all of the models, but the hydraulic transmission clearly has a positive effect. The reason for this is probably because the low stiffness off the drive train allows the rotor to accelerate when subject to a wind gust. With the stiff shaft of the original turbine, the rotor speed will be more stable causing higher and more sudden loads on the blade root.

The damage of the out-of plane blade motion shows the same trend at low wind speeds, probably due to the same reasons. The exception is the gain scheduled configuration. The reason for this is not known, but the speed controller of this turbine is quite aggressively tuned. It is possible that this has caused some oscillations, causing this kind of result.

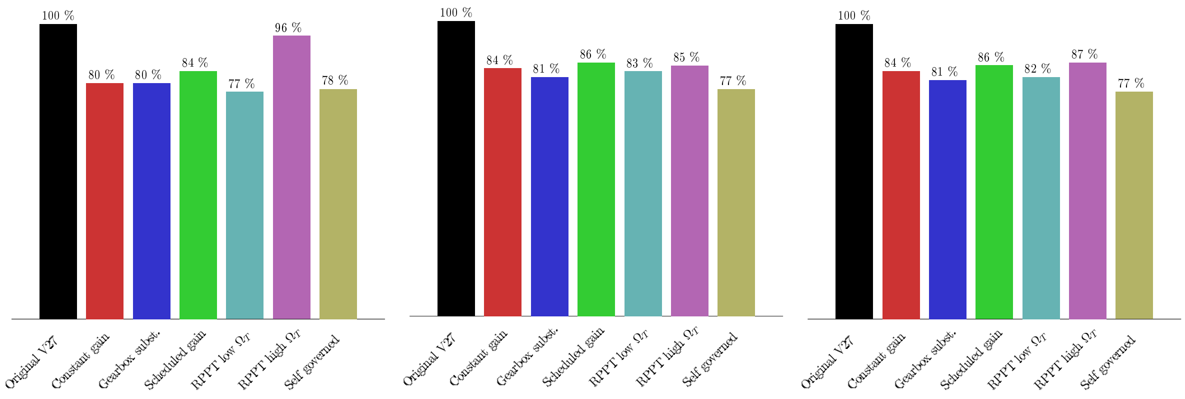

Low wind High wind Total

Figure 11.5: Relative in-plane blade root moment damage

At high wind speeds, the opposite trend is evident. The reason for this is probably that the pitch controller is tuned less aggressively, so that blades are not pitched fast enough to relieve the blades at high wind speeds.

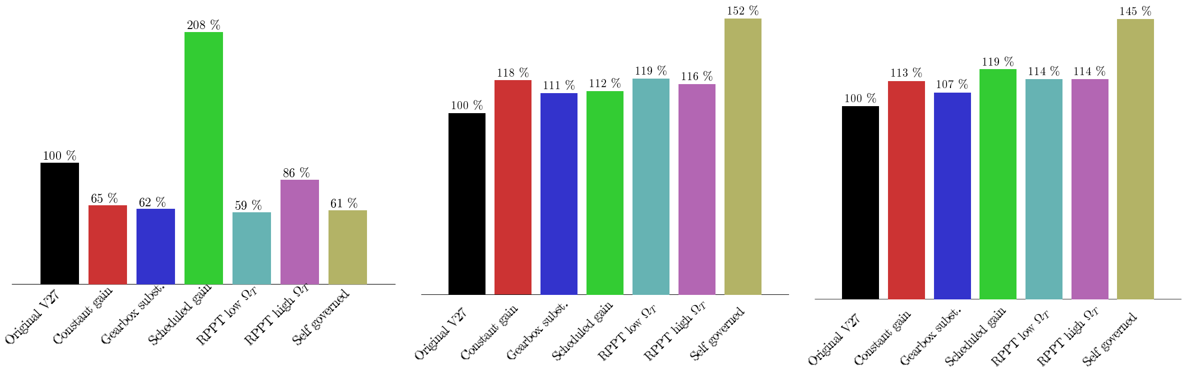

Low wind High wind Total

Figure 11.6: Relative out-of-plane blade root moment damage

The side-to-side fatigue damage on the tower base is shown in figure 11.7. The diagram for the low speed is quite strange, but because the damage from the low wind speeds clearly are negligible, this has not been investigated further. At high wind speeds three of the speed controlled hydraulic transmissions cause more loading on the tower, while the gain scheduled turbine and the fixed displacement configurations are approximately levelled with the original turbine. The three configurations have exactly the same speed and pitch control implementation at high wind speeds, and thus have the same damage. Why these cause more damage than for instance the gain scheduled turbine is not known. It might have to do with resonance caused by the speed control settings, but this should be investigated further.

The fore-aft damage on the tower base is shown in figure 11.8. The damage higher for the hydraulic turbines at low speed, except the high speed RPPT and the self governed turbine. Therefore the explanation probably has something to do with the turbine rotational speed: The suggestion is that the loading in general should be lower, like they were for the out-of-plane blade loads, but that the proximity to the 1^{st} natural tower frequency (see e.g figure 8.5) has caused some increased loading. At high wind speeds the fore-aft loading is lower. This is not as expected, as they should be closely related to the out-of-plane blade loadings in figure 11.6.

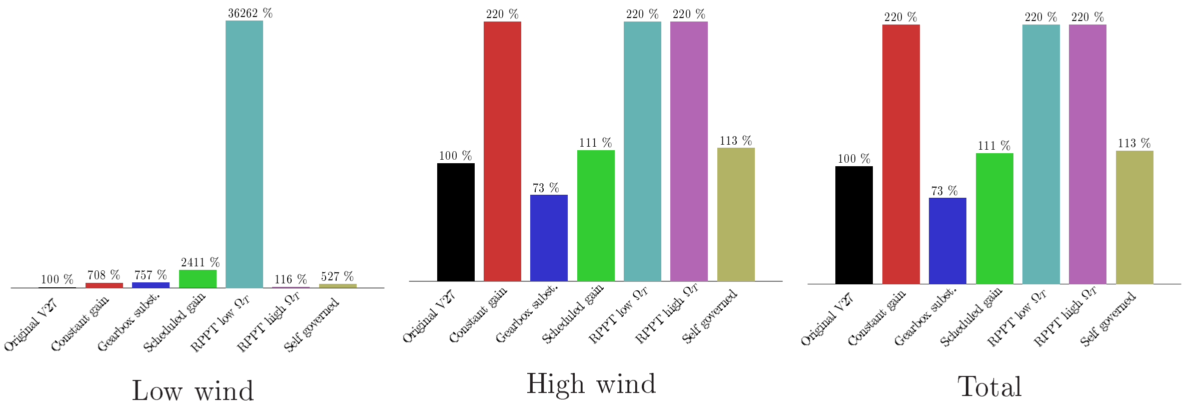

Figure 11.7: Relative side-to-side tower root moment damage

Why the self-governed turbine has lower loads for the low wind speeds and higher loads for the high wind speeds is not known, but the self controlled pitch mechanism is slower than the controlled pitch systems and that might be the reason. The self-governed turbine had higher out-of-plane blade loads too.

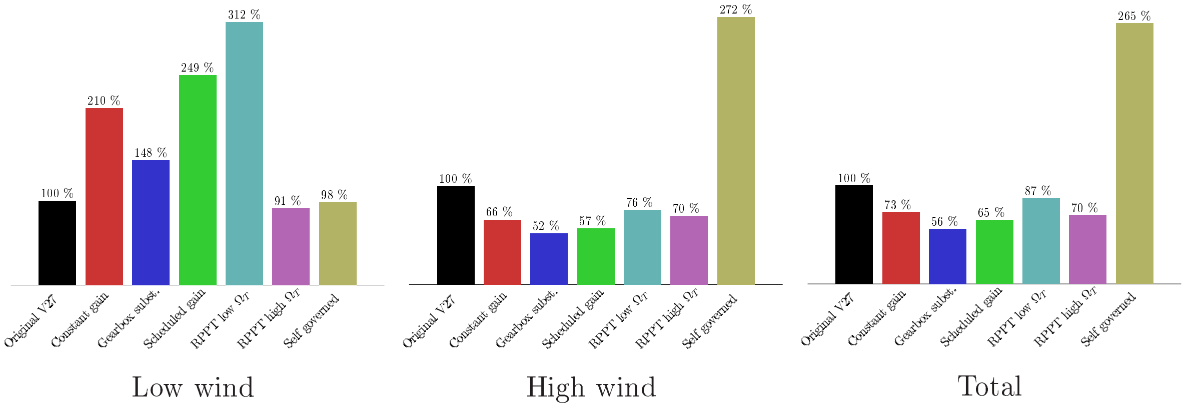

Figure 11.8: Relative fore-aft tower root moment damage

The relative torsional fatigue loading at the tower base is shown in figure 11.9. At low winds all the hydraulic drive train turbines, except the gain scheduling approach, have considerably lower torsional loading than the original turbine. At high wind speeds the damage is approximately equal. What causes the difference in torsional loading is difficult to say as no yaw mechanism has been involved. No explanation to this has been found, but the implications for the total torsional loading is not dramatic.

The fatigue life calculations for the low speed shaft is shown in figure 11.10, and the damage on the high speed shaft is shown in figure 11.11. Fatigue damage on the turbine shafts is generally not an important issue, as it is easy to make these components strong enough. The reason why these parameters are included here is to show the implications the hydraulic circuit will have on the generator, and consequently the produced electricity. The damping effect that the hydraulic circuit has on the rotational oscillations is clearly shown by the relative difference of the damage between the low speed and the high speed shaft. One of the possible benefits of the hydraulic transmission, in addition to saving nacelle weigh, is that it may be possible to use a synchronous generator, with the advantage this has on the stability in the grid, especially when considering offshore applications. Induction generators consumes a lot of reactive power,

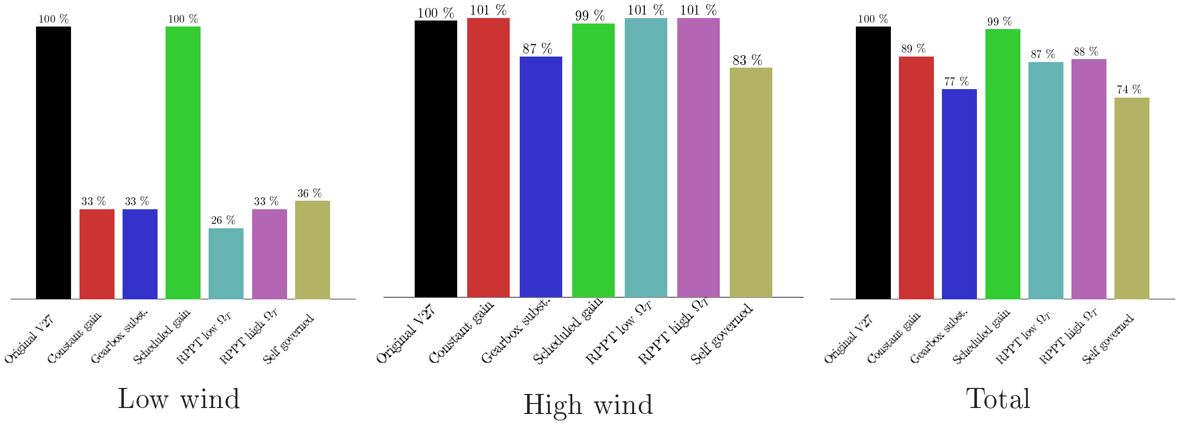

Low wind High wind Total

Figure 11.9: Relative torsional tower root moment damage

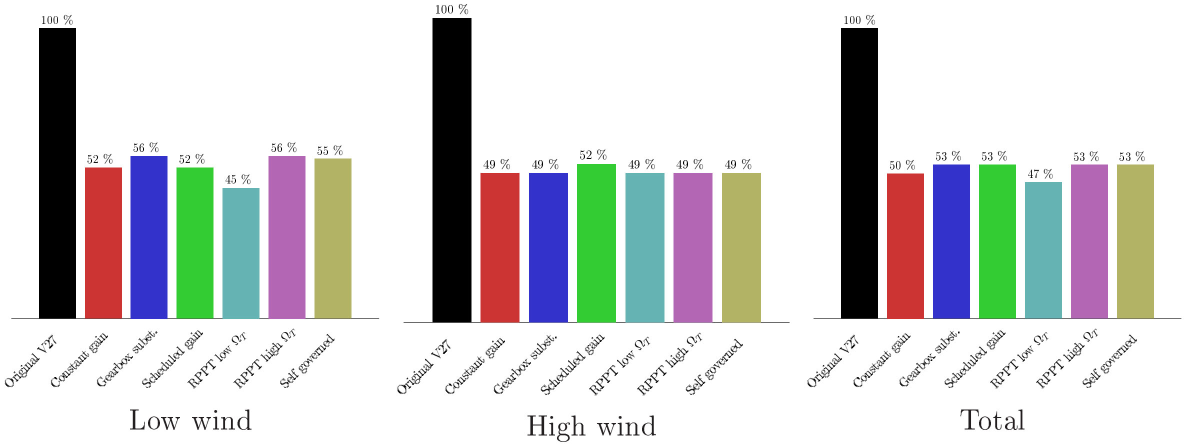

Low wind High wind Total

Figure 11.10: Relative low speed shaft damage

which causes problems in remote areas. In an offshore wind farm the electrical losses would be considerably less with synchronous generators, and the reliability of the grid would be better as the synchronous machine, as opposed to the induction machine, is able to maintain its own grid.

One of ChapDrive's main objectives at the present stage is the ability to use a synchronous generator in their concept. The drastically reduced high speed shaft oscillations indicates that this might be feasible and yield very good dynamic behaviour.

11.2 Comments on the results in appendix B and C.

The power and pitch angle curve of the original V27 turbine simulation shows very good correlation with the target power curve from figure 9.2. This suggests that the pitch control system is a good approximation of the pitch control system in the prototype.

The power curves for the hydraulic transmission turbines is showing good characteristics at low wind speeds, but they could probably be even better if the wind speed estimator was working better for the lowest wind speeds. The hydraulic turbine reaches rated power at a wind speed of approximately 14 m/s, but after that it shows some strange behaviour: First it dips a little until 17 m/s before it starts increasing steadily again. This dip will reduce the

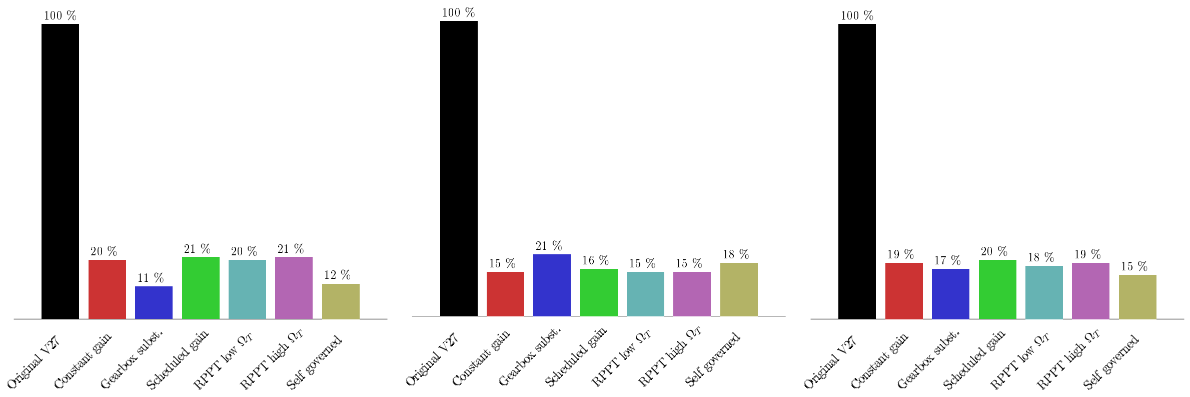

Low wind High wind Total

Figure 11.11: Relative high speed shaft damage

produced power noticeably, and should be avoided. Another important thing to observe is that the control system is not able to limit the power well enough for the highest wind speeds. The power curve increases beyond the 225 kW limit for wind speeds above approximately 22 m/s.

It is not sure exactly what causes this strange behaviour: Both the speed and the pitch control curves of the hydraulic turbines seem very well-behaved. The strange behaviour is also seen in the power curve of the self governed turbine and the turbine with the gearbox substitute. Further investigation is needed to reveal what causes the undesirable behaviour.

An interesting observation is that the scattering of the measurement points is more controlled in the hydraulic turbines than the original, both for the turbine power and the generator power. This despite that the hydraulic turbines have much larger deviations in the rotor speed. This is probably related to the generally lower high wind fatigue damage that has been observed in the hydraulic turbines versus the conventional one.

Chapter 12

Discussion and conclusion

Aeroelastic model

The idea of using an aeroelastic model in simulations of wind turbines is to be able to capture the highly coupled aerodynamics and structural dynamics. To get a useful result, it is imperative that the both the structural and aerodynamic models are as accurate as possible.

The aeroelastic model has been developed based on the information provided in the documentation and manuals supplied with the Vestas V27 wind turbine. From these data, a complete aerodynamic and structural model of the blades and the tower has been created. During this process, some assumptions has had to be made, as not all of the necessary information has been found. For this reason, there is no guarantee that the model is correct in its entirety.

The turbine blades are the parts that are the most uncertain: The aerodynamic properties are found using XFOIL. Experimental works has shown that it is difficult to produce accurate lift and drag curves from XFOIL [33], and therefore one can assume that the aerodynamic representation is a weakness in the model. The aerodynamics has been attempted verified by comparison with known data on the Vestas V27. The developed aerodynamic properties showed good correlation with the optimal pitch angle and with the power curve. For this reason it is concluded that the developed aerodynamic properties are reasonable.

The structural properties of the blades are also uncertain, as only the flapwise stiffness was provided. The edgewise stiffness distribution was then reconstructed in an iterative process using a finite element modelling code called PreComp. When both the geometry, the mass distribution and the flapwise stiffness distribution was reproduced in PreComp, it was assumed that the calculated edgewise stiffness also was correct. However, these data should be verified. IFE has done some structural testing on the blades of a V27 turbine, but it has not been possible to retrieve them. For future analyses, the analytical data should be verified against these measurements

The tower model is believed to be quite accurate as the tower is a simple steel structure. The tower structural properties were computed using PreComp, and the results has been verified by a similar calculation in GH Bladed in [21].

The aeroelastic code shows some weaknesses, both in the treatment of the structural dynamics and the aerodynamics: FAST uses a very limited number of mode shapes for the blades and the tower compared to for instance GH Bladed. Also the lack of an up-wind tower shadow model reduces the accuracy of the code. The program is, however under constant development, and it has been stated that a better model of the tower shadow is about to be implemented.

What implications these weaknesses has with regards to the results is not known. A similar aeroelastic model as the one developed in this thesis is being developed by Per Olav Haarberg from ChapDrive in GH Bladed. This means that it soon will be possible to verify the two models against each other by inputting similar structural and aerodynamic characteristics.

No results has been found that indicates that the model is experiencing incorrect behaviour or that any fundamental errors exist in the model or the aeroelastic solver.

Hydraulic model

The modelled hydraulic system is quite advanced, including friction models, fluid inertia, a boost system and relief valves. This means that much of the actual drive train dynamic effects can be simulated. The hydraulic model is largely based on a similar model that was developed during the project thesis. Only small changes has been applied to account for the differences between the two prototypes. The hydraulic circuit was thoroughly investigated and analysed in the project thesis and found to be reasonably accurate. For this reason the hydraulic model is considered to be sufficiently good. All simulations indicate that the hydraulic transmission is well-behaving and physically correct.

A hydraulic model for simulations in GH Bladed is currently under development by Garrad Hassan. When that model is finished it can be used for verification of hydraulic transmission used herein.

Control system

The main objective of this thesis was to develop and analyse different possibilities in control systems for wind turbines with a hydraulic transmission. The nature of the hydraulic transmission makes it more challenging to govern, and a lot of stability issues have been seen. The analyses indicates that these issues could be traced back to the heart of the control system, which is the wind speed estimator. The WSE calculates the apparent wind speed based on torque and rotor speed measurements and uses this information to set the target speed, pitch and power. Analyses of the WSE for the conventional turbine show exceptionally good estimates, but it turned out that the slower dynamics in the ChapDrive concept caused interference and self-excitation between the two controllers. To solve this problem an ad-hoc solution was found: Using a low pass filter with 10 s filtering time on the pitch target setting, the system was stabilised, but with a cost: The pitch response speed was somewhat reduced relative to that of the conventional turbine.

Another important issue with the WSE is the poor low wind speed performance: The wind speed estimator predicted too high wind speeds below 7 m/s. This in turn caused the turbine to run at a tip speed ratio above optimal. The most important feature of a variable speed turbine is to run at the optimal tip speed ratio below rated speeds to maximize the energy. This suggests that the wind speed estimator should be improved at low wind speeds. Exactly what causes the inaccuracy below 7 m/s is not known. The look-up table used was created according to blade element theory, and the lower limit of the table was set as low as 2 m/s wind speed to ensure that all operation points should be covered, but that is obviously not the case in practise.

A total number of six versions of the turbine control system was created, in addition to the one resembling the control system of the original V27 turbine. Most of them with only small individual differences. All these control strategies were successfully stabilised, but the performance leaves something to be desired, both at low winds as explained above and at high wind speeds as was seen in the power curves.

It has been shown that the control system with active speed control is superior to the gearbox substitute, which uses fixed motor displacement. A gain scheduling controller was created in order to improve the performance both at low and high wind speeds, but the improvement over the constant gain version was not dramatic. Two reduced power point tracking strategies were also tested, but the results are not very useful. The reason for this is that the poor low wind speed performance of the WSE resulted in that all the variable speed turbines were running at incorrect tip speed ratio.

In addition to these relatively conventional control systems a novel approach was tested: A turbine with direct feeding of the pitch actuators from the high pressure line when the pipe pressure increased above a certain level. The idea of this implementation is primarily for adding extra safety to the turbine in case of fault in the control system. However, in this analysis the self governing turbine was tested on equal terms with the other control strategies, but it turned out to have inferior performance both at low and high wind speeds. It is believed, however, that tuning of the parameters could increase the performance somewhat.

Fatigue analysis

The energy in the wind is free, so the cost of wind energy is only related to construction and maintenance of the turbine. Constructing turbines less vulnerable to fatigue damage could then improve the economics of wind energy considerably through longer lifetime and less maintenance costs.

Wind turbine fatigue is an important subject in the wind energy industry, and much of the present academic work on wind turbine control relates to methods of reducing the fatigue. But because the ChapDrive concept is so novel, a fatigue analysis of this kind of wind turbine has never been carried out before. The dynamics are fundamentally different from conventional turbines, and so also the fatigue damage.

The out-of-plane fatigue damage of the blade root was found larger for the turbines with hydraulic transmission than for the conventional, while the in-plane damage showed the opposite trend. Strangely, the exact opposite was found in the tower fore-aft and side-to-side loading: The speed controlled ChapDrive concept had more fatigue damage in the side-to-side direction and less in the fore-aft direction. A good explanation for this has not been found, but it is possible that it has to do with the frequency of the oscillations in the rotor speed. The hydraulic turbine has much lower frequency oscillations, and it is possible that this has caused larger oscillations in the side-to-side direction of the tower. The strange thing was that it was only the three of the turbines with active speed control that had higher tower side-to-side damage. The fixed displacement turbines and the gain scheduled turbine were approximately levelled with the conventional turbine. After this strange discovery was made an inspection of the statistics for the tower-top side-to-side displacement revealed that the maximum displacement was 26 % larger for the turbine with the hydraulic transmission. This suggests that some oscillations could have been taking place, but it could also be incidental. More simulations are needed to verify this.

The largest difference between the two concepts was found in the oscillations on the high speed and low speed shafts. As expected, the ChapDrive concept had less oscillations: Only half as much oscillations in the low speed shaft and only one fifth of the oscillations in the high speed shaft. This will have large implications on the controllability of the generator and on the power quality delivered to the grid.

It must be noted that the size of the data material is limited to 300 seconds for each wind speed. In order to get a better basis for the statistical data, simulations should be carried out according to the recommendations in the IEC standard with 5 statistically independent 600 second simulations for each wind speed. This has not been possible due to time constraints.

Chapter 13

Proposal for further work

There are three areas that should be pointed out for further work:

- Most importantly the models should be verified. This goes both for the hydraulic model, the structural model for the blades and of course the aerodynamics. The last part is rather difficult, as Vestas will not reveal the aerodynamic characteristics of the turbine. The aerodynamic model in FAST should also be further verified against the model in Bladed.

- The control systems need more work, in order to reduce the oscillations and to improve the low wind speed performance. It seems like most of the problems related to the control system can be traced back to the wind speed estimator. More advanced wind speed estimators, based on higher order models or Kalman filtering are discussed in [41], showing promising results. Such an approach might yield better results for the present turbine due to the slower dynamics.

- The control system proposed should also be tested on the prototype turbine to see if the actual response is similar to the simulated. This would serve as a verification of the models and provide more experience in running the ChapDrive concept at variable speed.

Bibliography

[1] Ira Herbert Abbott and Albert Edward Von Doenhoff. *Theory of Wing Sections.* Dover Publications Inc. New York, 1959.

[2] Anders Ahlström. *Aeroelastic Simulation of Wind Turbine Dynamics.* PhD thesis, Royal Institute of Mechanics, Stockholm, 2005.

[3] Anders Ahlström. *Aeroelastic simulation of wind turbine dynamics.* PhD thesis, Royal Institute of Technology, Stockholm, 2005.

[4] A. Akers, Max P. Gassman, and Richard Smith. *Hydraulic Power System Analysis.* Taylor & Francis, New York,, 2006.

[5] Christian Bak, Peter Fuglsang, Niels N. Sørensen, and Helge Aagaard Madsen. Airfoil characteristics for wind turbines. Technical report, Risøe National Laboratory and Technical University of Denmark, 1999.

[6] Jens G. Balchen, Trond Andresen, and Bjarne A. Foss. *Reguleringsteknikk.* NTNU-trykk, Trondheim, 2003.

[7] Fernando D. Bianchi, Hernán De Battista, and Ricardo J. Mantz. *Wind Turbine Control Systems: Principles, Modelling and Gain Scheduling Design.* Springer, London, 2006.

[8] Ommund Birkenes. The evaluation of hydraulic systems for power generation for wind turbines. Master's thesis, NTNU, 2005.

[9] E. A. Bossanyi. *GH Bladed - Theory Manual.* Garrad Hassan, 2007.

[10] Simon-Philippe Breton. *Study of the stall delaty phenomenon and of wind turbine blade dynamics using numerical approaches and NREL's wind tunnel tests.* PhD thesis, NTNU, 2008.

[11] Peter John Chapple. Wind turbine dynamic equations - case of fixed generator speed. Internal ChapDrive report, August 2005.

[12] P. K. Chaviaropoulos and M. O. L. Hansen. Investigating three-dimensional and rotational effects on wind turbine blades by means of a quasi-3d navier-stokes solver. *Journal of Fluids Engineering*, 122, June 2000.

[13] Cristian Nichita, Dragos Luca, Brayima Dakyo, and Emil Ceanga. *Large Band Simulation of the Wind Speed for Real Time Wind Turbine Simulators*, volume 17 of *IEEE Transactions on Energy Conversion*, 2002.

[14] DNV/Risø. *Guidelines for design of wind turbines - Second edition*, 2002.

[15] Mark Drela. http://web.mit.edu/drela/public/web/xfoil/. Web page.

[16] Lars Frøyd. Modeling, simulation and control of a wind turbine with hydraulic drive train. Technical report, NTNU, 2008.

[17] Peter Fuglsang, Christian Bak, Mac Gaunaa, and Ioannis Antoniou. Design and verification of the risø-b1 airfoil family for wind turbines. Technical report, Risøe National Laboratory, Roskilde, Denmark, 2004.

[18] G. D. Moor and H. J. Beukes. *Maximum Power Point Trackers for Wind Turbines*, volume 35 of *Annual IEEE Power Electronics Specialists Conference*, 2004.

[19] A. B. Goodwin. *Fluid Power Systems, Theory, Worked examples and problems.* The Macmillan Press Ltd. London, 1976.

[20] Per Olav Haarberg. The evaluation of hydraulic transmission from a tidal turbine. Master's thesis, NTNU, 2005.

[21] Per Olav Haarberg. Project thesis - ba8607 windturbine design. Technical report, NTNU, 2009.

[22] Keld Hammerum. A fatigue approach to wind turbine control. Master's thesis, Technical University of Denmark, 2006.

[23] A. Craig Hansen and David J. Laino. User's guide to the wind turbine aerodynamics computer software aerodyn. Technical report, Windward Engineering, 2002.

[24] Morten Hartvig Hansen, Mac Gaunaa, and Helge Aagaard Madsen. A beddoes-leishman type dynamics stall model in state-space and indicial formulations. Technical report, Risøe National Laboratory, Roskilde, Denmark, 2004.

[25] Svein Kjetil Haugset. Design av vindturbiner. Master's thesis, NTNU, 2007.

[26] Svein Kjetil Haugset and Marit Reiso. Project thesis - ba8607 windturbine design. Technical report, NTNU, 2009.

[27] Hägglunds Drives. *Product Manual COMPACT -EN396-8h*, 2004.

[28] Danmei Hu, Ouyang Hua, and Zhaohui Du. A study on stall-delay for horizontal axis wind turbine. *Renewable Energy*, 31(6), 2006.

[29] International Electrotechnical Commission. *IEC 61400 Wind turbines - part 1: Design requirements. Third edition*, 2005.

[30] Fridtjov Irgens. *Formelsamling Mekanikk*. Tapir akademisk forlag, Trondheim, 1999.

[31] Jason Jonkman. http://wind.nrel.gov/designcodes/simulators/fast/. last modified 12-august-2005. FAST distribution archive.

[32] Torben Juul Larsen. Hawcii course material.

[33] Helge Aagard Madsen and Antonino Filippone. Implementation and test of the xfoil code for airfoil analysis and design. Technical report, Risøe National Laboratory, Roskilde, Denmark, 1995.

[34] J. F. Manwell, J. G. McGowan, and A. L. Rogers. *Wind Energy Explained*. John Wiley & Sons, 2002.

[35] V. Parezanovic, B. Rasuo, and M. Adzic. Design of airfoils for wind turbine blades. Technical report, University of Belgrade, Serbia, 2005.

[36] Ove Jørås Pettersen. Modelling and simulation of wind turbines. Master's thesis, NTNU, 2007.

[37] Kirk Gee Pierce. Wind turbine load prediction using the beddoes-leishman model for unsteady aerodynamics and dynamic stall. Master's thesis, University of Utah, 1996.

[38] Risøe National Laboratories. *Description of Nordtank 500/41 at Risøe National Laboratories*, 2003.

[39] D.M. Sommers and M.D Maughmer. Theoretical aerodynamic analyses of six airfoils for use on small wind turbines. Technical report, National Renewable Energy Laboratory, USA, 2002.

[40] Niels N. Sørensen. Transition prediction on the nordtank 500/41 turbine rotor. Technical report, Risøe National Laboratory, Roskilde, Denmark, 2002.

[41] K. Z. Østergaard, P. Brath, and J. Stoustrup. Estimation of effective wind speed. *Journal of Physics*, 2007.

[42] James L. Tangler and Michael S. Selig. An evaluation of an empirical model for stall delay due to rotation for hawts. Technical report, National Renewable Energy Laboratory, USA, 1997.

[43] Torbjörn Thiringer and Jan Linders. *Control by Variable Rotor Speed of a Fixed Pitch Wind Turbine Operating in a Wide Speed Range*, volume 8 of *IEEE Transactions on Energy Conversion*, 2004.

[44] Steffen Andreas Varpe. Field measurement on a wind turbine. Technical report, NTNU, 2007.

[45] Steffen Andreas Varpe. Control system on a wind turbine. Master's thesis, NTNU, 2008.

[46] Vestas. V27 specifications: 13 m rotorblade geometri. Internal Vestas document.

[47] Vestas. *Elektrisk Service og Vedlikeholdelses Manual. Vestas V27/V29-225 kW*, 1994.

[48] Antonio Visioli. *Practical PID Control*. Springer, London, 2006.

[49] NWTC web page. http://wind.nrel.gov/.

[50] Frank M. White. *Fluid Mechanics - Fifth Edition*. McGraw-Hill, New York, 2003.

Appendix A

Linear analysis

Linear system equations

The derivation of these equations is based on similar work done by *Peter Chapple* 2005 [11]. In the following, capital letters (i.e Ω_T, D_M, P) will be used for the states at the linearisation points ($\theta(\Omega_T, \mathcal{V})$), while minuscules (i.e ω_T, d_M, p) will be used to denote changes of the state variables close to θ.

Flow equations

For the pipe flow the compressible continuity equation (from equation 6.1) is used:

$$\frac{\mathrm{d}\Delta P}{\mathrm{d}t} = \frac{\beta}{V}(\Omega_T D_P - \Omega_M D_M - C_L(P_1 - P_2)) \tag{A.1}$$

Where C_L is the combined internal and external leakage coefficient for both the motors and the pump. A linearisation is applied for small deviations about a linearisation point $\theta(\Omega_T, \mathcal{V})$:

$$\mathrm{d}(D_P \Omega_T)|_{\Omega_T,\mathcal{V}} = D_P \omega_T + \cancel{d_P \Omega_T} \tag{A.2}$$

$$\mathrm{d}(D_M \Omega_M)|_{\Omega_T,\mathcal{V}} = \cancel{D_M \omega_M} + d_M \Omega_M \tag{A.3}$$

$$\mathrm{d}\Delta P|_{\Omega_T,\mathcal{V}} = p_1 - \cancel{p_2} = p \tag{A.4}$$

$$\mathrm{d}(C_L P)|_{\Omega_T,\mathcal{V}} = C_L p + \cancel{c_L P} \tag{A.5}$$

Then the equation is Laplace transformed and ordered with respect to ω_T, yielding:

$$\omega_T = \frac{(\frac{V}{\beta}s + C_L)p}{D_P} + \frac{d_M \Omega_M}{D_P} \tag{A.6}$$

Rotor equations

For the turbine rotor dynamics, Newtons second law in angular direction is used:

$$\frac{\mathrm{d}\Omega_T}{\mathrm{d}t} = \frac{1}{J_T}(-T_T + T_P) = -\frac{1}{J_T}(C_T \Omega_T + \Delta P \frac{D_P}{\eta_{mech}}) \tag{A.7}$$

Where C_T is defined as

$$C_T = -\frac{\partial T_T}{\partial \Omega_T}|_\theta \tag{A.8}$$

the negative local slope of the T_T–Ω_T curve for a given linearisation point. A linearisation is applied for small deviations about a linearisation point $\theta(\Omega_T, V)$:

$$\mathrm{d}(C_T\Omega_T)|_{\Omega_T,\mathcal{V}} = C_T\omega_T + \cancel{c_T\Omega_T} \tag{A.9}$$

$$\mathrm{d}(\Omega_T)|_{\Omega_T,\mathcal{V}} = \omega_T \tag{A.10}$$

$$\mathrm{d}(\Delta P D_P)|_{\Omega_T,\mathcal{V}} = pD_P + \cancel{\Delta P d_P} \tag{A.11}$$

Then the equation is Laplace transformed and ordered with respect to ω_T, yielding:

$$\omega_T = -\frac{pD_P/\eta_{mech}}{Js + C_T} \tag{A.12}$$

Speed control analysis

For a non-linear system a PID controller can be designed by trial and error, with repeated simulations to find the best parameter settings. If the system is linearised, however, linear control theory can be applied, with a large toolbox of analytical design- and optimization methods available.

Because of the non-linearities of the system the equations will have to be linearised around specific linearisation points, $\theta(\Omega_T, \mathcal{V})$ in which both turbine speed and wind speed is known. The linearisation points will lie on the Ω_T – T_T locus of figure 9.3.

The feedback loop of the speed controller, in the simplest possible form, will look like the one in figure A.1. The controller acts on the deviation $\Delta\omega$ of the turbine speed ω_T from the reference speed, and produces a signal to the actuator that changes the motor swash plate angle. The finite time response of the actuator is represented by a first order transfer function with time constant $\mathcal{T}_A$ and gain K_A. The change in displacement d_M then causes a change in turbine speed according to the transfer function $H_1(s)$, which will be established based on linear equations for the rotor dynamics and the pipe flow respectively. Based on the equations derived above we get:

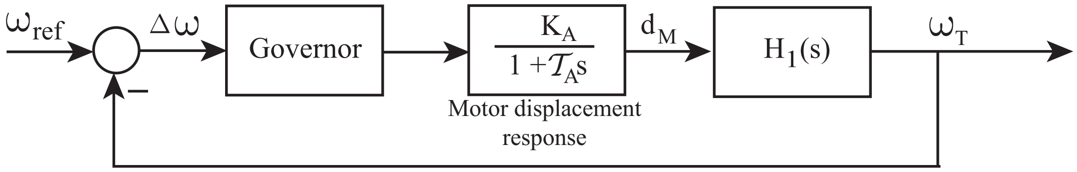

Figure A.1: Basic TSC feedback loop block diagram

$$\omega_T = -\frac{pD_P/\eta_{mech}}{Js + C_t} \tag{A.13}$$

$$\omega_T = \frac{(\frac{V}{\beta}s + C_L)p}{D_P} + \frac{d_M\Omega_M}{D_P} \tag{A.14}$$

Where C_L is the combined internal and external leakage coefficient for both the motors and the pump, and C_t is defined as:

$$C_t = -\frac{\partial T_T}{\partial \Omega_T}|_\theta \tag{A.15}$$

C_t, also known as the aerodynamic damping coefficient, is the negative local slope of the T_T–Ω_T curve for a given linearisation point as explained in figure A.2. When C_T is positive, a small increase in Ω_T will cause an decrease in T_T which tends to stabilize the rotor, but when it is negative a small increase in Ω_T will cause an increase in T_T which couses futher acceleration of the rotor. Negative damping will cause oscillations or even instability of the system. C_t is one of the most important non-linearities in the system and this must be included in the linear analysis. For a stall controlled wind turbine the C_T coefficient will become negative at high wind speeds, but pitching of the turbine blades will increase the damping. The aerodynamic damping coefficient of the Vestas V27 is shown in figure A.3

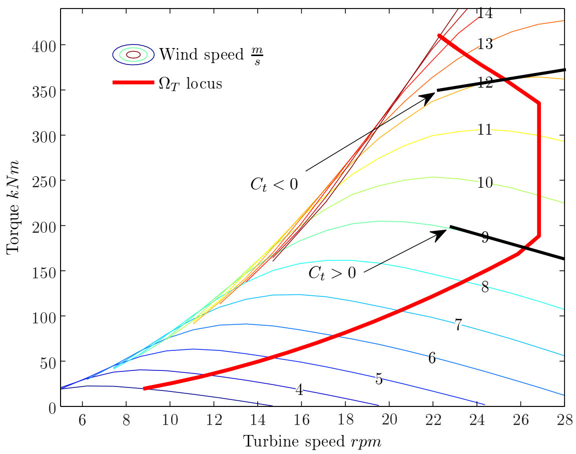

Figure A.2: Change in C_t along Ω_T locus. Non-pitched blade

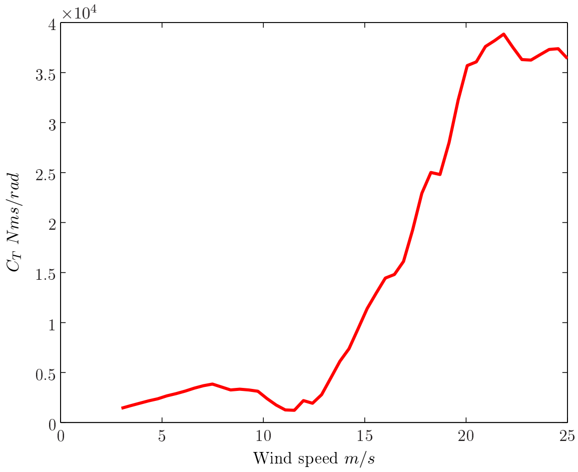

Figure A.3: Aerodynamic damping coefficient of the ideally pitched turbine

When combining equation A.13 and A.14 and eliminating p, the transfer function from d_M to ω_T can be found as a second order transfer function:

$$\frac{\omega_T}{d_M} = H_1(s) = \frac{K_\omega}{s^2 + 2\zeta_1\omega_1 s + \omega_1^2} \tag{A.16}$$

Where

$$K_\omega = \frac{D_P \Omega_M \beta}{V J_T \eta_P} \tag{A.17}$$

$$\omega_1 = \sqrt{\frac{\beta \eta_P D_P^2}{V J_T} K_1} \tag{A.18}$$

$$K_1 = 1 + \frac{C_t C_L \eta_P}{D_P^2} \tag{A.19}$$

$$\zeta_1 = \frac{1}{2 D_P \sqrt{\eta_P K_1}} \left(C_t \sqrt{\frac{V}{\beta J_T}} + C_L \sqrt{\frac{\beta J_T}{V}} \right) \tag{A.20}$$

ζ_1 and ω_1 is the damping coefficient and natural frequency of the equivalent mass-spring-damper system, respectively. These coefficients will vary along the turbine speed locus. The critical value of C_t to maintain positive damping ζ_1 will be:

$$C_t \, C_L \frac{J_T \beta}{V} \tag{A.21}$$

This equation clearly identifies some important features that influence the stability: C_t and J_T are dependent on the turbine rotor and cannot be altered. But the ratio β/V, the stiffness of the hydraulic system, should be kept as high as possible to increase the stability. Increased leakage will also improve the damping ratio, which is a well known phenomenon in hydrostatic transmissions [19]. The leakage is determined by the motor and pump geometries, but the equation suggests that the leakage could be increased artificially by bleeding off the system through valves at critical operational points, to improve stability if oscillations occur. This approach has not been pursued further in this thesis, but the principle has been tested with some success on the actual turbine.

Pressure feed-back damping

Another way to improve stability is to use damping injection from pressure feedback [11]. The idea is to introduce a feedback loop from a pressure measurement, which is then added to the input to the swash plate actuator. The principle is shown in figure A.4. $H_2(s)$ is the transfer function from a small change d_M of the motor displacement to a change in pressure. And $H_3(s)$ is a transfer function that specifies how a small change in the pressure level should affect the motor displacement actuator. The reason why the pressure injection contributes positively to the damping is because of the low inertia of the pipe system compared to the rotor: When the rotor experiences a disturbance the speed will increase slowly, but a small increase in Ω_T will result in a rapid increase in pressure. When this pressure increase is fed back the motor displacement actuator will increase D_M before Ω_T reaches its peak and thus the amplitude of the oscillations will be reduced.

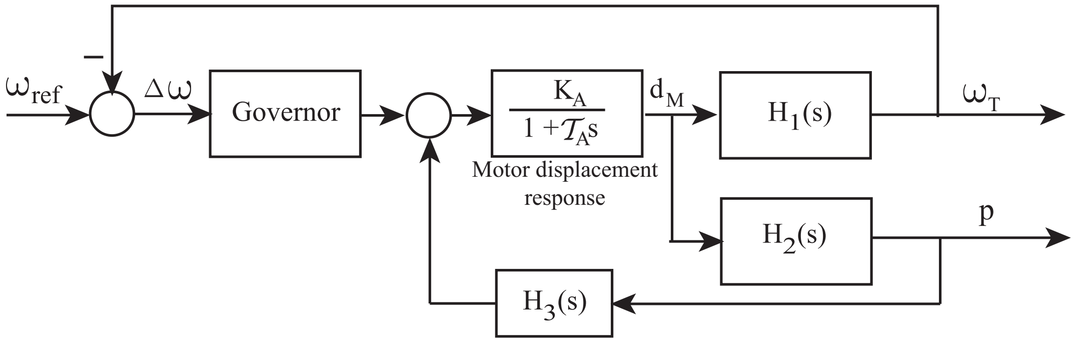

Figure A.4: TSC feedback loop block with damping injection

Combination of equation A.13 and A.14 and elimination of ω_T yields the transfer function $H_2(s)$ from d_M to p:

$$\frac{p}{d_M} = H_2(s) = \frac{K_{\Delta p}(1+\mathcal{T}_{\Delta p}s)}{s^2+2\zeta_2\omega_2 s+\omega_2^2} \tag{A.22}$$

Where

$$K_{\Delta p} = \frac{\Omega_M \beta}{V J_T C_t} \tag{A.23}$$

$$\mathcal{T}_{\Delta p} = \frac{J_T}{C_t} \tag{A.24}$$

$$\omega_2 = \sqrt{\frac{\beta \eta_P D_P^2}{V J_T} K_2} \tag{A.25}$$

$$K_2 = 1 + \frac{C_t C_L}{\eta_P D_P^2} \tag{A.26}$$

$$\zeta_2 = \frac{1}{2 D_P \sqrt{\eta_P K_2}} \left(C_t \sqrt{\frac{V}{\beta J_T}} + C_L \sqrt{\frac{\beta J_T}{V}} \right) \tag{A.27}$$

Equation A.22 has a steady-state term ($H_2(s\!=\!0) = K_{\Delta p}$), which will lead to a change in d_M for constant Δp if this steady state term is not compensated for in $H_3(s)$. The steady state gain can be removed by a high-pass filter, which has a gain of zero for very low frequencies and a gain of one for very high frequencies. A realisation of $H_3(s)$ would then be

$$H_3(s) = K_T \frac{\mathcal{T}_f s}{1 + \mathcal{T}_f s} \tag{A.28}$$

Where K_T is the proportional gain and

$$\frac{\mathcal{T}_f s}{1 + \mathcal{T}_f s} \tag{A.29}$$

is a first-order high-pass filter with time-constant $\mathcal{T}_f$. The high pass filter is necessary because the motor governing should not be affected by the steady-state pressure level.

Frequency response

One of the advantages of working with linear systems is the ability to work with frequency responses for stability analysis. One tool for investigating the stability is the amplitude-phase-frequency (APF) or Bode diagram. The stability analysis is carried out by investigating the gain margin ΔK and phase margin ψ, which are defined at the frequency where the phase margin crosses $-180°$ (ω_{180}) and the amplitude response crosses the zero-dB line (ω_c), as shown in figure A.5. A general rule is that $\Delta K \geq 6\ dB$ and $\psi \gtrsim 30 - 45°$ for stability [6]. These limits are not absolute, however, and the real stability margins may differ from system to system. Note that the x-axis unit is in Hz.

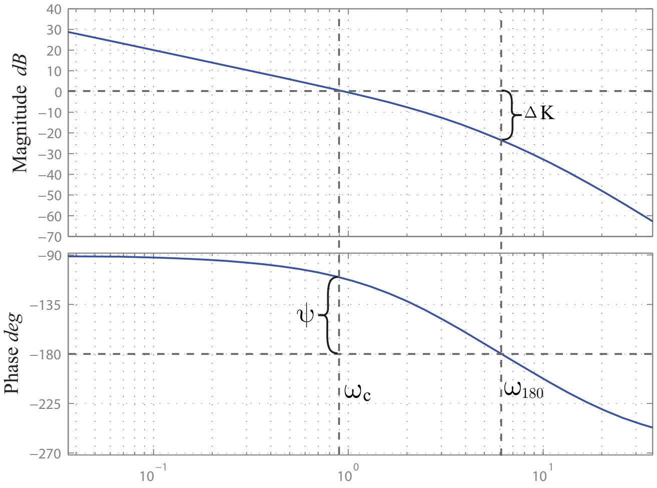

Figure A.5: Bode diagram definitions

Appendix B

Power curves

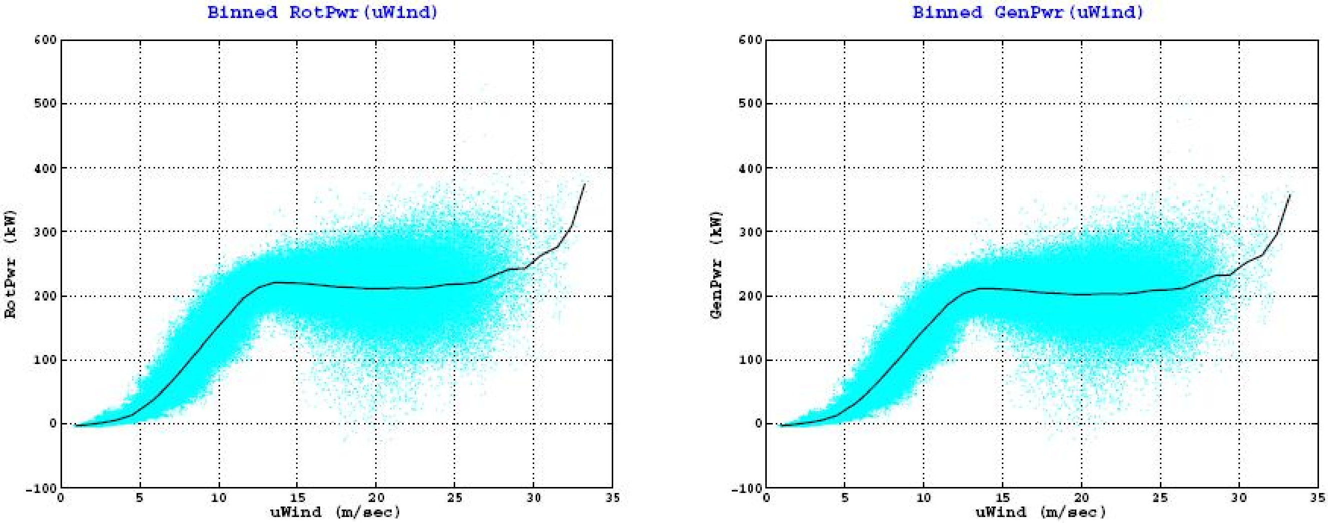

Figure 116: Original V27

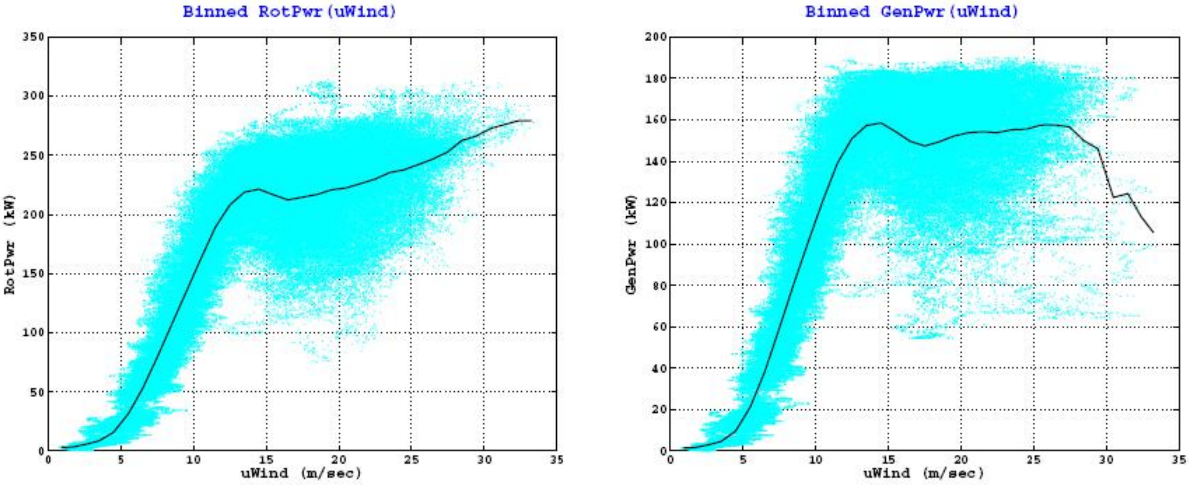

Figure 117: Constant gain

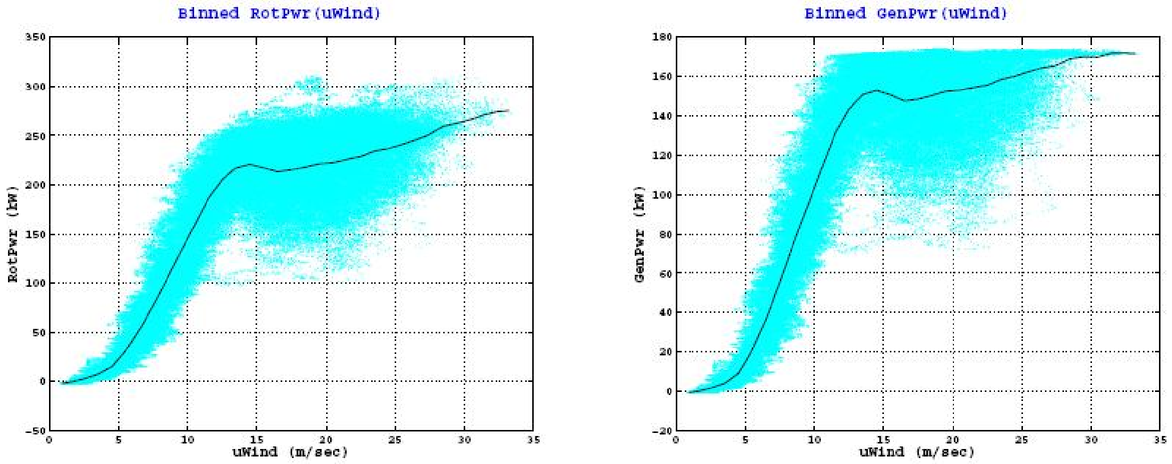

Figure 118: Gearbox subst.

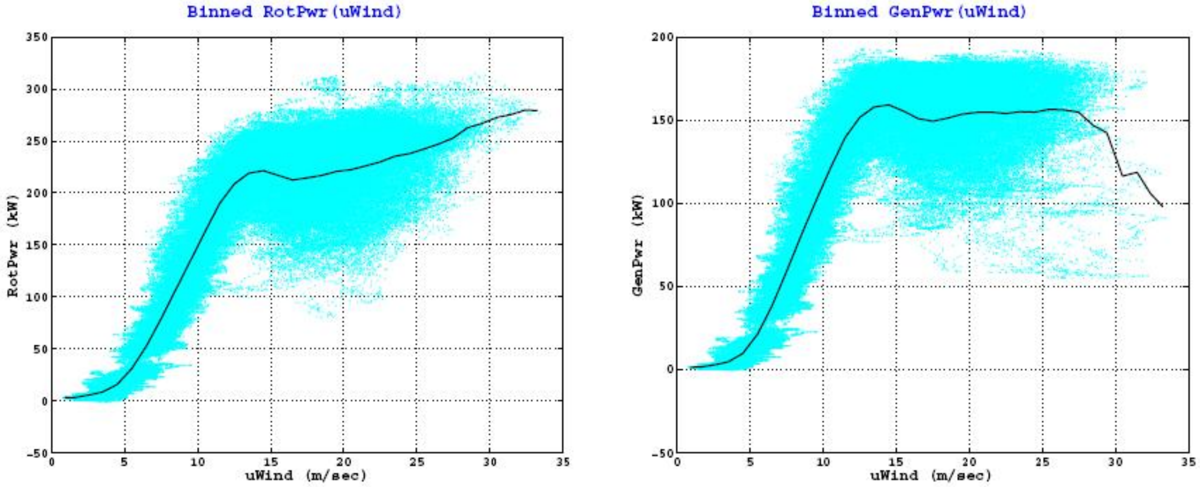

Figure 119: Scheduled gain

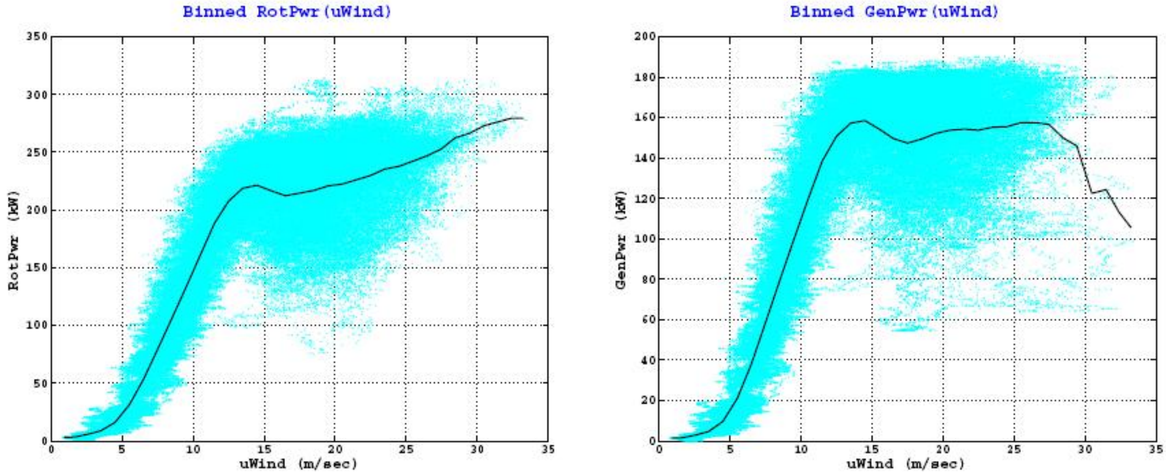

Figure 120: RPPT low Ω_T

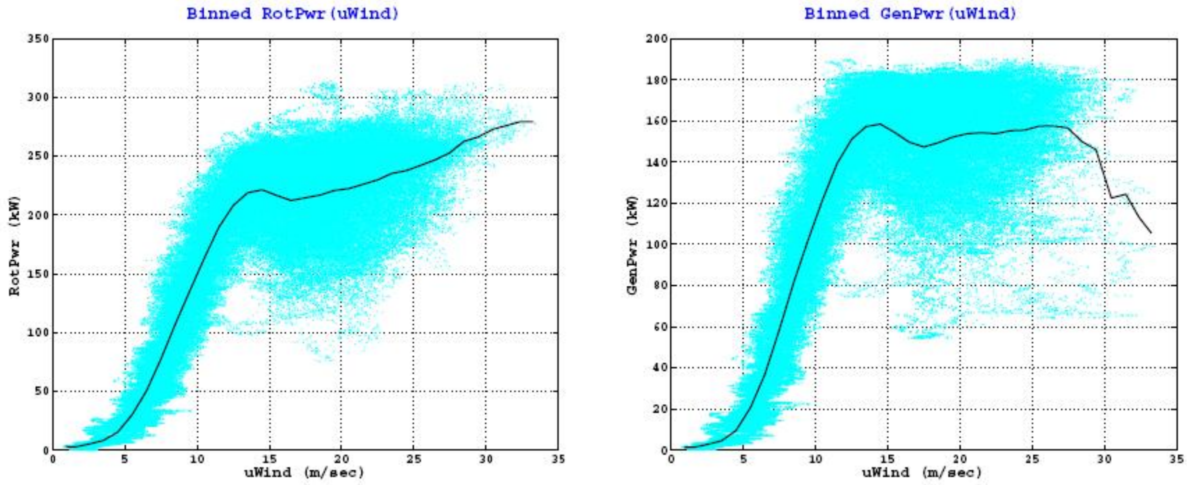

Figure 121: RPPT high Ω_T

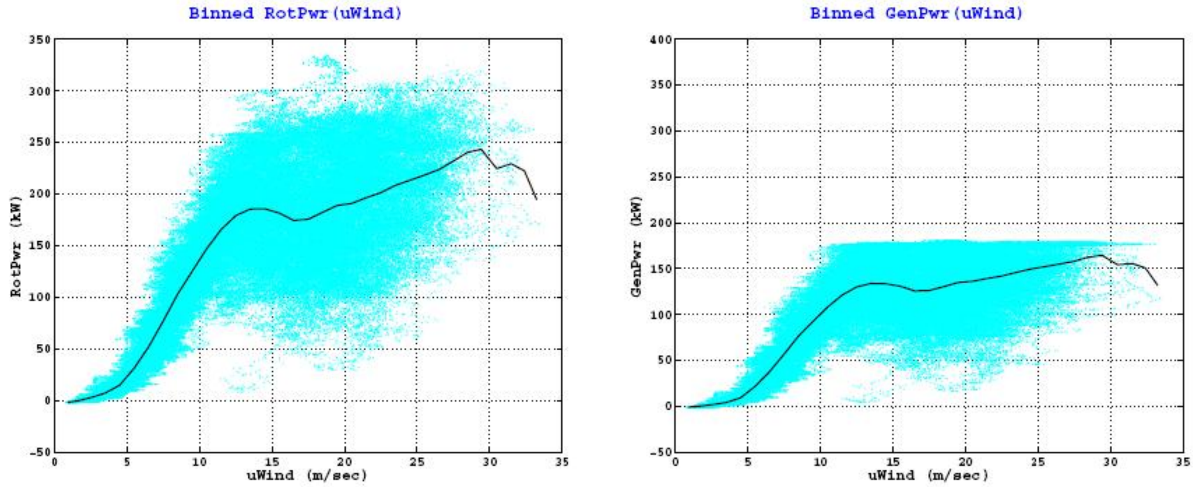

Figure 122: Self governed

Appendix C

Pitch and rotor speed curves

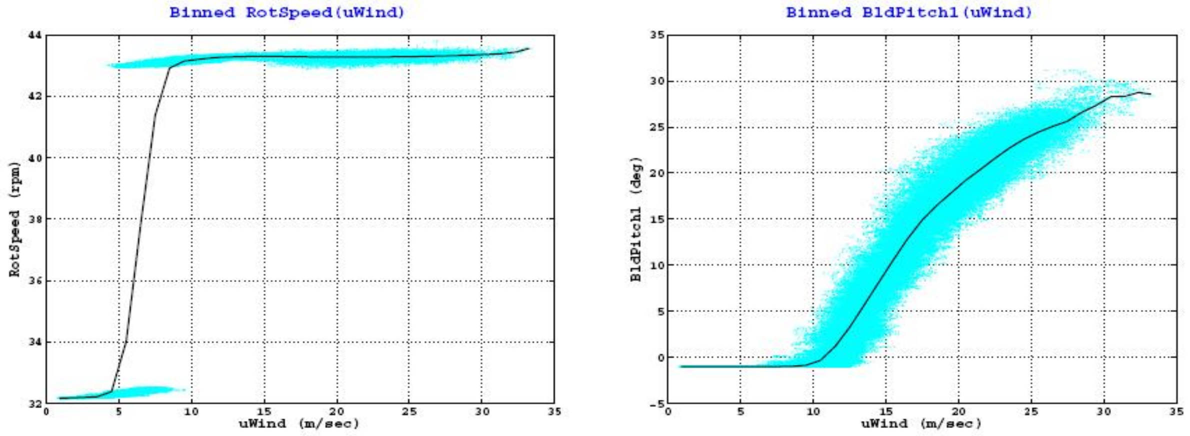

Figure 123: Original V27

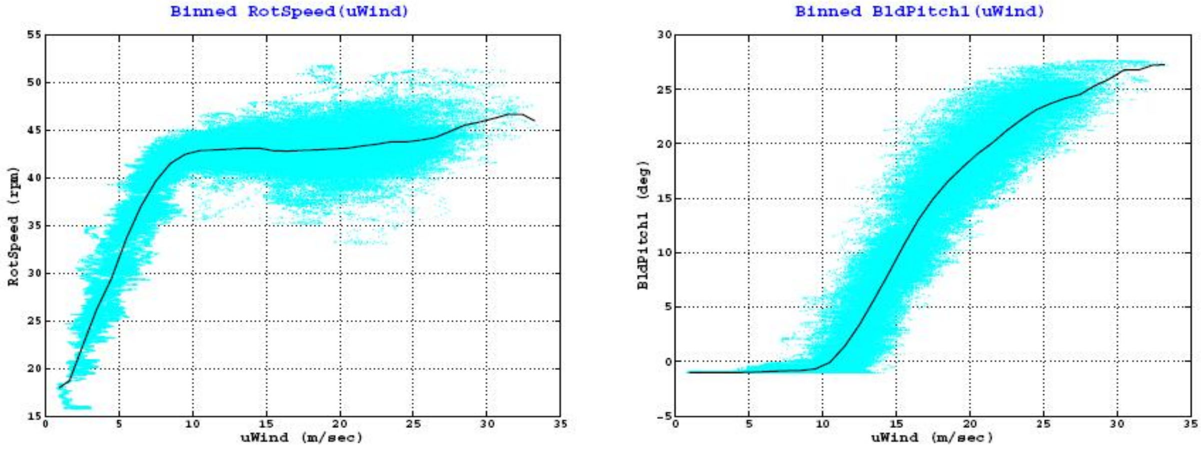

Figure 124: Constant gain

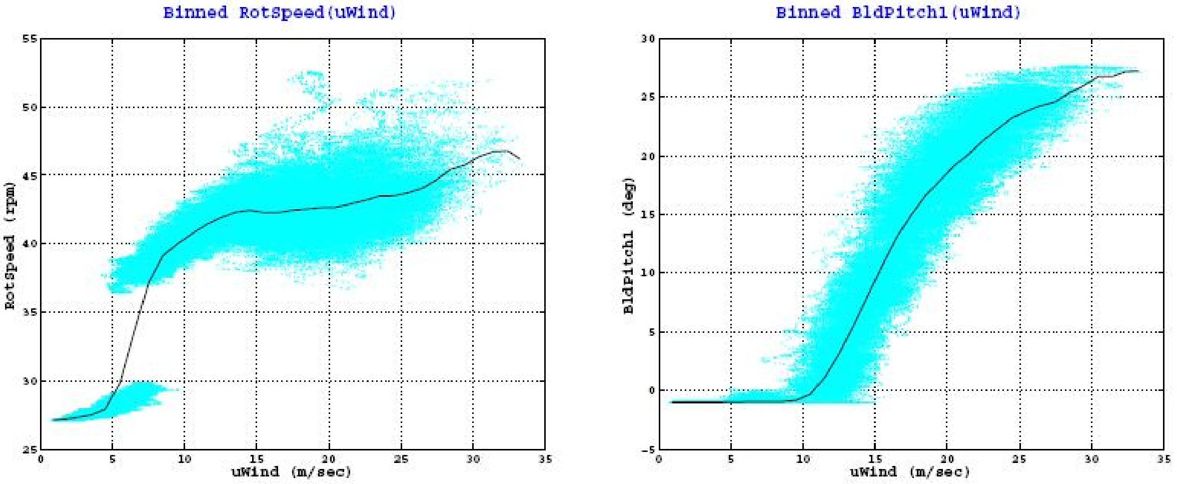

Figure 125: Gearbox subst.

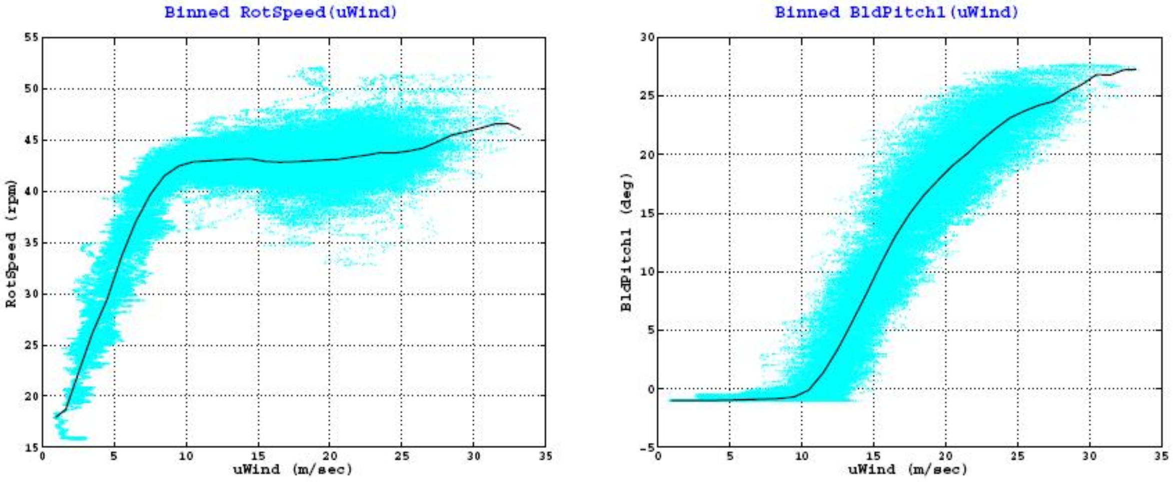

Figure 126: Scheduled gain

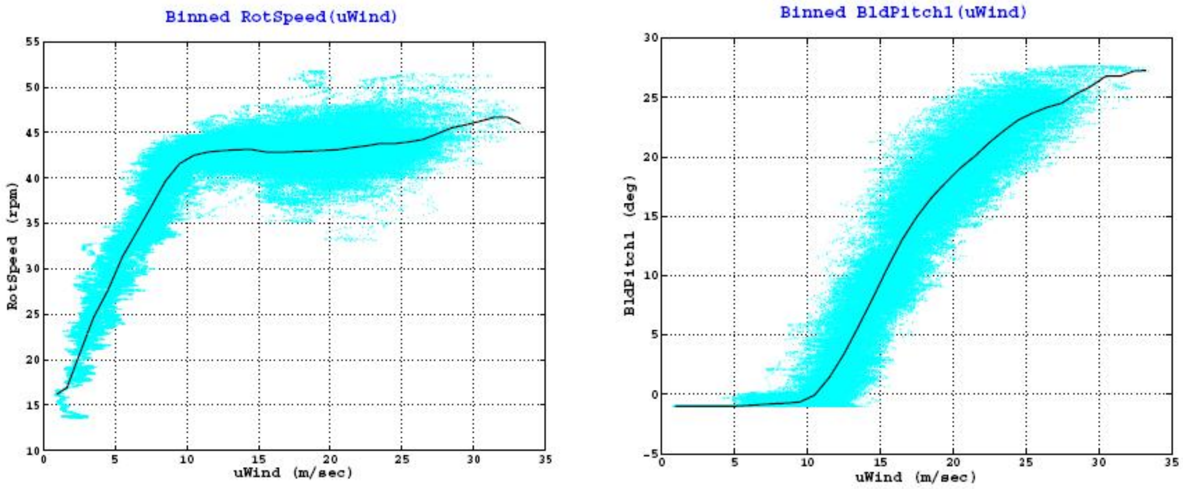

Figure 127: RPPT low Ω_{T}

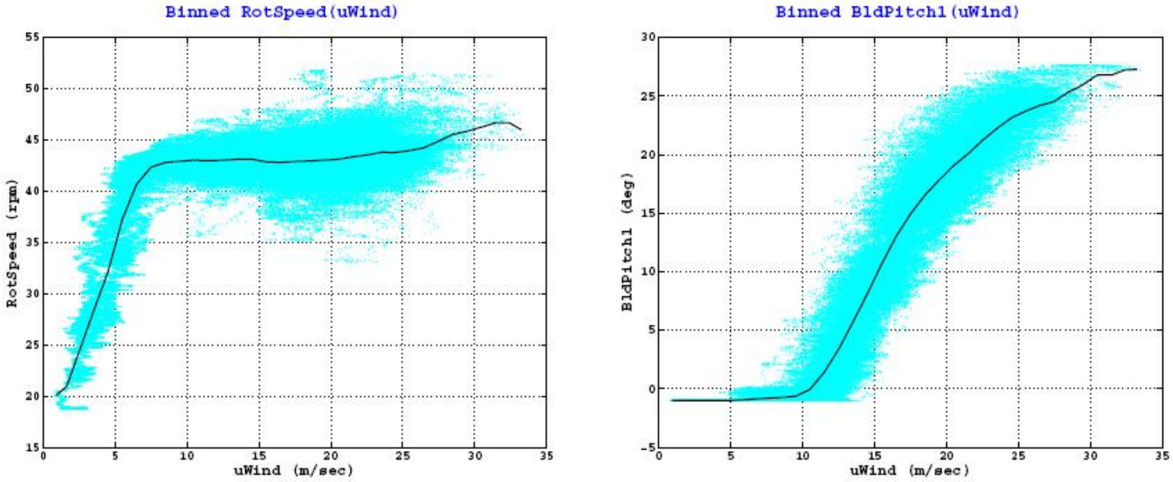

Figure 128: RPPT high Ω_T

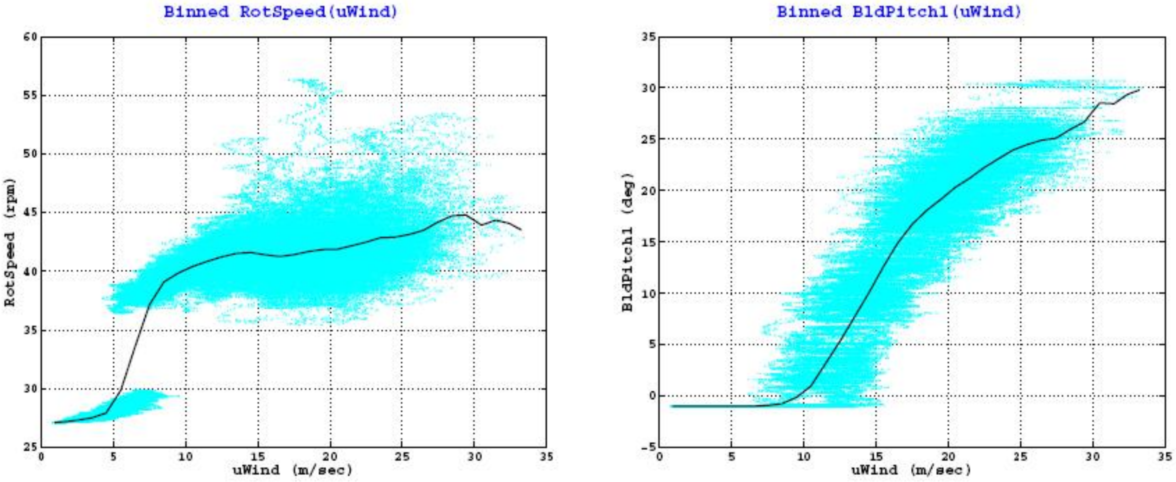

Figure 129: Self governed

Appendix D

Vestas blade data

13 M Rotorblade geometri Red 900419

Profile NACA 63.200 mod. Section

Beam center is placed 32% of cord from leading edge. Webs are displaced 5 mm from edges of the beam.

Bjælkecenter i 32% af korden fra forkant. U-bjælker placeret 5 mm indenfor bjælkekant.

Section	R m	C m	t %	h mm	Beam width m	Blade twist deg.	Trailing edges deflect. mm
62	0.50	0.000	100.00	584			
61	0.60	0.000	100.00	584			
60	0.70	0.000	100.00	574			
59	0.80	0.000	100.00	564			
58	0.90	0.000	0.00	554			
57	1.00	1.366	38.40	544			
56	1.10	1.359	38.02	533			
55	1.20	1.352	37.65	521			
54	1.30	1.344	37.28	510			
53	1.40	1.337	36.91	500			
52	1.50	1.330	36.56	491			
51	1.60	1.323	36.20	482			
50	1.70	1.316	35.86	474			
49	1.80	1.309	35.51	466			
48	1.90	1.301	35.18	458			
47	2.00	1.294	34.84	451	0.50	13.03	34.7
46	2.25	1.276	34.03	434	0.49	12.63	33.2
45	2.50	1.258	33.25	418	0.48	12.22	31.8
44	2.75	1.241	32.49	403	0.47	11.82	30.4
43	3.00	1.223	31.76	388	0.46	11.41	29.1
42	3.25	1.205	31.06	374	0.45	11.01	27.8
41	3.50	1.187	30.37	360	0.44	10.60	26.6
40	3.75	1.169	29.71	347	0.43	10.20	25.4
39	4.00	1.151	29.07	335	0.42	9.79	24.2
38	4.25	1.133	28.44	322	0.41	9.39	23.2
37	4.50	1.115	27.84	310	0.40	8.98	22.1
36	4.75	1.097	27.26	299	0.39	8.58	21.1
35	5.00	1.079	26.69	288	0.38	8.18	20.2
34	5.25	1.061	26.14	277	0.37	7.77	19.2
33	5.50	1.043	25.60	267	0.36	7.37	18.4
32	5.75	1.026	25.08	257	0.35	6.96	17.5
31	6.00	1.008	24.57	248	0.34	6.56	16.7
30	6.25	0.990	24.08	238	0.33	6.15	15.9
29	6.50	0.972	23.60	229	0.32	5.75	15.2
28	6.75	0.954	23.14	221	0.31	5.34	14.4
27	7.00	0.936	22.68	212	0.30	4.97	13.7
26	7.25	0.918	22.24	204	0.29	4.62	13.1
25	7.50	0.900	21.81	196	0.28	4.29	12.4
24	7.75	0.882	21.39	189	0.27	3.98	11.8
23	8.00	0.864	20.98	181	0.26	3.69	11.2
22	8.25	0.846	20.58	174	0.25	3.42	10.6
21	8.50	0.828	20.19	167	0.24	3.16	10.1
20	8.75	0.810	19.81	161	0.23	2.92	9.6
19	9.00	0.793	19.44	154	0.22	2.69	9.1
18	9.25	0.775	19.08	148	0.21	2.47	8.6
17	9.50	0.757	18.72	142	0.20	2.27	8.1
16	9.75	0.739	18.38	136	0.19	2.07	7.7
15	10.00	0.721	18.04	130	0.18	1.89	7.2
14	10.25	0.703	17.71	124	0.17	1.71	6.8
13	10.50	0.685	17.38	119	0.16	1.54	6.4
12	10.75	0.667	17.07	114	0.15	1.38	6.0
11	11.00	0.649	16.76	109	0.14	1.23	5.7
10	11.25	0.631	16.46	104	0.13	1.08	5.3
9	11.50	0.613	16.16	99	0.12	0.94	5.0
8	11.75	0.595	15.87	94	0.11	0.80	4.7
7	12.00	0.578	15.59	90	0.10	0.68	4.4
6	12.25	0.560	15.31	86		0.55	4.1
5	12.50	0.542	15.04	81		0.43	3.8
4	12.75	0.524	14.77	77		0.32	3.5
3	13.00	0.506	14.51	73		0.21	3.3
2	13.25	0.488	14.25	70		0.10	3.1
1	13.50	0.470	14.00	66		0.00	2.8

Mass distributation

Shell weight pr m2 10 kg/m2
Beam weight pr m2 2.2 kg/m2 pr mm thickness incl. web.

Radius m	Shell kg	Beam kg		Massemoment Nm	Inertia kgm2
0			0.0	28948	22302
0.4		60	60.0	25351	
1	27.3	41.8	69.1	22947	
2	25.9	41.1	67.0	18941	
3	24.5	37.8	62.3	14935	
4	23.0	33.5	56.6	11541	
5	21.6	29.4	51.0	8703	
6	20.2	25.5	45.7	6365	
7	18.7	21.8	40.5	4475	
8	17.3	18.9	36.2	2984	
9	15.9	16.0	31.8	1847	
10	14.4	13.1	27.5	1023	
11	13.0	10.2	23.1	469	
12	11.6	7.3	18.8	142	
13	10.1	4.4	14.5	36	
Sumweight	243	361	total =	604 kg	

Bladedeflection and curvature

R	Ix-x m^4	Mx Nm	r m	1/r /m	angle rad	sum rad	deflect m
1	9.37E-04	1.63E+05	1.73E+02	0.006	0.006	0.006	0.003
2	8.06E-04	1.34E+05	1.81E+02	0.006	0.006	0.011321	0.011
3	5.37E-04	1.08E+05	1.49E+02	0.007	0.007	0.018015	0.026
4	3.44E-04	8.53E+04	1.21E+02	0.008	0.008	0.026275	0.048
5	2.17E-04	6.60E+04	9.89E+01	0.010	0.010	0.036383	0.080
6	1.35E-04	4.95E+04	8.15E+01	0.012	0.012	0.048645	0.122
7	8.12E-05	3.58E+04	6.79E+01	0.015	0.015	0.063362	0.178
8	4.87E-05	2.47E+04	5.92E+01	0.017	0.017	0.080264	0.250
9	2.79E-05	1.59E+04	5.28E+01	0.019	0.019	0.099216	0.339
10	1.51E-05	9.20E+03	4.91E+01	0.020	0.020	0.119571	0.449
11	7.50E-06	4.49E+03	5.01E+01	0.020	0.020	0.139539	0.578
12	3.33E-06	1.54E+03	6.47E+01	0.015	0.015	0.154986	0.725
13	6.06E-07	1.64E+02	1.11E+02	0.009	0.009	0.164025	0.883
					Tipdeflection:		0.883

Material stress and strain

R m	M Nm	C m	Ix-x m^4	Smax m	Wx-x m^3	stress Pa	strain m/m (E=30GPa
1	1.63E+05	1.366	9.37E-04	2.62E-01	3.57E-03	4.56E+07	0.0015
2	1.34E+05	1.29432	8.06E-04	2.26E-01	3.57E-03	3.74E+07	0.0012
3	1.08E+05	1.22264	5.37E-04	1.94E-01	2.76E-03	3.90E+07	0.0013
4	8.53E+04	1.15096	3.44E-04	1.67E-01	2.06E-03	4.14E+07	0.0014
5	6.60E+04	1.07928	2.17E-04	1.44E-01	1.51E-03	4.37E+07	0.0015
6	4.95E+04	1.0076	1.35E-04	1.24E-01	1.09E-03	4.55E+07	0.0015
7	3.58E+04	0.93592	8.12E-05	1.06E-01	7.65E-04	4.69E+07	0.0016
8	2.47E+04	0.86424	4.87E-05	9.07E-02	5.37E-04	4.60E+07	0.0015
9	1.59E+04	0.79256	2.79E-05	7.70E-02	3.62E-04	4.38E+07	0.0015
10	9.20E+03	0.72088	1.51E-05	6.50E-02	2.32E-04	3.97E+07	0.0013
11	4.49E+03	0.6492	7.50E-06	5.44E-02	1.38E-04	3.26E+07	0.0011
12	1.54E+03	0.57752	3.33E-06	4.50E-02	7.41E-05	2.09E+07	0.0007
13	1.64E+02	0.50584	6.06E-07	3.67E-02	1.65E-05	9.95E+06	0.0003

Appendix E

XFOIL input parameters

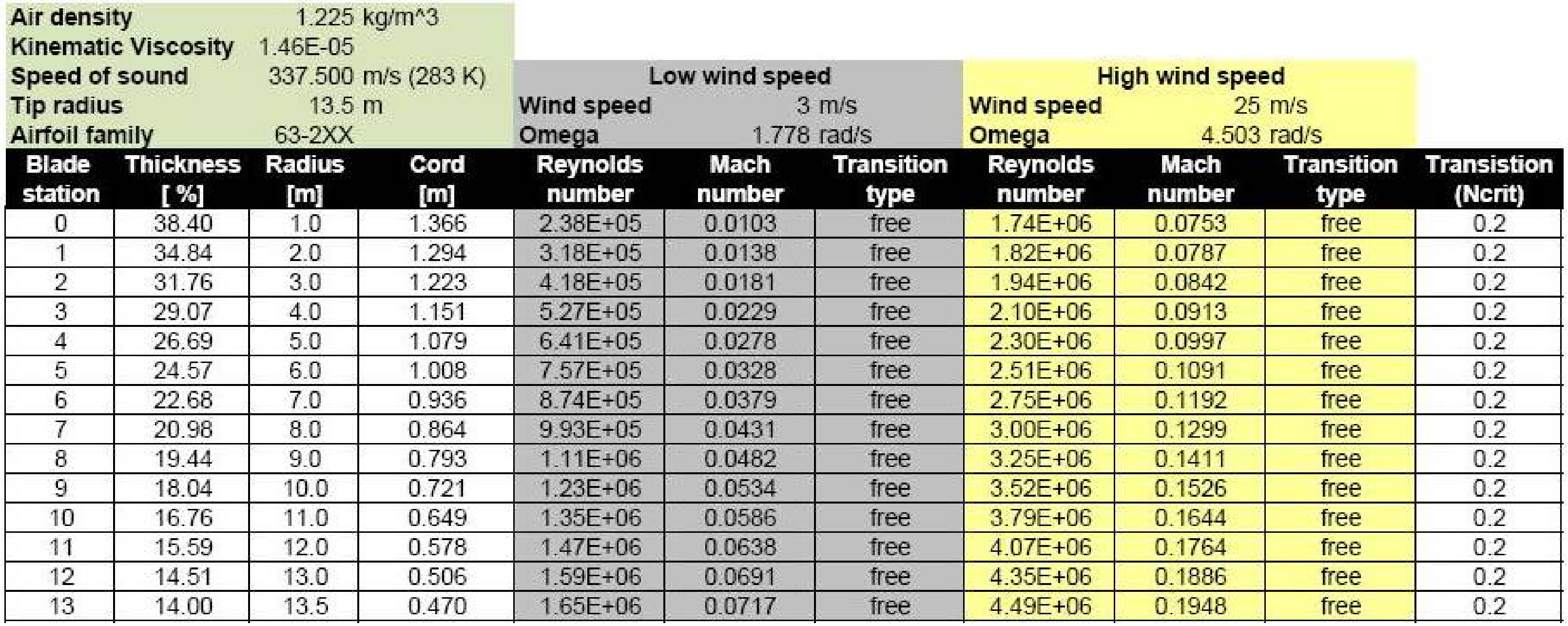

Air density 1.225 kg/m^3
Kinematic Viscosity 1.46E-05
Speed of sound 337.500 m/s (283 K)
Tip radius 13.5 m
Airfoil family 63-2XX

				Low wind speed Wind speed 3 m/s Omega 1.778 rad/s			High wind speed Wind speed 25 m/s Omega 4.503 rad/s			
Blade station	**Thickness [%]**	**Radius [m]**	**Cord [m]**	**Reynolds number**	**Mach number**	**Transition type**	**Reynolds number**	**Mach number**	**Transition type**	**Transistion (Ncrit)**
0	38.40	1.0	1.366	2.38E+05	0.0103	free	1.74E+06	0.0753	free	0.2
1	34.84	2.0	1.294	3.18E+05	0.0138	free	1.82E+06	0.0787	free	0.2
2	31.76	3.0	1.223	4.18E+05	0.0181	free	1.94E+06	0.0842	free	0.2
3	29.07	4.0	1.151	5.27E+05	0.0229	free	2.10E+06	0.0913	free	0.2
4	26.69	5.0	1.079	6.41E+05	0.0278	free	2.30E+06	0.0997	free	0.2
5	24.57	6.0	1.008	7.57E+05	0.0328	free	2.51E+06	0.1091	free	0.2
6	22.68	7.0	0.936	8.74E+05	0.0379	free	2.75E+06	0.1192	free	0.2
7	20.98	8.0	0.864	9.93E+05	0.0431	free	3.00E+06	0.1299	free	0.2
8	19.44	9.0	0.793	1.11E+06	0.0482	free	3.25E+06	0.1411	free	0.2
9	18.04	10.0	0.721	1.23E+06	0.0534	free	3.52E+06	0.1526	free	0.2
10	16.76	11.0	0.649	1.35E+06	0.0586	free	3.79E+06	0.1644	free	0.2
11	15.59	12.0	0.578	1.47E+06	0.0638	free	4.07E+06	0.1764	free	0.2
12	14.51	13.0	0.506	1.59E+06	0.0691	free	4.35E+06	0.1886	free	0.2
13	14.00	13.5	0.470	1.65E+06	0.0717	free	4.49E+06	0.1948	free	0.2

Appendix F

Simulink block diagram

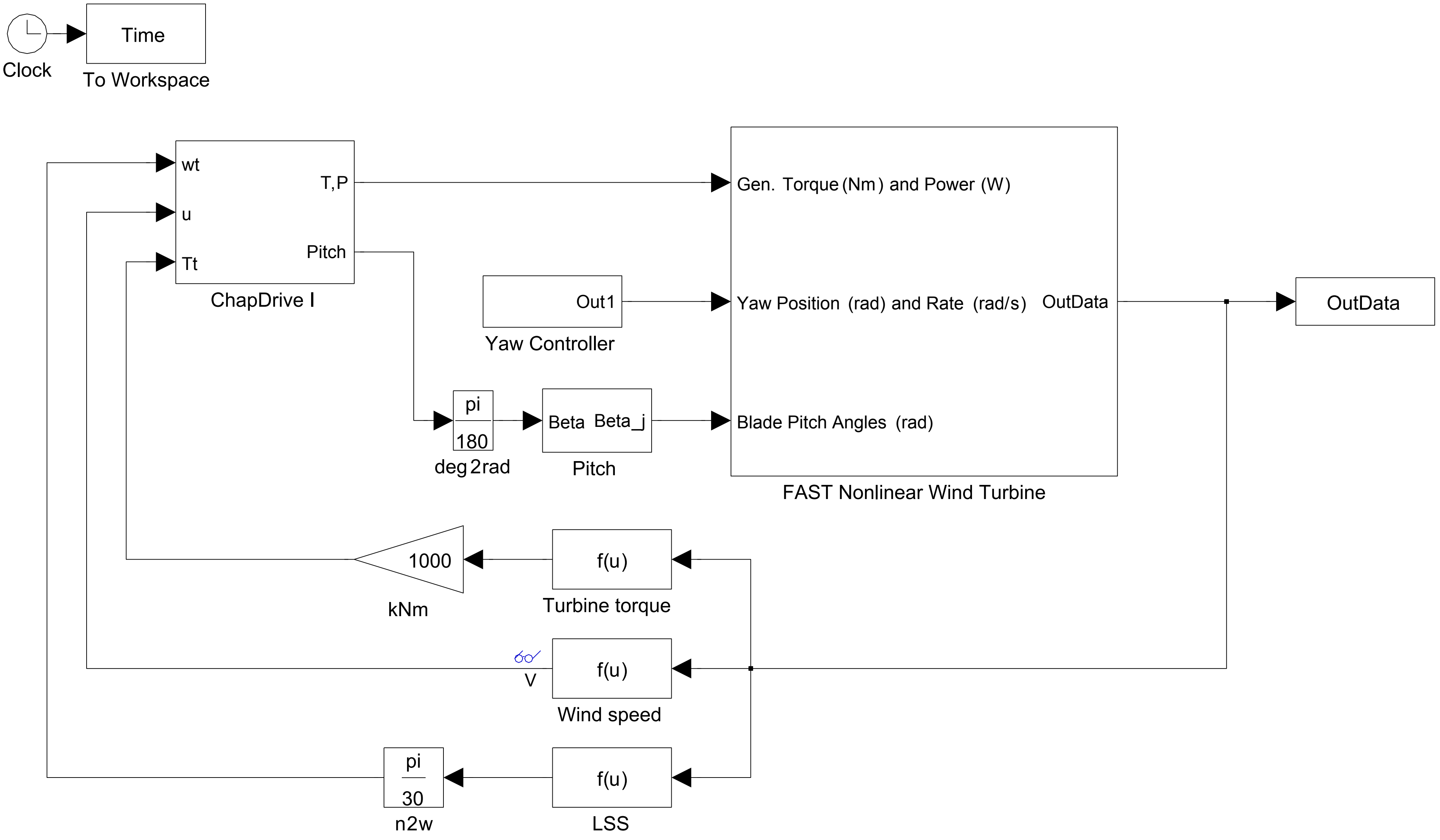
Time
Clock
To Workspace
wt
u
Tt
T,P
Pitch
ChapDrive I
Gen. Torque (Nm) and Power (W)
Yaw Position (rad) and Rate (rad/s)
Blade Pitch Angles (rad)
OutData
FAST Nonlinear Wind Turbine
Out1
Yaw Controller
pi
180
deg2rad
Beta Beta_j
Pitch
OutData
1000
kNm
f(u)
Turbine torque
V
f(u)
Wind speed
pi
30
n2w
f(u)
LSS

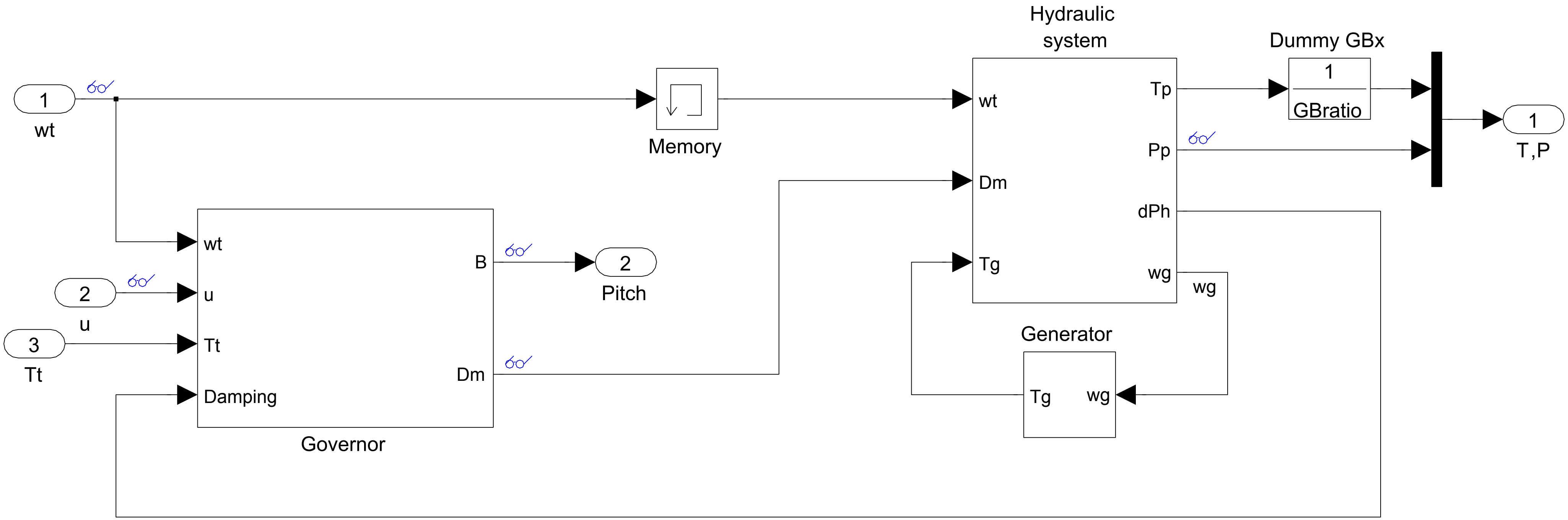
1
wt
Memory
Hydraulic system
wt
Dm
Tg
Tp
Pp
dPh
wg
wg
Dummy GBx
1
GBratio
1
T,P
wt
u
Tt
Damping
B
Dm
Governor
2
u
3
Tt
2
Pitch
Generator
Tg
wg

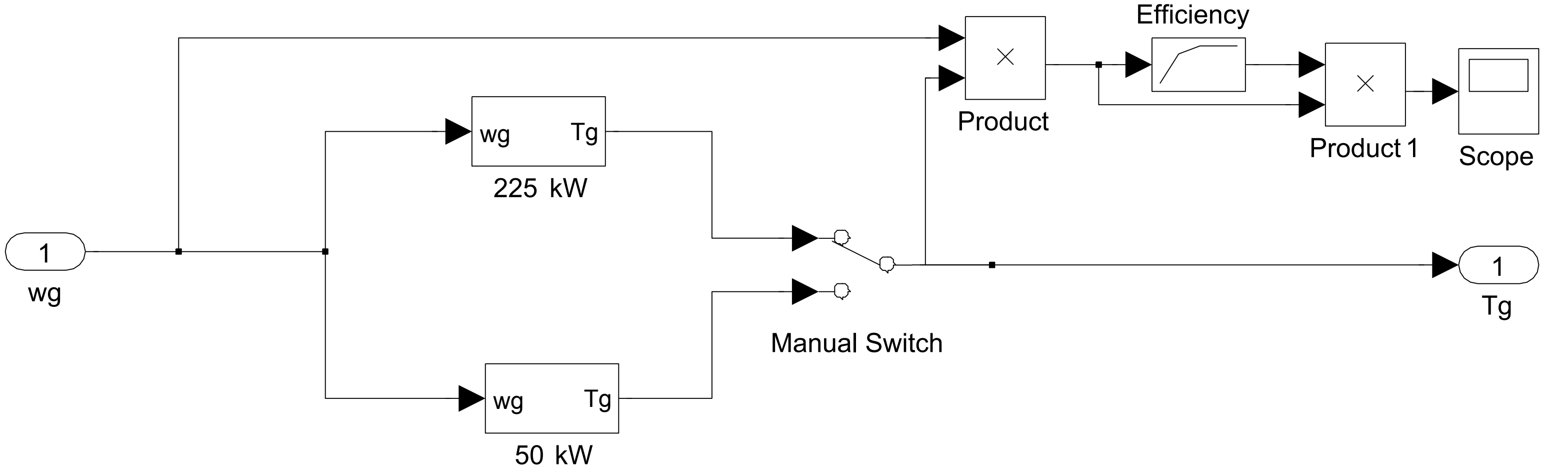
Efficiency
Product
Product 1
Scope
wg
Tg
225 kW
wg
Tg
50 kW
Manual Switch
1
wg
1
Tg

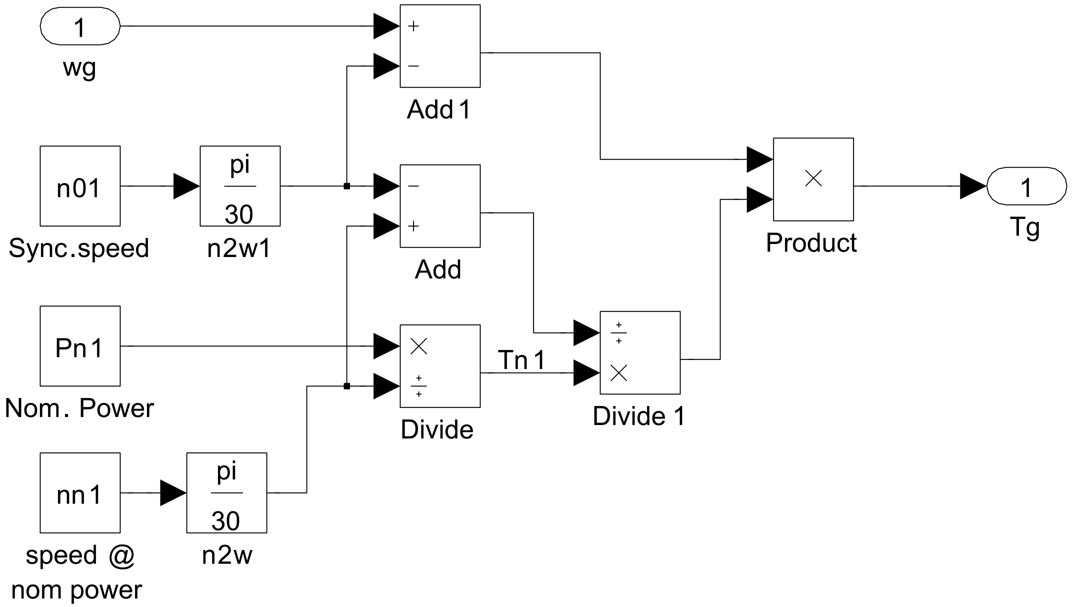
1
wg
+
−
Add 1
n01
Sync.speed
pi
30
n2w1
−
+
Add
Product
1
Tg
Pn1
Nom. Power
Divide
Tn1
Divide 1
nn1
speed @
nom power
pi
30
n2w

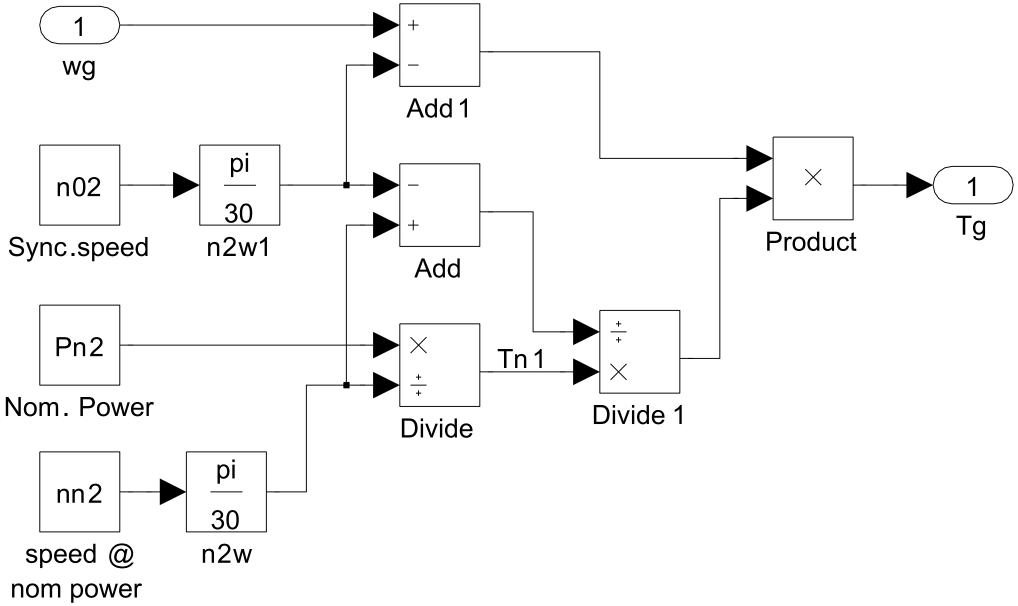
1
wg
Add 1
n02
Sync.speed
pi
30
n2w1
Add
Pn2
Nom. Power
Divide
Tn 1
Divide 1
nn2
speed @
nom power
pi
30
n2w
Product
1
Tg

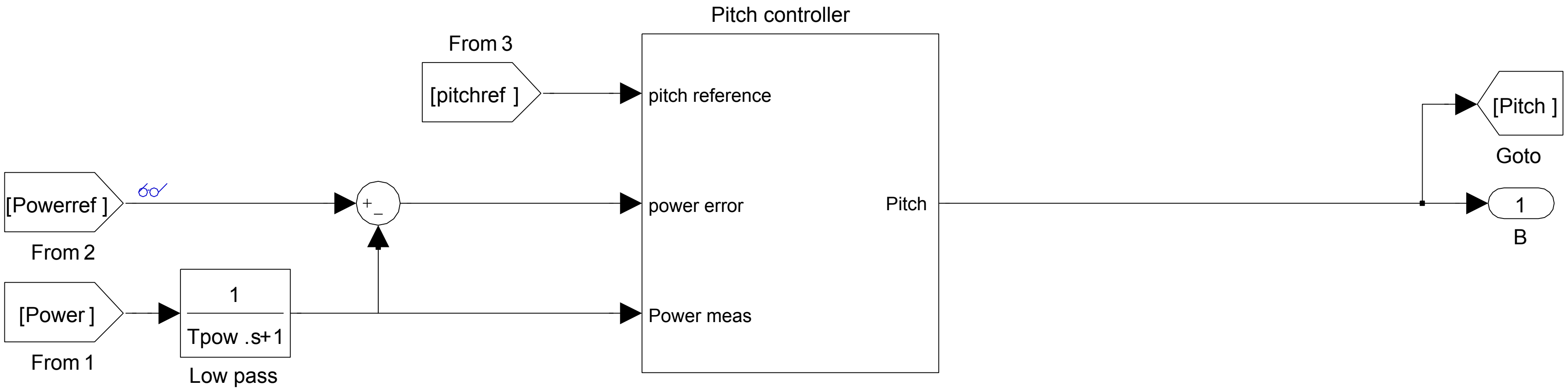
Pitch controller
From 3
[pitchref]
pitch reference
[Powerref]
From 2
+
_
power error
Pitch
[Power]
From 1
1
Tpow .s+1
Low pass
Power meas
[Pitch]
Goto
1
B

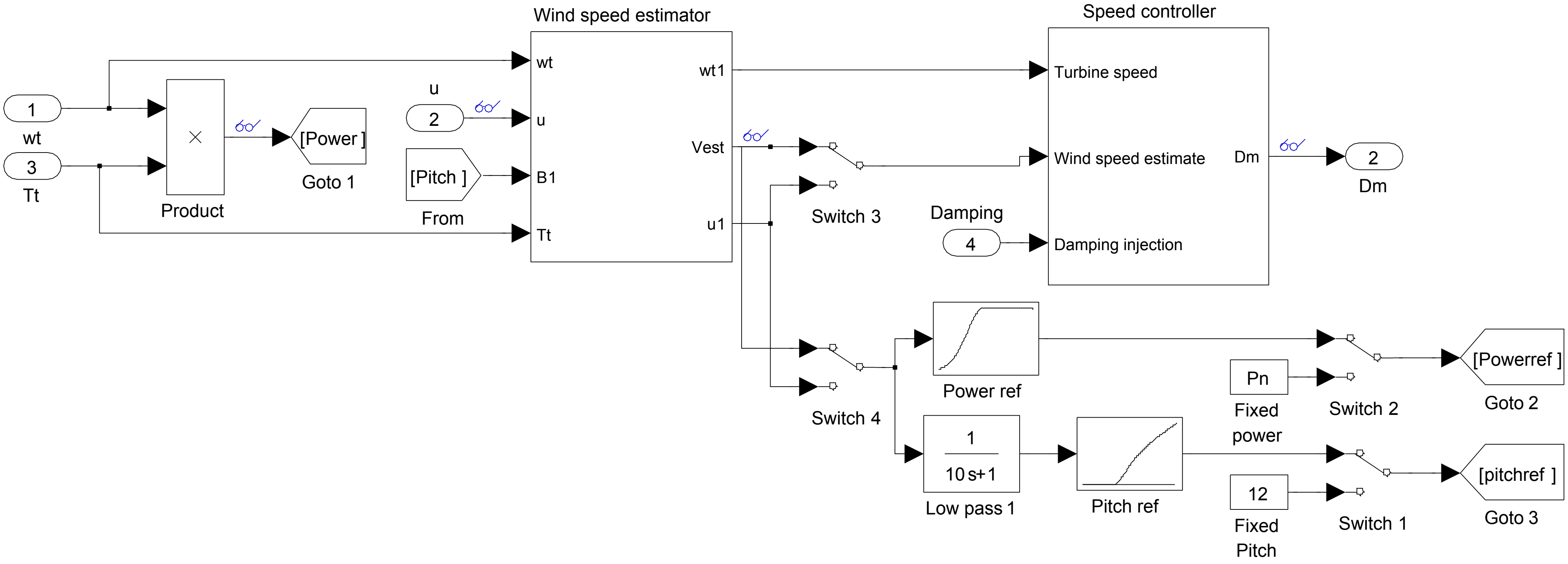
Wind speed estimator
wt
wt1
1
wt
3
Tt
×
Product
[Power]
Goto 1
u
2
u
[Pitch]
From
B1
Tt
Vest
u1
Switch 3
Speed controller
Turbine speed
Wind speed estimate
Dm
Damping
4
Damping injection
2
Dm
Switch 4
Power ref
Pn
Fixed power
Switch 2
[Powerref]
Goto 2
1
10 s+1
Low pass 1
Pitch ref
12
Fixed Pitch
Switch 1
[pitchref]
Goto 3

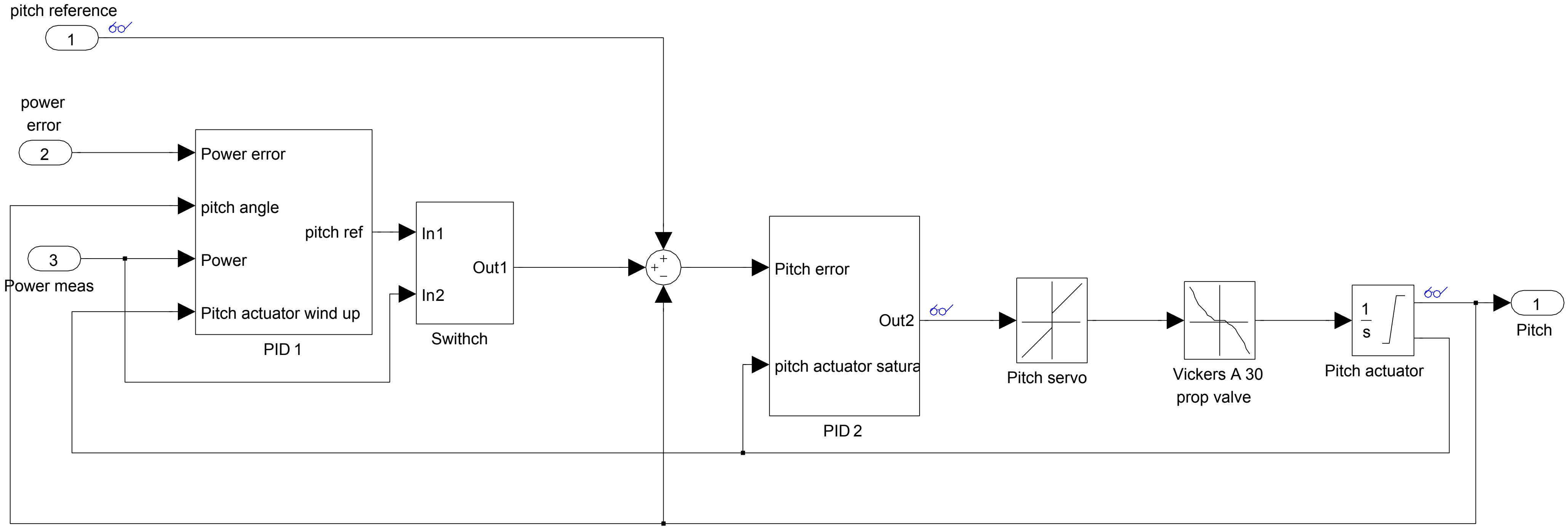
pitch reference
1
power
error
2
Power error
pitch angle
pitch ref
3
Power
Power meas
Pitch actuator wind up
PID 1
In1
Out1
In2
Swithch
+
+
-
Pitch error
Out2
pitch actuator satura
PID 2
Pitch servo
Vickers A 30
prop valve
1
s
Pitch actuator
1
Pitch

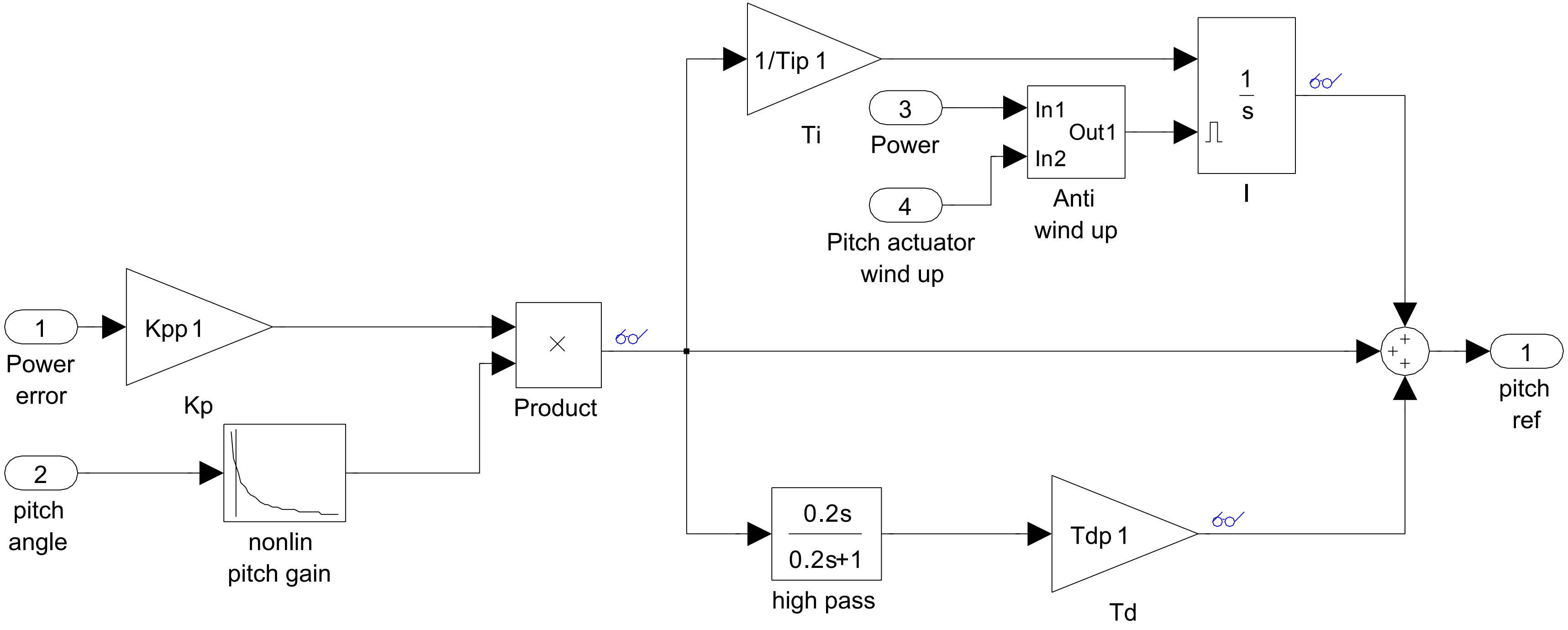
1/Tip 1
Ti
3
Power
In1
In2
Out1
Anti
wind up
1
s
I
4
Pitch actuator
wind up
1
Power
error
Kpp 1
Kp
Product
2
pitch
angle
nonlin
pitch gain
+
+
+
1
pitch
ref
0.2s
0.2s+1
high pass
Tdp 1
Td

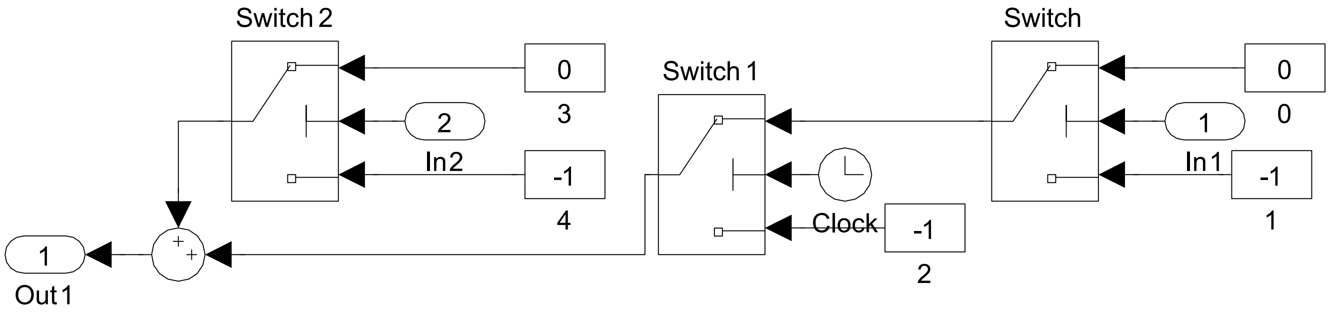
Switch 2
Switch 1
Switch
0
3
2
In2
-1
4
Clock
-1
2
0
0
1
In1
-1
1
1
Out1
+
+

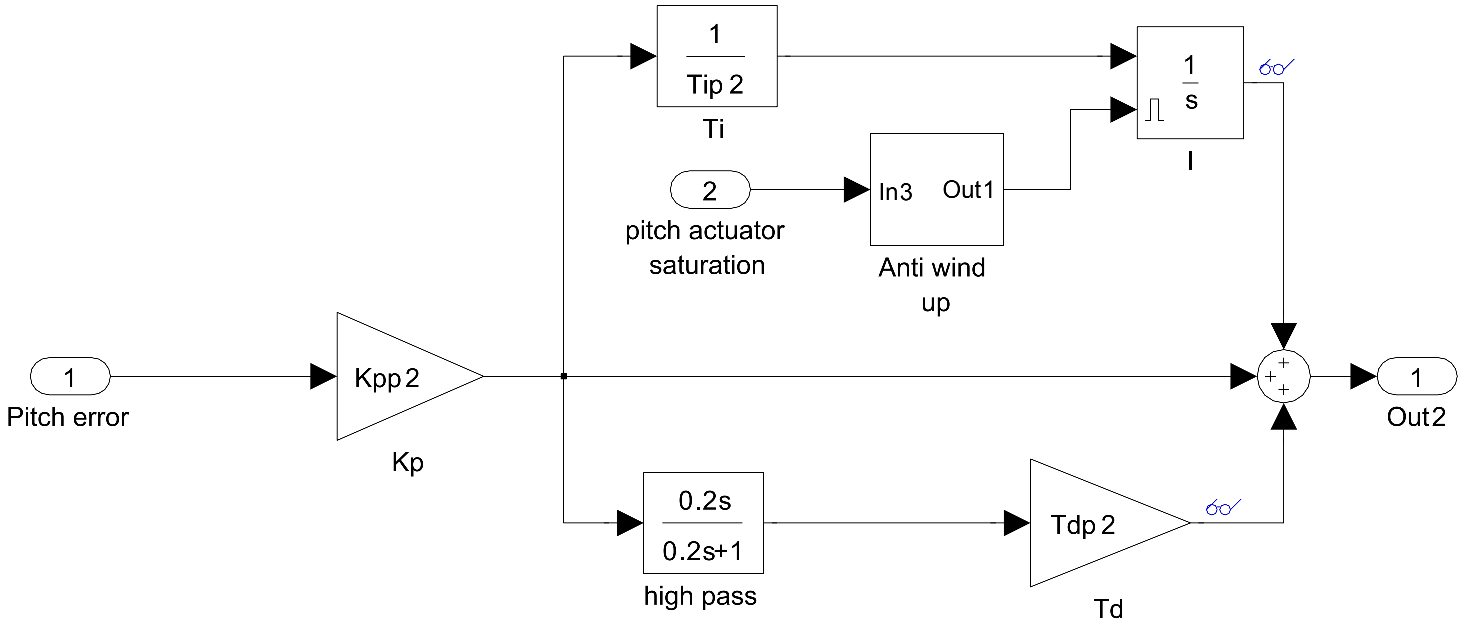
1
Pitch error
Kpp2
Kp
1
Tip 2
Ti
2
pitch actuator saturation
In3
Out1
Anti wind up
1
s
I
0.2s
0.2s+1
high pass
Tdp2
Td
+
+
+
1
Out2

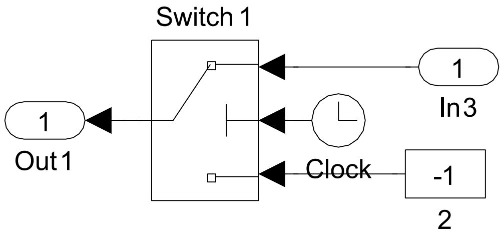
Switch 1
1
In3
1
Out 1
Clock
-1
2

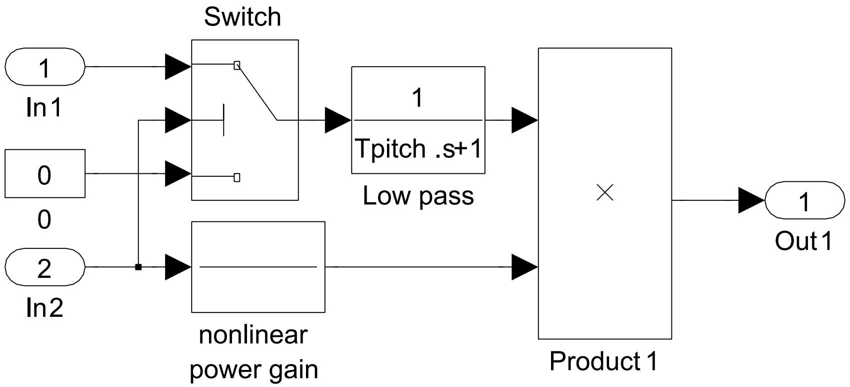
Switch
1
In1
0
0
2
In2
1
Tpitch .s+1
Low pass
nonlinear
power gain
×
Product 1
1
Out1

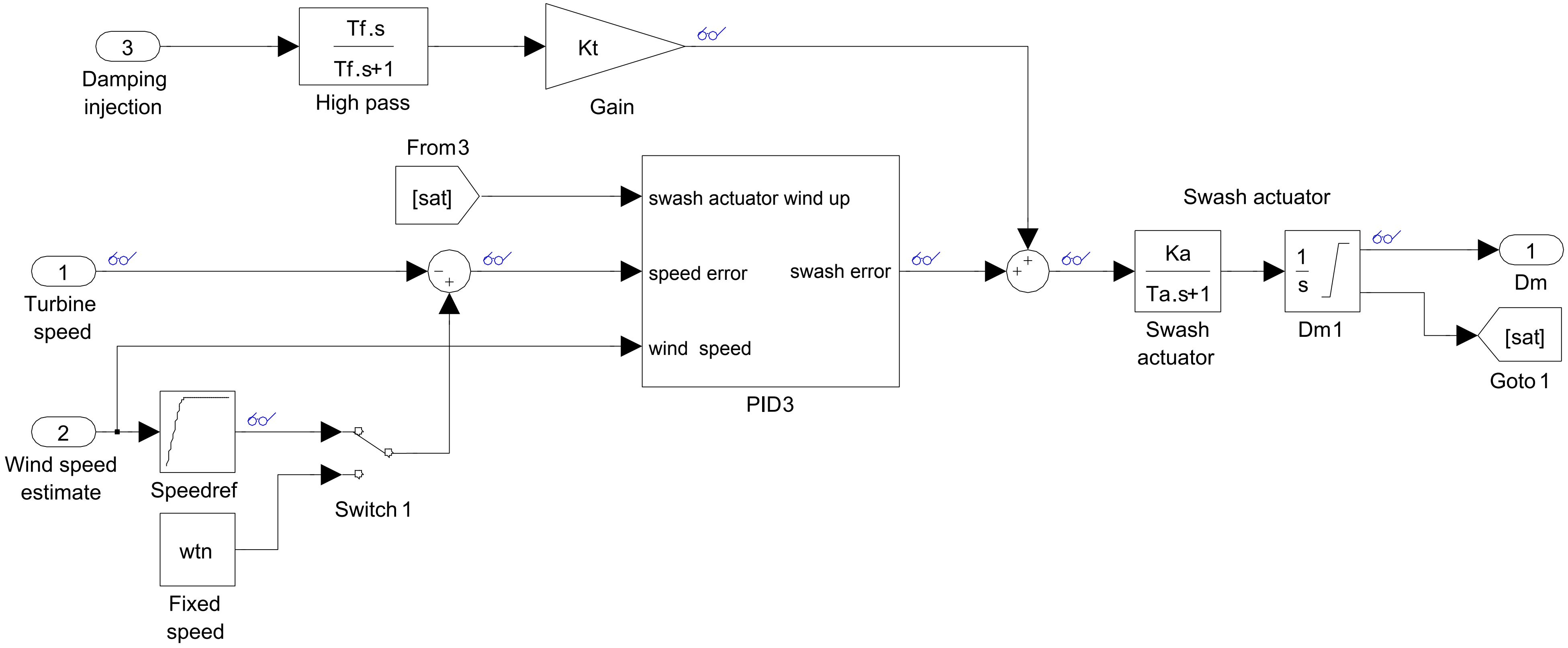
3
Damping injection
Tf.s
Tf.s+1
High pass
Kt
Gain
From3
[sat]
swash actuator wind up
speed error
swash error
wind speed
PID3
1
Turbine speed
2
Wind speed estimate
Speedref
wtn
Fixed speed
Switch 1
Swash actuator
Ka
Ta.s+1
Swash actuator
1
s
Dm1
1
Dm
[sat]
Goto 1

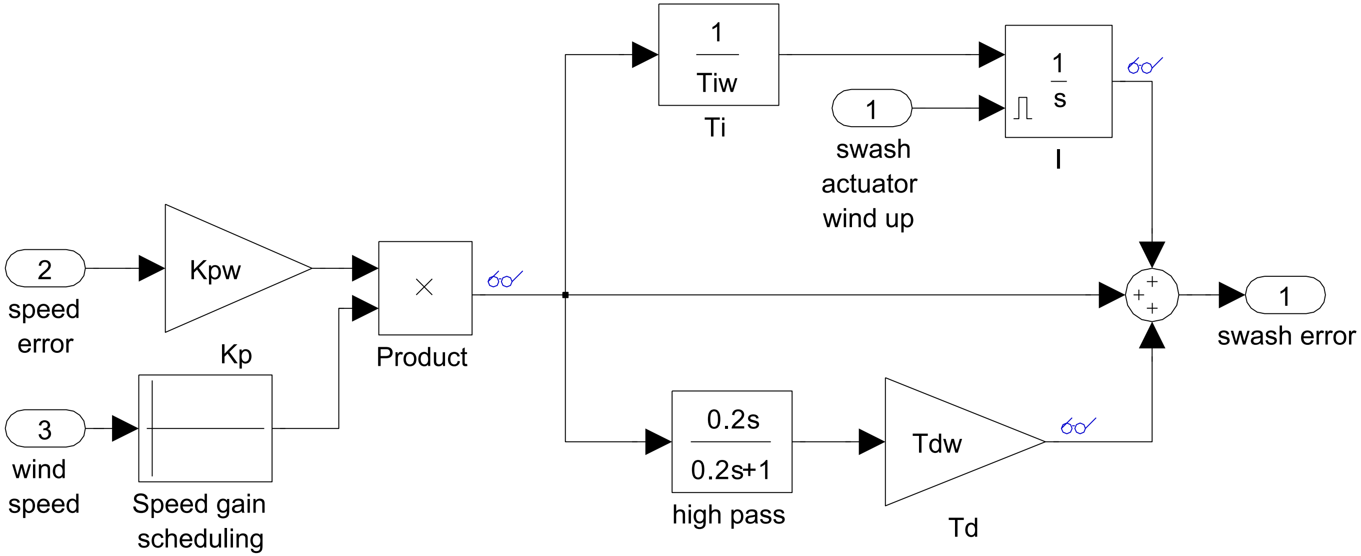
2
speed error
Kpw
Kp
3
wind speed
Speed gain scheduling
Product
1
Tiw
Ti
1
swash actuator wind up
1
s
I
0.2s
0.2s+1
high pass
Tdw
Td
1
swash error

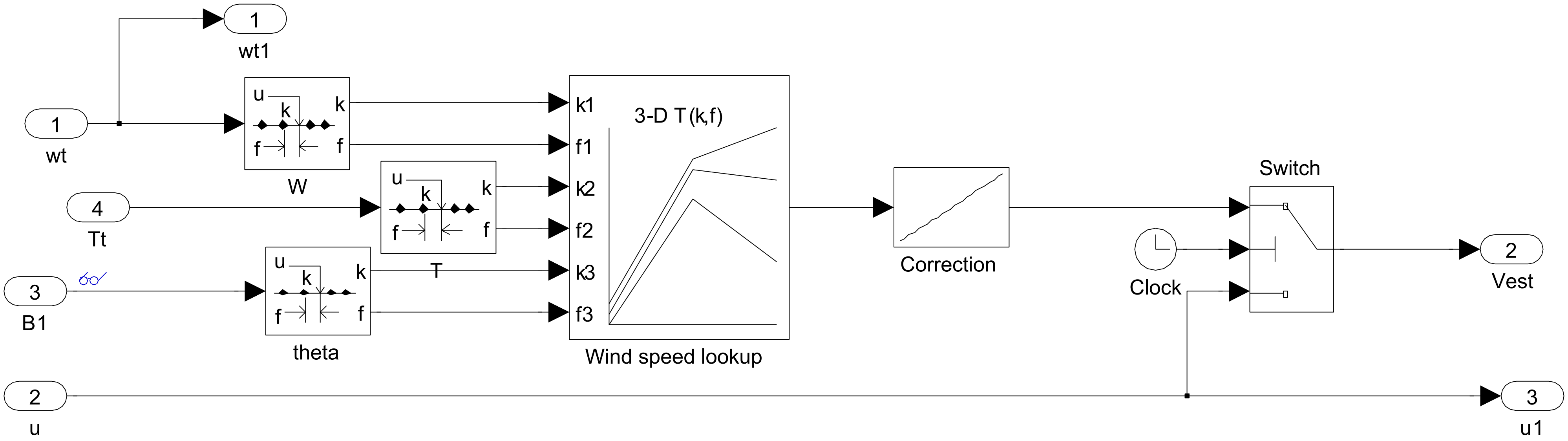
1
wt1
1
wt
u
k
k
f
f
W
4
Tt
u
k
k
f
f
T
3
B1
u
k
k
f
f
theta
k1
f1
k2
f2
k3
f3
3-D T(k,f)
Wind speed lookup
Correction
Switch
Clock
2
Vest
2
u
3
u1

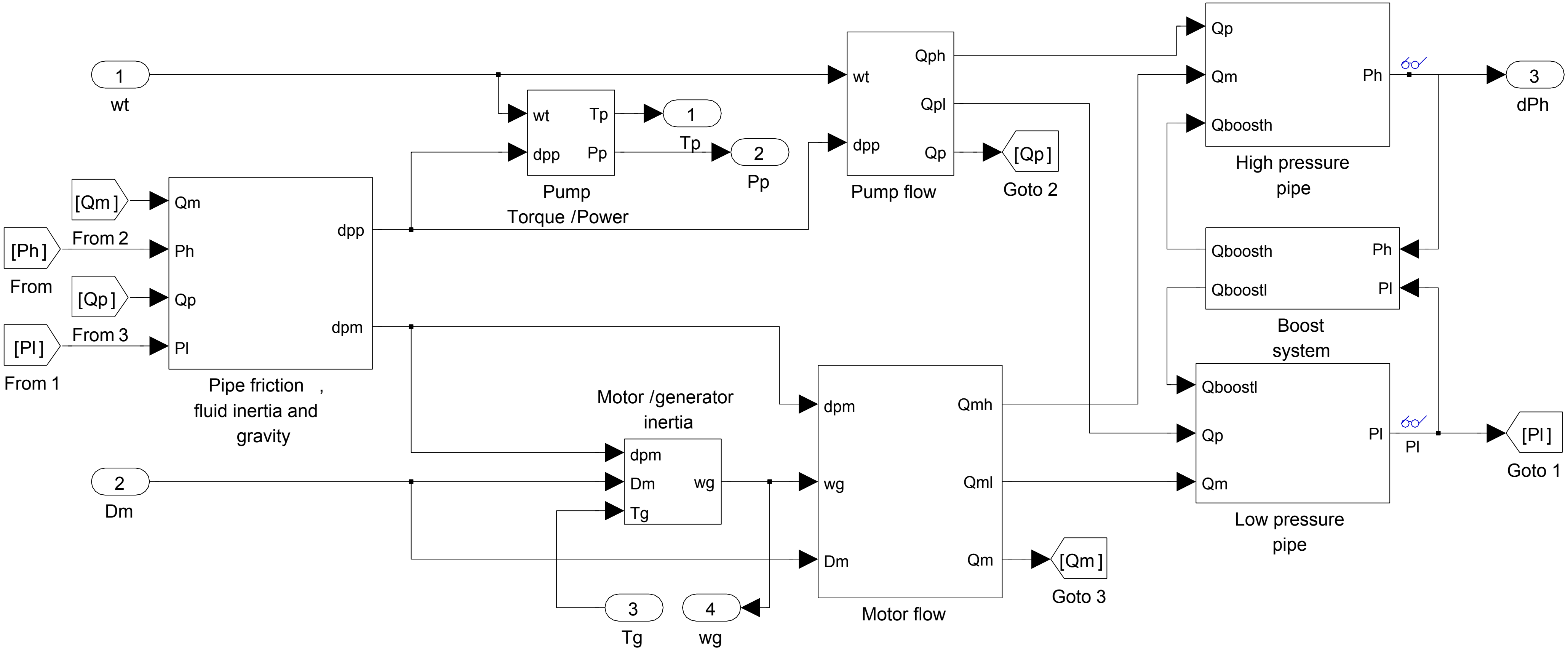
1
wt
wt
Tp
1
Tp
dpp
Pp
2
Pp
Pump
Torque /Power
wt
dpp
Qph
Qpl
Qp
Pump flow
[Qp]
Goto 2
Qp
Qm
Qbooosth
Ph
High pressure
pipe
3
dPh
[Qm]
From 2
[Ph]
From
[Qp]
From 3
[Pl]
From 1
Qm
Ph
Qp
Pl
dpp
dpm
Pipe friction ,
fluid inertia and
gravity
Qbooosth
Qboostl
Ph
Pl
Boost
system
Qboostl
Qp
Qm
Pl
Pl
Low pressure
pipe
[Pl]
Goto 1
Motor /generator
inertia
dpm
Dm
Tg
wg
dpm
wg
Dm
Qmh
Qml
Qm
Motor flow
[Qm]
Goto 3
2
Dm
3
Tg
4
wg

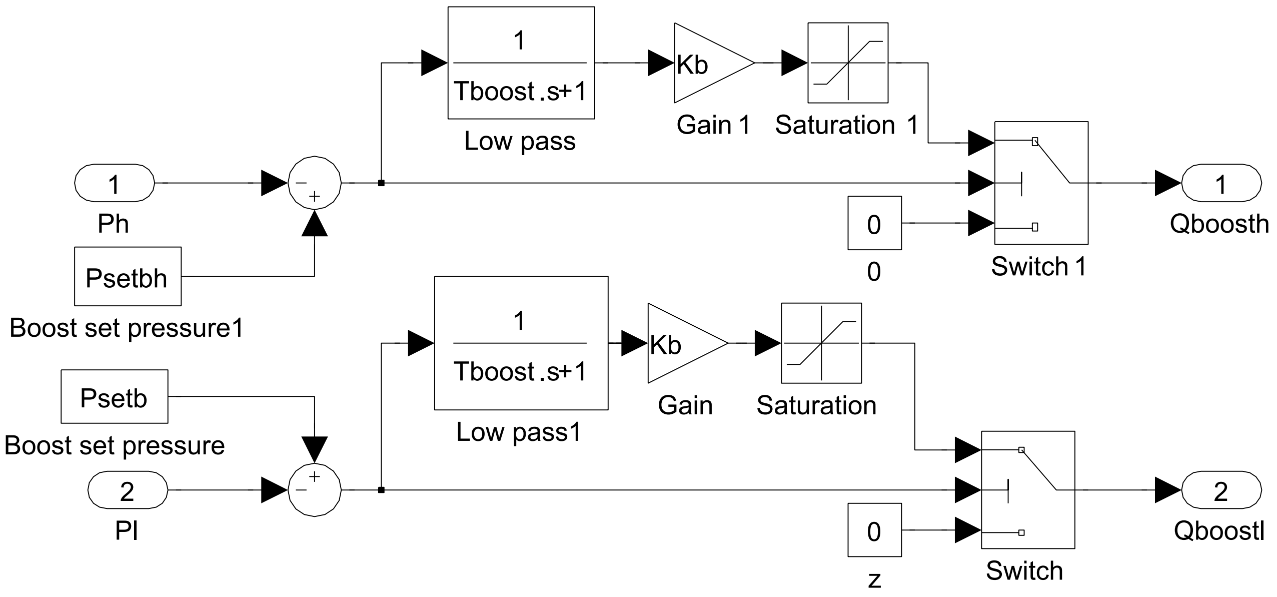
1
Tboost.s+1
Low pass
Kb
Gain 1
Saturation 1
1
Ph
Psetbh
Boost set pressure1
0
0
Switch 1
1
Qboosth
1
Tboost.s+1
Low pass1
Kb
Gain
Saturation
Psetb
Boost set pressure
2
Pl
0
z
Switch
2
Qboostl

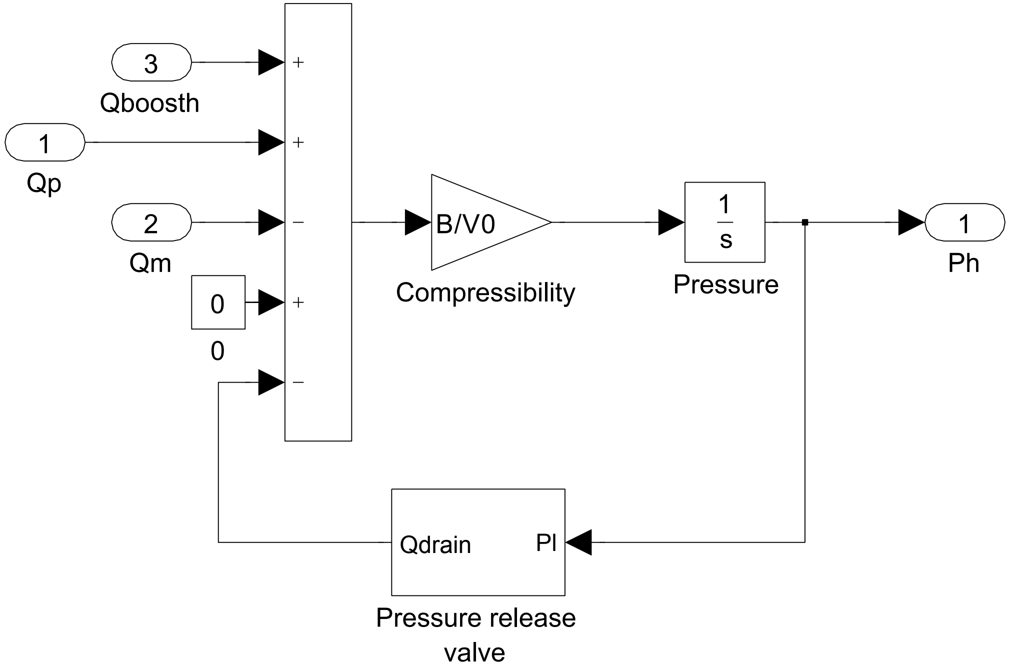
3
Qboosth
1
Qp
2
Qm
0
0
+
+
−
+
−
B/V0
Compressibility
1
s
Pressure
1
Ph
Qdrain
Pl
Pressure release valve

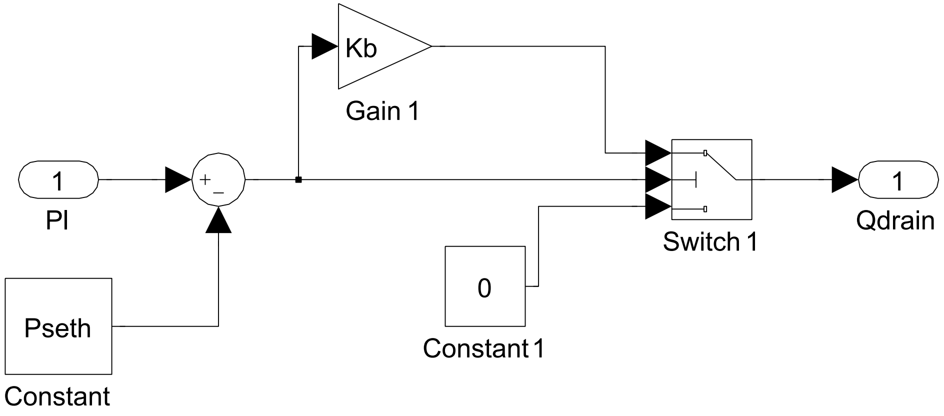
Kb
Gain 1
1
Pl
+
–
Switch 1
1
Qdrain
0
Constant 1
Pseth
Constant

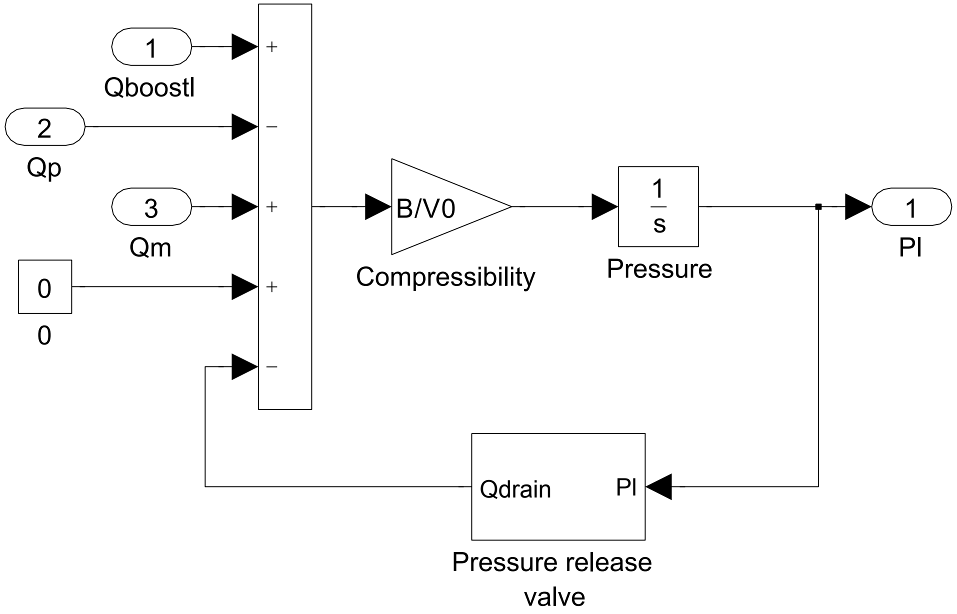
1
Qboostl
2
Qp
3
Qm
0
0
+
−
+
+
−
B/V0
Compressibility
1
s
Pressure
1
Pl
Qdrain
Pl
Pressure release valve

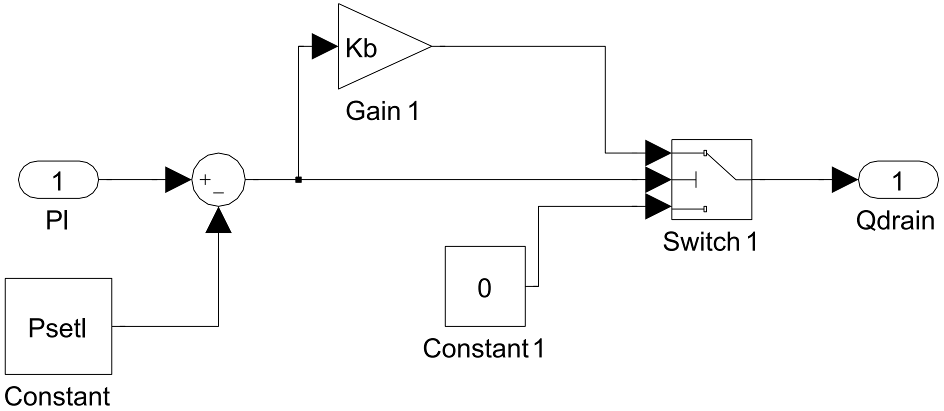
Kb
Gain 1
1
Pl
+
_
Psetl
Constant
0
Constant 1
Switch 1
1
Qdrain

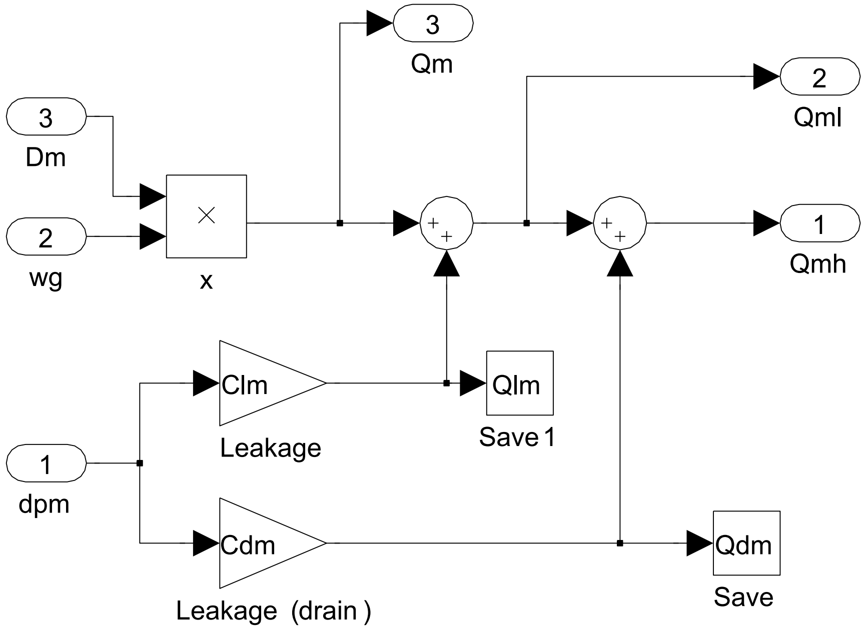
3
Qm
2
Qml
3
Dm
2
wg
x
+
+
+
+
1
Qmh
Clm
Leakage
Qlm
Save 1
1
dpm
Cdm
Leakage (drain)
Qdm
Save

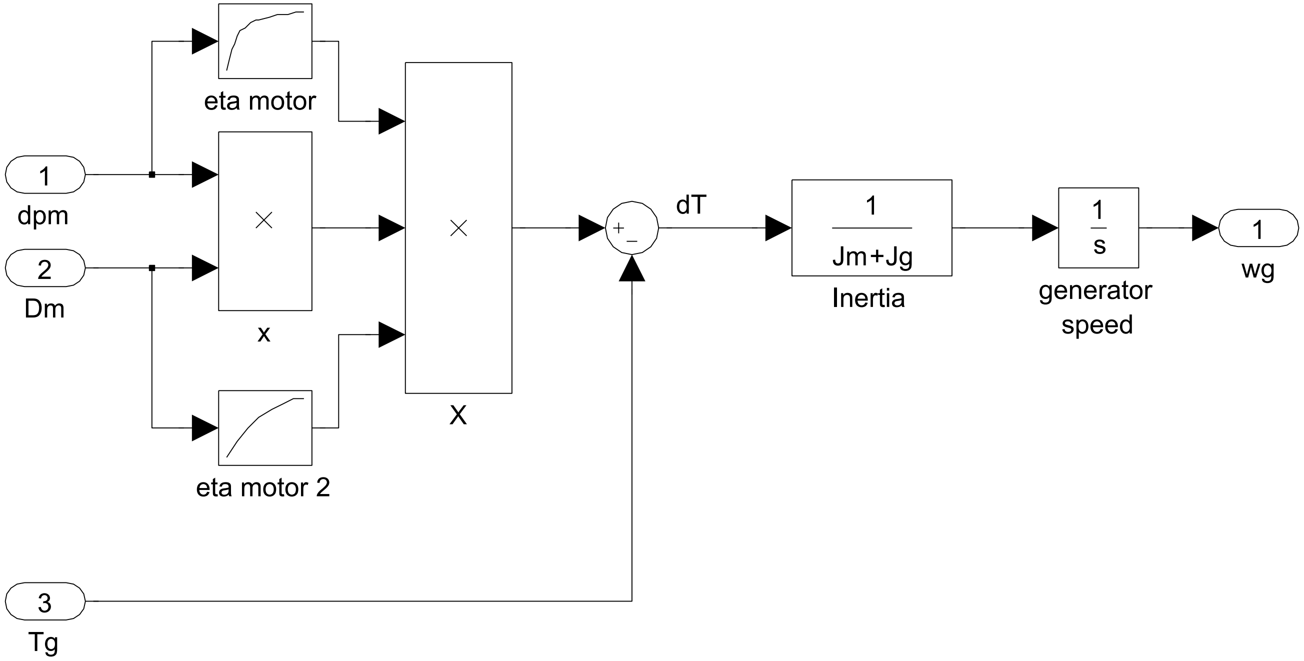
1
dpm
2
Dm
3
Tg
eta motor
x
eta motor 2
X
+
_
dT
1
Jm+Jg
Inertia
1
s
generator speed
1
wg

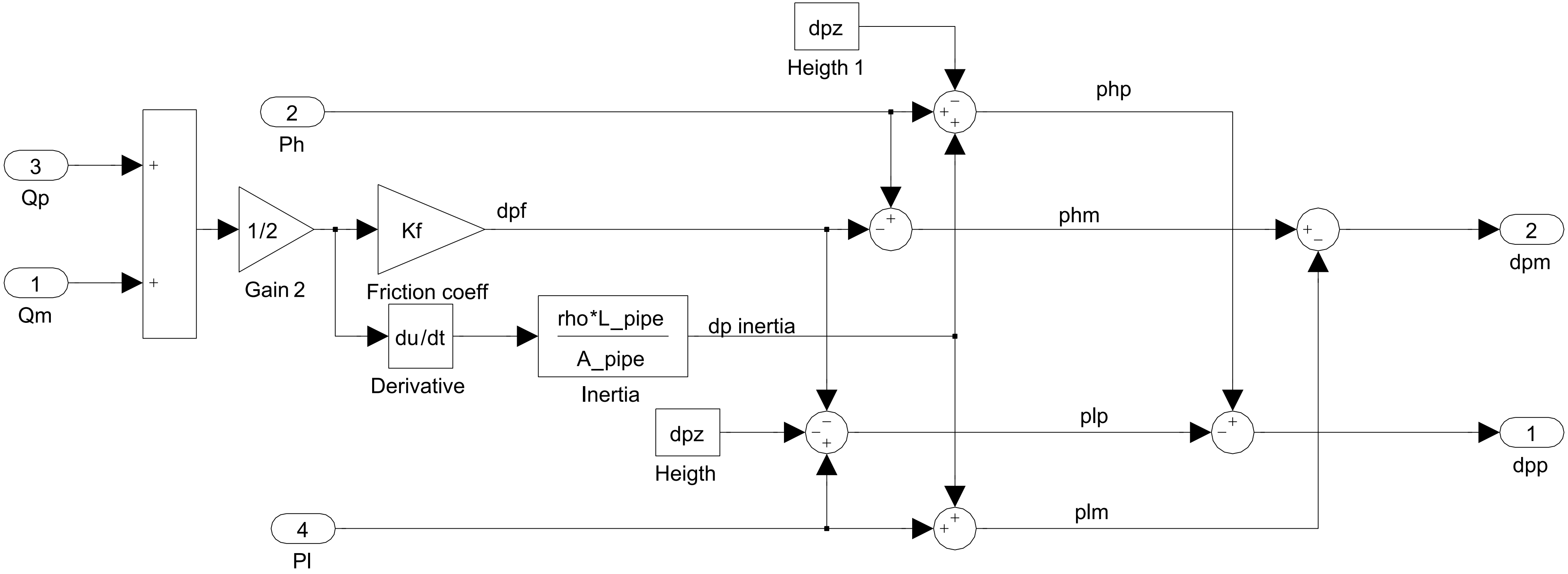
dpz
Heigth 1
php
2
Ph
3
Qp
1
Qm
1/2
Gain 2
Kf
Friction coeff
dpf
phm
2
dpm
du/dt
Derivative
rho*L_pipe
A_pipe
Inertia
dp inertia
dpz
Heigth
plp
1
dpp
plm
4
Pl

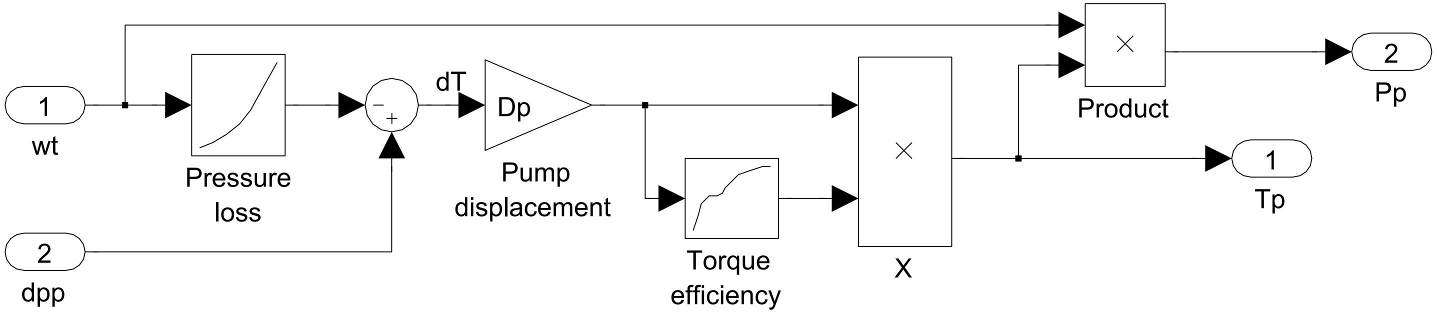
1
wt
2
dpp
Pressure
loss
dT
Dp
Pump
displacement
Torque
efficiency
X
Product
2
Pp
1
Tp

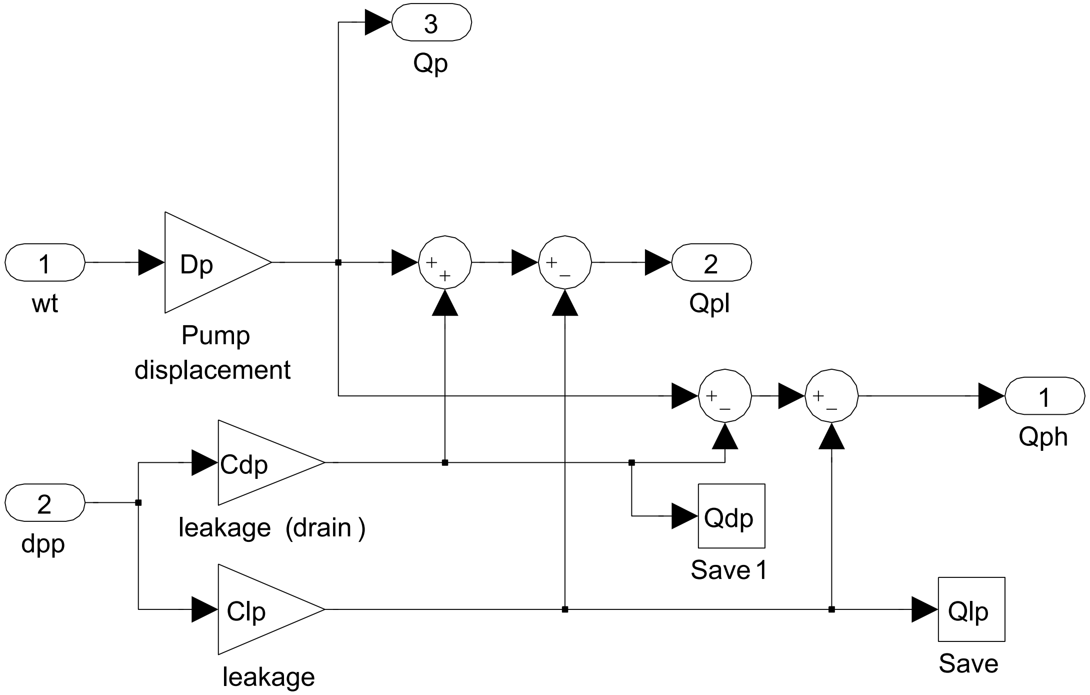
3
Qp
1
wt
Dp
Pump
displacement
+
+
+
−
2
Qpl
+
−
+
−
1
Qph
Cdp
leakage (drain)
2
dpp
Qdp
Save 1
Clp
leakage
Qlp
Save

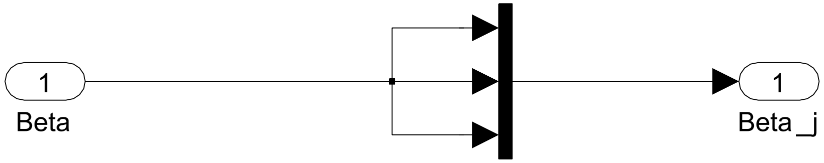
1
Beta
1
Beta _j

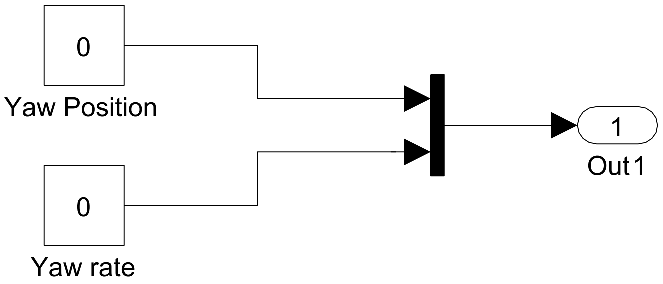
0
Yaw Position
0
Yaw rate
1
Out1

Appendix G

Quasi-steady model block diagram

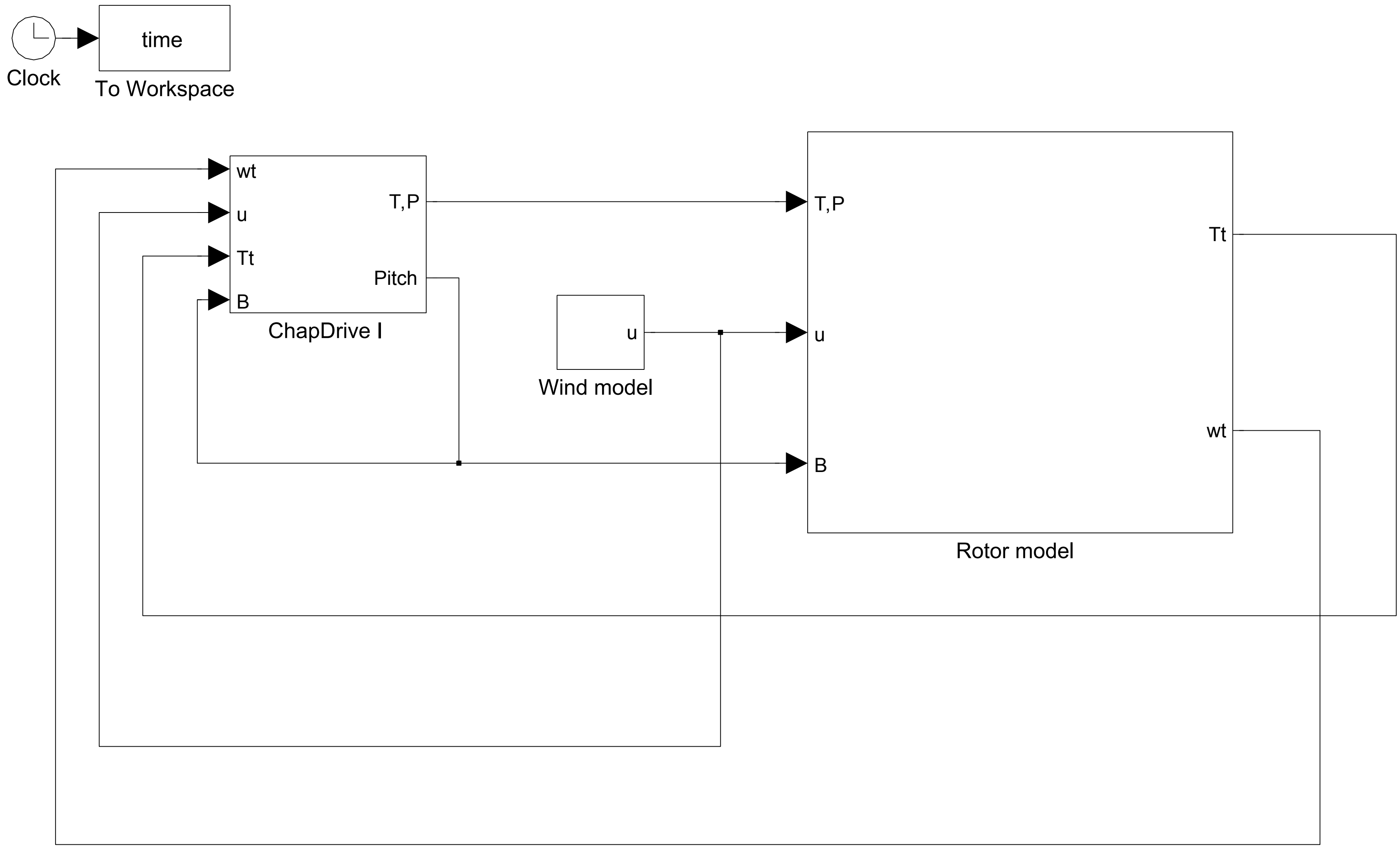
time
Clock
To Workspace
wt
u
Tt
B
T,P
Pitch
ChapDrive I
u
Wind model
T,P
u
B
Tt
wt
Rotor model

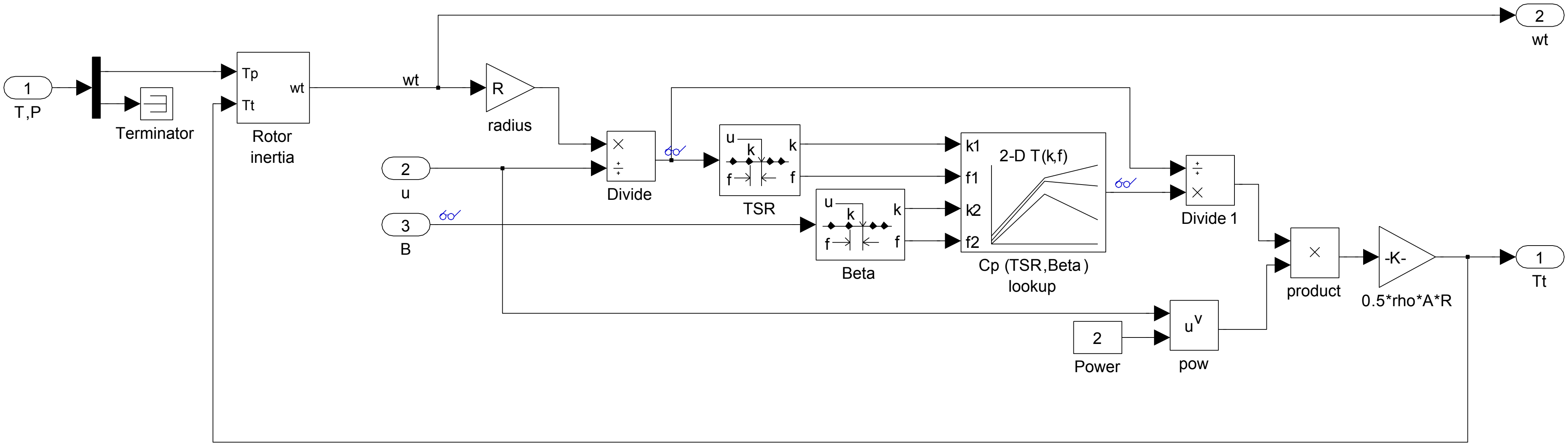
1
T,P
Terminator
Tp
Tt
wt
Rotor
inertia
wt
R
radius
2
wt
2
u
3
B
Divide
u
k
k
f
f
TSR
u
k
k
f
f
Beta
k1
f1
k2
f2
2-D T(k,f)
Cp (TSR,Beta)
lookup
Divide 1
product
-K-
0.5*rho*A*R
1
Tt
2
Power
u^v
pow